UNIVERSITY OF BIRMINGHAM

Ceramic Materials for the Immobilisation of High Level Radioactive Waste

By

Philip H. Walsh Atkins

Supervisors: Dr Mark S. D. Read and Dr Joseph A. Hriljac

A thesis submitted to The University of Birmingham

for the degree of Master of Science

The School of Chemistry

College of Engineering and Physical Sciences
University of Birmingham
April 2016

Abstract

The aim of this project was to investigate, both experimentally and theoretically, the perovskite mineral calcium titanate ($CaTiO_3$) and to gain a greater insight into its properties. Primarily, the properties studied were the defect chemistry of the material and the effect of doping on the structure, with particular attention being given to strontium and yttrium incorporation. This focus was chosen due to the potential applications of calcium titanate in radioactive waste immobilisation, primarily as one of the constituent phases in SYNROC.[1]

Experimentally, the effect on the structure of significant levels of strontium impurity was studied, with attention being given to phase changes and possible implications for the maximum level of doping in the structure. To compliment this, a theoretical investigation was undertaken into how defects within the $CaTiO_3$ structure manifest themselves, how charge imbalances may be accounted for and the implications this has for radioactive waste immobilisation.

Initially, substitutional defects were examined, followed by defect clustering and how multiple defects may interact with each other in the system. Strontium doping is of major concern in the $CaTiO_3$ structure due to the use of the mineral in radioactive waste immobilisation, and consequently the effect of yttrium and zirconium doping is also of relative importance due to their formation in the ^{90}Sr decay chain.

1. A. Ringwood, S. Kesson, N. Ware, W. Hibberson and A. Major, *Nature*, 1979, **278**, 219-223.

Acknowledgements

This last year has been quite an adventure, and finally getting to this point where I can put together a piece of work and analyse everything is definitely a relief. Numerous people have helped me along the way and deserve some recognition. First and foremost I would like to thank my supervisors Dr Mark Read and Dr Joe Hriljac for giving me this opportunity and putting up with me for the last year, as well as the Read/Hriljac groups for all their invaluable advice when I was completely lost and confused. In particular my thanks goes to Geoff for being a fountain of computational knowledge, putting up with constant frustrated emails, and a lot of the code used in this project. In addition, Sav, George, Ryan, Evin, Laura and Phil were a great help in the lab making sure I didn't burn the building down. In that regard I would also like to thank the rest of floor 5 for both scientific advice and generally making the last year so enjoyable.

Throughout the last year I have been given considerable help with proof reading, corrections and general structuring of this thesis. I would like to thank everyone who has for the most part kept this thesis legible, and kept myself sane throughout the whole process. The most credit goes to Rob, Katy, Chris and Emma for putting up with me at home and all the floor 5 masters students. I also need to thank John for help with simulations once I had left Birmingham, and Prof Saiful Islam and the Islam group (University of Bath) for their support in the months since.

Finally I would like to thank my parents for their support, guidance, and financial assistance throughout this endeavour.

Calculations in this work were performed using the BEAR HPC service at the University of Birmingham.

Contents

Abbreviations

FWHM – Full Width at Half Maximum

GSAS – General Structural Analysis System

GULP – General Utility Lattice Program

HLW – High Level Radioactive Waste

ILW – Intermediate Level Radioactive Waste

LLW – Low Level Radioactive Waste

Ln – Lanthanide

MC – Monte Carlo

MOX – Mixed Oxide Fuel

PXRD – Powder X-ray Diffraction

RDF – Radial Distribution Function

RE – Rare Earth

REE – Rare Earth Element

SYNROC – Synthetic Rock

XRD – X-ray Diffraction

Definitions

Radionuclide: An atom with an unstable nucleus that undergoes radioactive decay

Vitrification: Transformation of a substance into glass

Diffraction: The process by which a wave spreads out as a result of passing through an aperture of similar size to the wavelength of the wave

Ceramic: An inorganic solid comprising of atoms held together with ionic and covalent bonds. Normally crystalline, a similar amorphous material would be a **glass**

Isotope: Isotopes of an element contain differing numbers of neutrons to each other. A **radioisotope** is a radioactive isotope.

Radiation: The energetic particles or waves emitted by a radioactive isotope during the breakdown of an unstable nucleus.

Half-life: The time taken for the radioactivity of an isotope to fall to half of its original value

Chapter 1: Introduction

Within the nuclear industry, ceramics are utilised in a wide range of applications, the most common being nuclear fuels (UO_2, MOX) and as wasteforms for high level radioactive waste (HLW).[1] The main current method of waste immobilisation used is vitrification in borosilicate glass, which has several disadvantages that the development of new ceramic wasteforms is aiming to abate. Key among these is the brittle nature of the glass and the fracture tendency of the glass matrix.[2] Ceramics are less affected by these issues, are cheaper to produce and safer to move and store, and also have higher thermal stability. Additionally, ceramics have a higher density than glasses, which means that they can accommodate higher waste loadings in smaller areas than glasses are able to. The consequence of these beneficial properties is that ceramics are potentially more ideal waste immobilisation matrices than glasses.[3]

The three major categories of ceramic with potential for waste immobilisation are silicate, phosphate, and titanate ceramics. These ceramics all have MO_x polyhedra throughout their structures, where M = Si, P or Ti. Of these, silicates and phosphates are more structurally analogous to the current glasses used within the industry. Zircon ($ZrSiO_4$) based ceramics are silicates proposed for rare earth element and actinide incorporation, with the durability and low solubility of the ceramic being identified as ideal for immobilisation of weapons grade plutonium. Upwards of 9 mole% of Pu has been synthesised within a zircon lattice, with Th and U solubility limits closer to 4 mole%. Other rare earths such as Gd have also been incorporated

into zircon at high (500 – 1000+ ppm) concentrations.[4] Monazite – $RE(PO_4)$ (Where RE= Rare Earth lanthanides and yttrium) and Xenotime – YPO_4, are proposed as viable phosphate ceramics for waste lanthanide immobilisation as a consequence of their abundance in nature as rare earth accessory minerals. The compositions of the materials are similar, both being rare earth phosphates, though there are several structural differences originating from differences in the MO_x polyhedra in their lattices. This structural difference translates to changed affinities for incorporating different rare earths. Xenotime accommodates smaller rare earths in an REO_8 polyhedron, whereas monazite incorporates larger rare earths in an REO_9 polyhedron. They also have differing unit cell symmetries, with monazite being monoclinic and xenotime being tetragonal.[5]

The third major ceramic category, titanate ceramics, encompasses calcium titanate perovskite ($CaTiO_3$), pyrochlore, and zirconolite. Their common feature is the TiO_x polyhedra in the structure.[6] The ceramic phases in SYNROC are also, for the most part, titanate ceramics.

1.1: SYNROC – Synthetic Rock

When utilising potential ceramic waste forms for immobilisation of high level waste, the particular properties of each waste form needs to be adapted for successful incorporation of the particular waste stream without major structural change. Some of these waste forms are single phases, constituted of a single ceramic, with a specific material or mineral chosen as the ideal container for a particular isotope. Conversely,

other proposed waste forms can be constituted of multiple phases for accommodating a wider array of waste isotopes. At present, the ceramic waste form closest to being used in waste immobilisation is the multiphase ceramic SYNROC. Developed by Ringwood in 1979, SYNROC has several key advantageous properties that underline its suitability as a potential waste form. SYNROC has been shown to be highly durable in aqueous conditions, and particularly resistant to corrosion. In leach testing, the majority of dissolved material originated from minor phases in the material that contained small (<5%) quantities of radioactive isotopes.[7] The ceramic has been shown to be more durable than its borosilicate glass competitor, and is also of greater density – hence a higher waste loading can be achieved.[3]

1.1.1: SYNROC Phases

The most common SYNROC formulations consist of three titanate ceramic phases – zirconolite, hollandite and perovskite. Each of these is utilised for their ability to immobilise a particular radioisotope, with the formulation as a whole designed to immobilise as many isotopes as possible.[1, 8, 9]

Zirconolite (Fig. **1.2**) is one of the major phases of SYNROC and within 'SYNROC-C' – a common SYNROC formulation – comprises approximately 20 wt% of the volume of the material. Zirconolite is utilised to immobilise lanthanides and actinides such as U and Pu, and both trivalent and tetravalent species from nuclear waste can be readily

incorporated within the structure.[10] With the monoclinic $CaZrTi_2O_7$ structure, derived from an anion-deficient fluorite structure, there are multiple cation sites of differing coordinations where waste cations can be accommodated.[6, 11] Throughout the structure there are layers of corner linked TiO_6 octahedra, alternating through the lattice with layers of Ca and Zr sites. The structure can be formed easily under oxidising conditions, whereas under reducing conditions both fluorite and perovskite impurity phases are formed within the material. This is due to partial reduction of Ti^{4+} to Ti^{3+} and subsequent loss of positive charge.[11] The 8-coordinate Ca site in zirconolite can be substituted with trivalent lanthanide ions such as Nd^{3+} and Ce^{3+}. Up to 85% of the Ca sites in the structure are able to be substituted before additional phases, such as zirconia and alumina, begin forming within the material. This may be problematic as additional phase production can decrease the ability of the material to retain waste isotopes. There is structural change from 65% – 85% substitution where the cell changes from monoclinic to orthorhombic, but the ability of zirconolite to resist change at high substitutions up to this point is an indication of the effectiveness of this phase for HLW immobilisation.[10]

Hollandite (Fig. **1.1**) – $(Ba,Cs)(M,Ti)_8O_{16}$ – is a titanate ceramic incorporated into SYNROC for the purpose of immobilising Cs^+ and Ba^+ ions. Throughout the hollandite system there are columns of edge-sharing TiO_6 octahedra, which are arranged like walls to create 2x2 tunnels down the short axis of the structure. Within these tunnels there are 8-coordinate 'A' cationic sites – where Ba^+ and Cs^+ ions can be accommodated.[12] The nature of the 'B' TiO_6 cationic sites in the tunnel 'walls' dictates

the selectivity of the ceramic for incorporating different cations on the A site. 'M' is either a trivalent d-block element or trivalent group 13 element such as aluminium.[13] Amoroso *et al.* (2014) demonstrated that for Cs retention the B site being occupied by Cr^{3+} gives the greatest level of retention compared to other 3+ cations such as Fe^{3+} and Al^{3+}. Fe-hollandites also show some affinity for immobilising waste caesium ions, with waste rubidium ions being more favourably accommodated within Al-hollandites.[13, 14] These properties are due largely to B site cations expanding the structure such that the A site can then accommodate larger cations. Cr^{3+} has an ionic radius of 0.615 Å which makes it more ideal for Cs^{+} (1.74 Å) retention than Al^{3+} – which has a smaller ionic radius of 0.535 Å.[15, 16] The ability of the hollandite structure to accommodate several waste isotopes, most importantly ^{137}Cs and ^{137}Ba, underlines the reasoning behind its incorporation within SYNROC.

The third main ceramic phase within SYNROC is Calcium Titanate perovskite (Fig. **1.3**) – $CaTiO_3$. Perovskite is a key feature for the immobilisation of light rare earth elements (La, Ce), actinides, and for ^{90}Sr and its decay products.[9, 17] $CaTiO_3$ is of the ABX_3 perovskite structure type, with large Ca cations on the 12-coordinate 'A' site centrally in the unit cell, surrounded by smaller Ti cations on the 'B' site, within BO_6 octahedra. The $CaTiO_3$ structure is orthorhombic and distorted from the ideal primitive cubic symmetry of perovskite.[6] Tilting of the octahedra with the changing ion size pushes the cubic system into an orthorhombic symmetry. This perovskite phase is of particular interest, as the incorporation of Sr into the lattice, though commonly studied, has not been modelled extensively. Additionally, the effect of the

Sr decay products – yttrium and zirconium – on the material has not been examined in great detail. Strontium incorporation is particularly facile in $CaTiO_3$ due both to the similar ionic radii and properties of the two elements. Both are group 2 alkaline earth elements and hold 2+ charges within crystal systems. A continuous solid solution between $CaTiO_3$ and $SrTiO_3$ exists, also demonstrating the ability of Sr to be incorporated.[18]

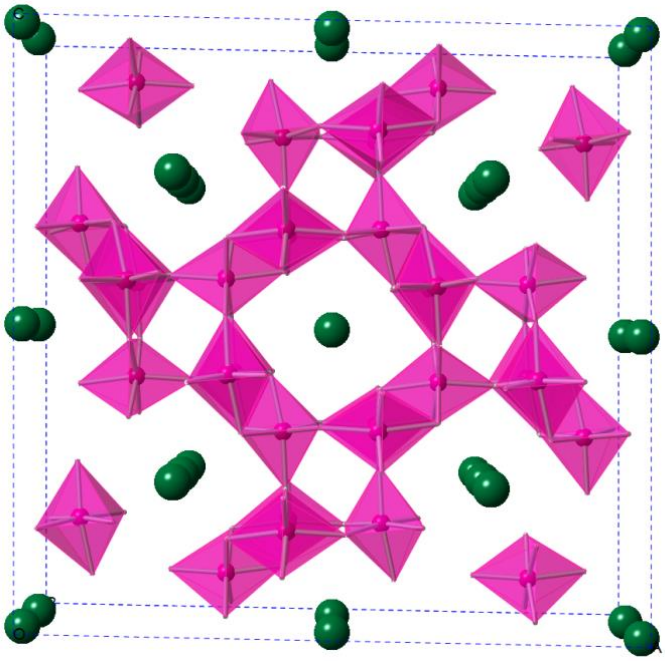

Fig. 1.1: The crystal structure of hollandite. (Top down – 010 – projection) The dark green A site cations are situated in central cavities surrounded by pink B and C (M) site octahedra. Changing the nature of these sites changes the size of the cavity, impacting on the immobilisation ability of the material for different radioisotopes. This structure shows a Ba-Mn hollandite, as described by H. Miura (1986) with Ba occupying the A site and Mn in the B and C sites.[19]

Adapted From: H. Miura, *Miner. J.,* 1986, **13,** 119-129

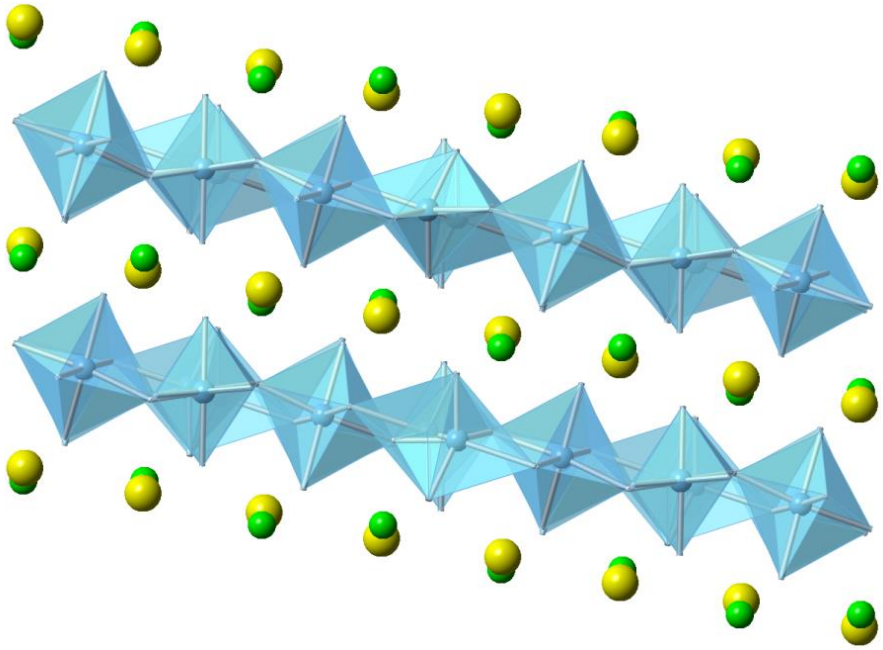

Figure 1.2: The crystal structure of zirconolite projected down the 010 – b – axis. Layers of yellow Ca and light green Zr atoms alternate in the structure between TiO_x octahedra. The two (Ca and Zr) cation sites present mean both trivalent and tetravalent waste ions can be immobilised with relative ease.[20]

Adapted From: K. Whittle *et al.*, *Am. Mineral.,* 2012, **97**, 291-298

SYNROC also contains a significant quantity of rutile TiO_2, which is an inert matrix that in most SYNROC formulations is not primarily used for waste immobilisation. However, there has been a suggestion for use of TiO_2 to encapsulate ruthenium and technetium isotopes.[21] TiO_2 is important in mediating the formation of secondary phases within the material which could have undesirable mechanical effects such as lower durability. SYNROC formulations with high titanium content and rutile saturation prevent the formation of phases with low Ti concentrations, such as $CsAlTiO_4$. These have higher leach rates – are affected more by ground water in the

system – and as such are detrimental to the performance of the waste form.[9] Excess TiO_2 is also incorporated into SYNROC to provide the ability to adapt the waste form for different waste streams – where rutile could be utilised to encapsulate different elements. The main example of this is SYNROC-E, where encapsulated radioisotopes are embedded in the inert rutile matrix. Addition of other oxides to the ceramic, such as Na_2O, can also form undesirable soluble phases like $NaAlSiO_4$. Despite this, the modified material can accommodate waste loadings of considerable levels before the properties of the waste form are adversely affected.[3] In some compositions, other ceramic phases such as pyrochlore – $(Na,Ca)_2Nb_2O_6(OH,F)$ – may be present in significant quantities. The cation sites in pyrochlore are able to immobilise Sr, U, and rare earth elements. It also makes up the bulk of the material in SYNROC-F, whereas in SYNROC-E the ceramic is only present in small quantities (~2 wt%).[3, 9]

1.1.2: SYNROC Formulations

The variability of SYNROC to accommodate a desired waste stream means SYNROC is produced in several variations for different purposes, such as SYNROC-E, as discussed above. The original formulation developed by Ringwood was SYNROC-A, followed by SYNROC-B/C. The design of each is tailored to different waste streams via use of varying levels of different ceramic matrices: SYNROC-B/C, comprised of the aforementioned titanate phases and various alloys, is designed to accommodate ~20 wt% of HLW from nuclear reactors. Specifically, SYNROC-C is the waste form containing material upon addition of HLW, whereas the precursor material

comprised of just the initial ceramic phases is SYNROC-B. SYNROC-E has a similar composition to SYNROC-C, but with a large excess composition (~80 wt%) of rutile, and holds less HLW (~7 wt%). This formulation is more suited for geological disposal in salt beds and the seabed.[9, 22] SYNROC-F is produced in a similar way to SYNROC-C, but is pyrochlore rich with a small wt% of hollandite and rutile making up the rest of the composition (~5 wt% of each). This formulation is considerably more resistant to leaching than untreated spent fuel, is primarily for spent fuel which has not been reprocessed, and can be buried with less costly containment precautions than untreated fuel.[9] Table **1.1** summarises the SYNROC phases, their constituents and ideal usage.

Table 1.1: SYNROC Variants, their respective compositions and uses

SYNROC Variants, Their Respective Compositions and Uses			
Material	**Composition**	**Elements Immobilised**	**Usage**
SYNROC-A	Silicates, titanates	Cs	Prototype
SYNROC-B	Hollandite – ~33 wt% Zirconolite – ~28 wt% Perovskite – ~19 wt% Rutile – ~15 wt% Alloys – ~5 wt%	Ba, Cs, Sr, U, Th, REEs, Pu, d-block, Te, I	Precursor material for SYNROC-C
SYNROC-C	Hollandite – ~33 wt% Zirconolite – ~28 wt% Perovskite – ~19 wt% Rutile – ~15 wt% Alloys – ~5 wt%	Ba, Cs, Sr, U, Th, REEs, Pu, d-block, Te, I	20% waste loading. Waste from reprocessing of spent reactor fuel e.g. UO_2
SYNROC-D	Zirconolite – ~16 wt% Perovskite – ~11 wt% Spinel – ~55 wt% Nepheline – ~18 wt%	Al, Na, 1st row d-block, Si, Cs	High (~80%) waste loading. Immobilise HLW produced from US defence program
SYNROC-E	Rutile TiO_2 – ~80 wt% Hollandite – ~5 wt% Zirconolite – ~7 wt% Perovskite – ~7 wt% Pyrochlore – ~2 wt%	Transuranic elements	Low (~5-7%) waste loading. Deposition in deep sea, ocean sediments, salt
SYNROC-F	Pyrochlore – ~95 wt% Hollandite – ~5 wt% Rutile – ~5 wt%	Cs, Ba, Sr, U, REEs	Fuel cycles where reprocessing not undertaken

Data from:

A. Ringwood *et al.*, *Nature.,* 1979, 278, 219-223.

A. Ringwood, *Mineral. Mag.,* 1985, 49, 159-176

J. Cooper *et al., J. Am. Ceram. Soc.*, 1985, 68, 64-70

1.2: Radioisotopes – Constituents of HLW

The calcium titanate phase within SYNROC has been proposed as a means to incorporate various radioisotopes present in high level radioactive waste. Immobilisation of ^{90}Sr is the main reasoning behind the incorporation of the material into SYNROC. Alongside ^{90}Sr it is proposed that other common isotopes – such as ^{137}Cs and its decay product ^{137}Ba – could be accommodated alongside lanthanide isotopes and REEs (Rare Earth Elements).[9, 23] These isotopes are common fission products of ^{235}U – the primary uranium isotope used in nuclear fuel.

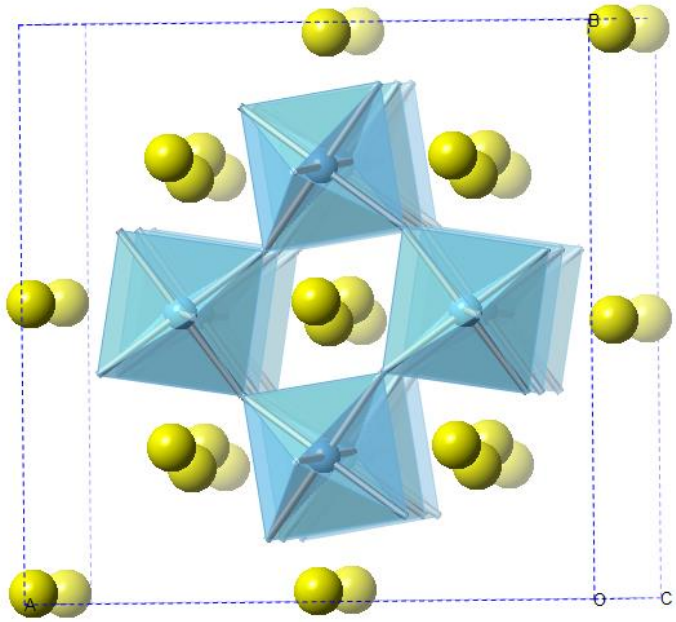

Figure 1.3: The $CaTiO_3$ perovskite structure – Yellow spheres are calcium (Ca^{2+}) ions on the A site with the blue octahedra representing the titanium (Ti^{4+}) ions (centre of the octahedron) on the B site bonded to oxygen (at the corners - not shown). Note orthorhombic structure – distorted from ideal cubic perovskite due to tilting of octahedra. Substitution of cations will occur on either the A or B sites depending on size and charge of dopant.

Adapted from: Structural information given by: S. Sasaki *et al.*, *Acta. Cryst.,* 1987, **43,** 1668-1674

1.2.1: Immobilisation of ^{137}Cs

For immobilisation of ^{137}Cs and ^{137}Ba, the ceramic hollandite has been proposed as the ideal waste form due to its ability to incorporate both Cs^{+} and Ba^{2+} ions, as well as having Ti^{4+} ions within the structure able to act as 'electron traps'. ^{137}Cs undergoes beta-negative decay, in which a neutron transforms into a proton and produces a β^{-} electron and an electron-antineutrino, forming ^{137}Ba. The ^{137}Cs isotope has a half-life of ~30.07 years and the resultant barium decay product is stable.[24]

Barium titanate ($BaTiO_3$) has a similar structure to calcium titanate, with a central 12-coordinate A site surrounded by 6-coordinate BO_6 octahedra, though it is tetragonal rather than orthorhombic. In this sense $BaTiO_3$ is closer to the more archetypal 'perovskite' structure, as with cubic $SrTiO_3$. Considerable research has been undertaken on the relationship between the two materials. $BaTiO_3$ has several beneficial electrical properties, such as ferroelectricity, and doping with calcium has been thought to improve these beneficial properties for industrial application.[25, 26] The Ca^{2+} ion has been seen to substitute into both the Ba^{2+} and Ti^{4+} sites in the barium titanate structure. On doping onto the Ba^{2+} site, creating $Ba_{1-x}Ca_xTiO_3$, phase change from cubic to tetragonal has been observed on increased doping level and increased temperature (at ~98 °C when doping level is at x=0.227).[27] Despite this relationship and relative ease of doping Ca into $BaTiO_3$ at low levels, little work has been published on doping Ba into $CaTiO_3$. This may be due to a lack of study in the area, or simply because the barium atom may be too large to incorporate into the lattice.

Consequently, despite their structural similarities, calcium titanate seems unable to easily incorporate the Ba^{2+} ion, and for similar reasons would also be unable to accommodate the even larger ^{137}Cs.

1.2.2: Immobilisation of Nd and Pr

Two larger lanthanide elements, Nd and Pr, are both also possible candidates for immobilisation in $CaTiO_3$, with their behaviours possibly being indicative of the nature of larger rare earth elements and lanthanides in general. Incorporation of Pr into the structure in small amounts (where x=0.1) has been seen to result in an orthorhombic crystal, similar to $CaTiO_3$. There is minor stress and strain on this system due to the change in ionic radius from Ca^{2+} (1.34 Å) to Pr^{3+} (1.286 Å), however this stress/strain is small due to there only being a minor radius difference of ~0.054 Å between the two ions. Consequently, the major consideration in Pr^{3+} incorporation is charge compensation, as there is now an excess of positive charge within the Pr-doped crystal. The mechanism for this has been suggested as either reduction of a Ti^{4+} to Ti^{3+} or equivalent change in oxygen content to compensate.[28] Nd^{3+} substitution has also been reported in the literature, garnering a material with useful optical properties, but this level of substitution was very small (x=0.01). Cell parameters were found to increase on addition of Nd^{3+} to the lattice, which may be indicative of some strain or phase change. However, the space group of the doped structure remained orthorhombic, indicating that the ion is more easily accommodated into the lattice.[29, 30] The aptitude of lanthanides to immobilise within the $CaTiO_3$ structure is

promising when assessing the ability of the mineral to accommodate different waste forms, and hence the ability of SYNROC to immobilise multiple waste streams.

1.2.3: Decay of ^{90}Sr

One of the main constituents of high level radioactive waste is ^{90}Sr – A β^- emitter with a half-life of 28.79 years, which decays into ^{90}Y. This yttrium isotope then decays, with a half-life of 64 hours and again via β^- emission, to stable ^{90}Zr.[31] Throughout this process the surrounding environment acts as an 'electron sink', accepting the emission of radiation and balancing the variation in charge which occurs. In $CaTiO_3$ this would possibly be the Ti^{4+} ions.[17]

1.3: Strontium and Barium Incorporation in Calcium Titanate

Due to the abundance of ^{90}Sr in high level radioactive waste, the safe immobilisation of this isotope is of pressing concern, with ceramics such as NZP (Sodium Zirconium Phosphate) and SYNROC being designed with this in mind. NZP can be loaded with ~6 wt% of Sr with little resultant change to the crystal structure, though above this level a secondary strontium zirconium phosphate phase begins to form.[32] Within SYNROC, strontium is immobilised preferentially in the perovskite phase (~66% of immobilised Sr), though Sr immobilisation also occurs in smaller quantities in hollandite and zirconolite (~18% and 6%).[7]

The structure of the $CaTiO_3$ perovskite phase used in SYNROC when doped with Sr changes shape and symmetry with increased loading. Ball *et al*. (1998) describe that this is particularly evident on phase change between orthorhombic and tetragonal, with an expansion of ~0.3%. Despite this, there is little resultant change in the volume of the structure – from ~56 to ~60 $Å^3$.[33] They also mention that the mechanical integrity of the perovskite may not be affected greatly by this change, giving promise for its use in waste immobilisation.[33] Perovskite has also been shown to retain large levels of strontium fixed within the structure for long periods of time, with leach rates from the structure over time remaining static. A study by Shrivastava *et al.* (2002) shows the ceramic after 90 days of leaching retaining ~86% of the original strontium within the structure.[34]

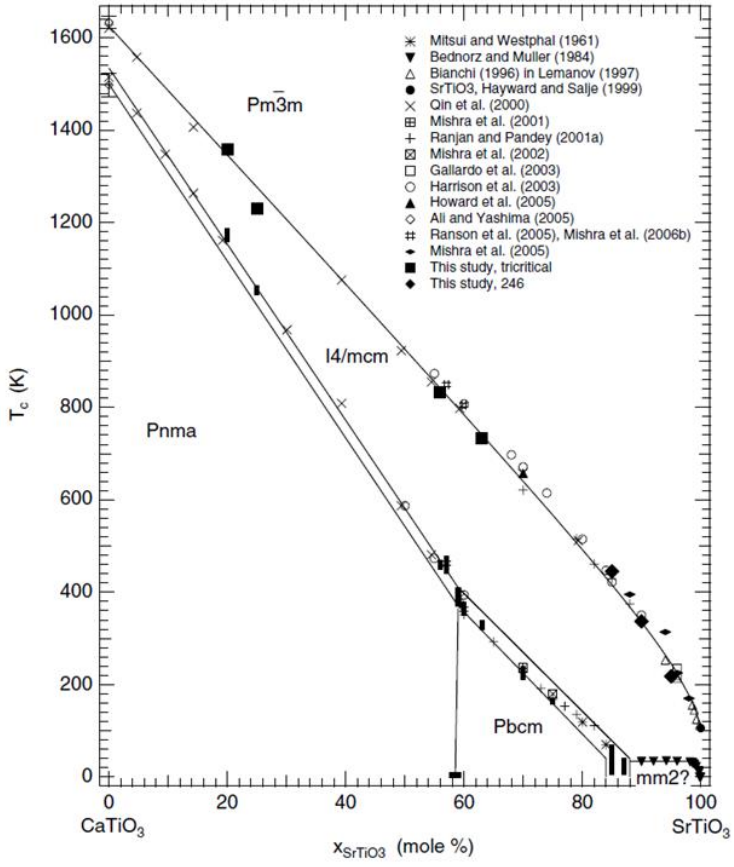

Figure 1.4: Phase diagram of the $CaTiO_3$ – $SrTiO_3$ solid solution. At room temperature (~298K) there is a phase change at approx. 58% substitution of Ca for Sr, and again from orthorhombic to tetragonal at approx. 65%. At very high Sr concentrations (90%+) the mineral structure is cubic.[18]

The large % concentration of Sr that can be incorporated into the lattice without considerable phase change highlights the potential of $CaTiO_3$ to immobilise ^{90}Sr.

From: M. A. Carpenter *et al., J. Phys.: Condens. Mater.*, 2006, **18,** 10725–10749

The similarities of $CaTiO_3$ and $SrTiO_3$ are such that they form a continuous solid solution through all of their phases, as evidenced in Figure **1.4**.[18] As the doping level of Sr into the $CaTiO_3$ structure increases, the symmetry of the system changes from orthorhombic (Pnma) through tetragonal (I4/mcm) to cubic (Pm-3m), with the high temperature phases of both systems being cubic.[18] The phase transition boundary between orthorhombic and tetragonal in the system lies at approximately x= 65-70 at room temperature, where x = the mole% of Sr in the material – essentially $Ca_{0.35}Sr_{0.65}TiO_3$. The phase transition to cubic occurs at ~90% Sr loading, showing $SrTiO_3$ remains cubic with only minor Ca incorporation. Conversely, $CaTiO_3$ retains its orthorhombicity with much larger strontium levels.[18, 33]

The intricacies of this structure change can be modelled via computational simulation. Within these simulations, the lattice changes on different doping levels can be deduced and compared to experimental data. The bulk properties of these titanates are well understood, but more insight could be gained into how the structure adapts around the differing cation sizes and the most energetically favourable configuration of the impurities. For example, whether they prefer to cluster together or spread apart.

Barium incorporation, though relatively unstudied, would likely follow a similar trend to that of strontium. The differences being the considerably larger ionic radius of the barium cation (1.61 Å compared to 1.44 Å for Sr)[16] which may force a structure change to cubic with smaller doping levels than the 90% doping needed for transition in the Ca-Sr system.

Though the main aim of this project is an investigation into the properties of $CaTiO_3$, attention must also be paid to similar materials. Strontium and barium titanates are both common and important structures, and to gain a full understanding of dopant incorporation into $CaTiO_3$, the end members of this doping must also be examined. Computational studies of these materials have been undertaken by Freeman (2011) and Dawson (2013), with the latter also examining calcium titanate.[35, 36] The focus of these papers is mainly on dopant incorporation of rare earth elements such as yttrium and lanthanides, and the charge compensation mechanisms such doping undertakes. This work leads on from that undertaken by Buscaglia *et al.* (2001), where the effects of divalent and trivalent dopants on the material were studied in detail. Buscaglia describes several different charge compensation mechanisms, along with the respective solution energies for each mechanism. The charge compensation mechanism with the lowest solution energy is thermodynamically more likely to occur experimentally.[15] Analysis of solution energies can also determine whether the studied defect is more likely to occur within a small cluster or at infinite dilution across the lattice, as well as the binding energy of a simulated defect. Also prior to this, Akhtar *et al.* (1985) derived a potential model for simulating strontium titanate and incorporating different cations into the lattice. They proposed several different charge compensation mechanisms, which the subsequent publications then improve and expand upon.[37]

1.4: Yttrium Incorporation in Calcium Titanate

^{90}Y, unlike ^{90}Sr, does not incorporate into $CaTiO_3$ without need for further changes to the material to accommodate the change in cationic charge. Both the calcium ion in the mineral and a strontium dopant have equivalent 2+ charges, and therefore can substitute with each other with relative ease. However the yttrium decay product has a 3+ charge and therefore there must be a mechanism of charge balance before the ion is immobilised. This change in charge is accompanied by the release of a β^- electron into the surrounding environment. The balance is likely caused by reduction of Ti^{4+} to Ti^{3+}, possibly via this electron, a mechanism already known to occur when immobilising cerium in $CaTiO_3$ in SYNROC-C.[38] An increase in oxygen content is also suggested to be a mechanism of charge compensation within the perovskite.[39]

A study by Navi *et al.* (2011) demonstrates that there is only minor substitution of Y within the perovskite phase of a perovskite-pyrochlore system, suggesting a tendency for the Y to separate from the perovskite forming a pyrochlore $Y_2Ti_2O_7$ phase upon incorporation. Formation of this secondary phase could prove problematic for the structural integrity of the material. Within the context of waste immobilisation it would not be ideal if the resultant phase has a higher tendency to dissolve or leach into the environment. Conversely, research suggests that due to the low concentration and low half-life of the isotope it can still be immobilised within the perovskite phase of the waste form.[23]

Further to this, there is the possibility that the Y^{3+} ion may prefer to reside in the B site of the perovskite, displacing a Ti^{4+}. Substitution of Y^{3+} into the lattice and

subsequent charge compensation can therefore be undertaken via several different mechanisms: Substitution on the Ca^{2+} site can be compensated via conduction electrons and cation vacancies, as well as the titanium reduction described for cerium immobilisation. Substitution on the Ti^{4+} site would be compensated via electron holes (lack of electrons) or oxygen vacancies.[38, 40]

Freeman *et al.* (2011) discuss five possible compensation mechanisms available for substitution of an M^{3+} REE ion into the $BaTiO_3$ structure, which is a cubic perovskite analogous to the $SrTiO_3$ structure. Further to this, they conclude that the size of the dopant cation is fundamental in determining which charge compensation mechanism is most favourable, in addition to the preferred site of substitution.[35] Dawson *et al.* (2013) further this work by examining these schemes in relation to $CaTiO_3$ and $SrTiO_3$, providing further evidence of dopant size being fundamental to substitution location and charge compensation scheme. This research shows that titanium reduction is unfavourable for larger REEs when substituting into $SrTiO_3$, with production of Sr vacancies instead being the preferred compensation mechanism. Mid-sized rare earths such as Gd and Eu are capable of doping onto both A and B sites, with this 'self-compensation' being described as the dominant mechanism. The mechanisms follow a similar pattern in $CaTiO_3$, with Gd and Eu doping via self-compensation at both sites. Evidence suggests that smaller REE ions have a larger range of possible charge compensation mechanisms they can undergo.[36] Work by Bassoli *et al.* (2008) supports the conclusion that smaller trivalent cations can occupy both A and B sites within the $CaTiO_3$ lattice, if the dopant ion size is between the two site sizes, as shown with Yb.[40] Yttrium (1.22 Å) falls into this category, though it is

closer in size to the calcium A site (1.34 Å) than to the titanium B site (0.605 Å).[16, 41] As a result it is likely to preferentially substitute on the A site over the B site.

This research is primarily aimed at explaining the behaviour of rare earth ions on incorporation, which, although giving us an idea as to the behaviour of yttrium in $CaTiO_3$, does not paint the full picture. As a Y^{3+} ion becomes apparent in the material after Sr decay, it will initially be located in the place of the Sr ion it decayed from. There is also a kinetic factor to consider when assessing where the Y ion is likely to place after this, as with the solution energies discussed previously. Though it may not initially be favourable thermodynamically for the atom to occupy the same space as the initial Sr, it may be kinetically even less favourable for the atom to move to a lower energy site. When considering charge compensation mechanisms, this means that in reality the process may not proceed via the lowest energy mechanism.

1.5: Zirconium Incorporation in Calcium Titanate

When considering the immobilisation of ^{90}Zr, the effect of further decay no longer needs to be taken into account as it is a stable isotope. Despite this, there remain several issues with immobilising Zr within $CaTiO_3$. Chief among these is the Zr^{4+} cation being too small (0.72 Å) for the calcium site it originated from, much closer in size to Ti^{4+}. The waste radionuclide may then transfer on decay of Y to the more 'comfortable' B site which accommodates the ion more easily. An issue here being the

Zr^{4+} ion is larger than the Ti^{4+} cation on the B site, complicating easy incorporation into this position. Furthermore, due in part to the size difference, the $CaZrO_3$ structure contains more distorted BO_6 octahedra than $CaTiO_3$ – The ZrO_6 octahedra are more tilted than the TiO_6 octahedra in $CaTiO_3$. The consequence of this is that incorporation of significant quantities of zirconium may induce phase changes in the mineral system. which has been seen to occur at high pressures.[42]

Additionally, the issue of charge balancing is greater with Zr^{4+} than with Y^{3+}. Some of the possible mechanisms of charge balance within this system are described by Ringwood (1985);[9] Ringwood notes that previous studies describe the location of the Zr^{4+} cation on the Ca^{2+} site, and that appropriate compensation has been achieved by substituting divalent and trivalent cations onto the B sites to achieve stability. It is also noted that at significant (25%+) loadings of zirconium the ion may diffuse through the structure onto the B site leaving an A site vacancy.[17] Furthermore, appropriate compensation of Ti^{4+} with Ti^{3+}, two for each Sr – Y – Zr decay, could effectively balance the resulting charge variation.[9] The hard Sr doping limit for this mechanism to occur would be 50% waste loading without transmutation or the formation of secondary phases occurring, with the actual limit possibly being lower.

The 'B' site in the perovskite structure is more accommodating to the Zr^{4+} ion, even though the Ti^{4+} ion is smaller. With the size issue it could be expected that the ion may transfer into this site, with the aforementioned stabilisation via reduced Ti^{3+} not having a considerable affect. This would cause an excess of B^{4+} cations in the mineral. Upon this excess manifesting, the Zr cations may diffuse from the lattice and form a

separate phase entirely. Incorporation of Zr into the $CaTiO_3$ lattice has been shown to produce a $CaZr_{1-x}Ti_xO_3$ solid solution, followed by production of a secondary Ca–Ti–Zr–O phase as the stoichiometry of the material alters and temperature increases – with faster diffusion on increased temperature. The formation of this secondary phase suggests that the waste form is thermodynamically unstable with increased Zr concentrations, further driving diffusion and secondary phase production.[17] As lower temperatures hinder the zirconium diffusion, kinetic factors may come into play more when examining the behaviour of the waste form, which is an area that still needs to be studied in detail.

Szajman *et al* (1987) have shown that substitution of similarly tetravalent U^{4+} into SYNROC-C preferentially occurs at the Ti^{4+} B site. This is due to its similar charge and valence, supporting the argument that Zr^{4+} may also preferentially reside on the B site. In the SYNROC zirconolite phase the uranium ion has been shown to substitute mostly into the Zr^{4+} site, suggesting the two ions have similar behaviours/preferences when substituting into $CaTiO_3$.[38]

Overall it seems more likely that the behaviour of the Zr^{4+} ion within the mineral structure will produce a separate phase, possibly similar to zirconolite already present in SYNROC. Remaining in the A site would be unlikely due to the characteristics of the ion as discussed. Movement to the B site from the A site would potentially disrupt the lattice greater than secondary phase creation; particularly as an apparent A site vacancy would be caused by this. This possibility raises questions about the ability of $CaTiO_3$ in SYNROC to immobilise the entire Sr-Y-Zr decay chain.

As a result, more research will need to be done to determine the exact mechanism that the Zr^{4+} ion undergoes within the material once it has been produced. The reduction of two Ti^{4+} ions may have a stabilising effect, meaning possible retention of the Zr^{4+} ion on the A site, but considerably more research would need to be undertaken before any such conclusion can be made.

1.6: Conclusion and Continuing Research

The main advantage of using a multiphase ceramic over a single phase ceramic is the ability to incorporate numerous different elements effectively. This is due to the number of different sites available for substitution. SYNROC can effectively immobilise many isotopes present in high level waste, and the perovskite phase forms an integral part of the waste immobilisation aptitude of SYNROC. Calcium titanate can accommodate numerous radioisotopes within the two cation sites of its structure, with there being good evidence of the ability of $CaTiO_3$ to successfully accommodate different ions of a range of sizes and charges. The effect of the isotopes in the ^{90}Sr decay chain on the $CaTiO_3$ lattice will play an important role of assessing the feasibility of the material at different stages of the waste disposal process. How the lattice reacts to ^{90}Y and ^{90}Zr being apparent within it and how this changes the properties of the material will give an insight into its behaviour as a waste storage material. If secondary phases form or the cell is distorted drastically, the propensity of the waste isotopes to remain within the structure may deteriorate. As such, it is

imperative to assess such material behaviours at different concentrations of dopant in order to give a clear idea of what mechanisms may occur.

Computational simulation plays an important role in determining the effect of dopant incorporation, as synthesising and analysing these materials is not always viable. Computational techniques can give an insight on the atomic scale of how a structure may distort on addition of very small levels of impurity, such as the influence of substitutional defects on the structure. This again may not be practical to examine experimentally, so using a computational model can give this insight whilst overcoming the practical hurdles. The effect of Y and Zr doping on the A site of calcium titanate has not been extensively modelled beyond initial research, showing the possibility of separate phases occurring within the structure. Despite this, no definite conclusions have been made.[17, 23] Alongside this, the mechanism of how charge balances within the material upon Y/Zr incorporation or Sr decay is still not fully understood, with several possibilities as to how this may occur.[36] This leaves opportunity for a modelling approach to determine these questions, whilst shedding light on how the perovskite phase of SYNROC manages to successfully immobilise waste strontium.

Chapter 2: Computational Methodology

The starting point of an investigation into the structure and properties of crystalline solids is the production of a static model of the lattice and the energies associated with both the pure lattice and the defect structure. Atomistic simulation techniques can generate extended lattices of atoms and accurately examine their chemistry and material properties. These techniques can probe the properties of structures on the nanometre scale – a higher 'resolution' than experimental techniques, and therefore can examine phenomena that techniques such as X-ray diffraction cannot. The function of these techniques is to be used as a compliment to experimental methods, both confirming and predicting results. They can either construct a model from this experimental data or by using information generated by *ab initio* methods. Within this project the computational techniques used begin from experimental data, and one of the purposes of the experimental section of this report is to bring things full circle in showing how the data is originally collected. Alongside general material property investigations, atomistic simulation can also be used to examine large timescale behaviour and behaviour of materials in extreme environments, such as radiation damage and waste immobilisation in the nuclear industry.

The computational package used in this project is the General Utility Lattice Program (GULP), the details of which are described below, along with the potential model used and how predictions of crystal structures can be made from these techniques. GULP was originally developed by J D Gale for modelling of solids and clusters via force field and interatomic potential methods. It has the capability to model a wide range of

crystal structures from small clusters to extended bulk systems.[43, 44] The software is also able to utilise numerous different potential models and subsequently analyse many physical properties of the modelled material. As such it is a powerful tool for atomistic simulation and molecular dynamics calculations.

2.1: The Potential Model

In order to explain the interactions between ions in crystal systems, a 'potential model' needs to be derived to account for the level of interaction between particular ions. A potential model describes the potential energy at defined points in a range extending between two species. The second derivative of the energy at a point is the force applied to the system at that particular point. Two of the most common two-body potential models utilised in atomistic simulation are the Lennard-Jones and Buckingham potentials, both of which describe the potential energy at certain distances between the individual ions in the crystal. Other potentials such as the Morse or reactive models such as Reaxff and Comb potentials can be used for models with more covalency, or for differing environments within a single crystal.[45] Three-body terms can be used to describe repulsion between pairs of atoms and for bond angles, and four-body terms for torsion angles.

The Lennard-Jones potential, first described by J E Jones in 1924,[46] is regularly used to describe these interactions in covalent and ionic systems. The most common form of the Lennard-Jones potential is as follows:

$$V_{LJ} = 4\varepsilon\left[\left(\frac{\sigma}{r}\right)^{12} - \left(\frac{\sigma}{r}\right)^{6}\right]$$

Equation 2.1 – The Lennard-Jones 6-12 potential

Where ε is the depth of the potential well, r is the distance between the two atoms the potential is acting between and σ is the distance at which the potential is zero.

The Buckingham potential is an adaptation of the Lennard-Jones, with differing parameters, and is commonly used to describe interactions in crystals, though either can be used and adapted to fit the model under investigation. The parameters of the Buckingham potential have more repulsive and attractive terms for use in ionic systems, whereas Lennard-Jones and Morse potentials are more normally used for systems with some covalency. The regular form of the Buckingham potential used is:

$$\Phi(r) = Aexp\left(-\frac{r}{\rho}\right) - \frac{C}{r^6}$$

Equation 2.2 – The regular form of the Buckingham potential

Where A, ρ and C are constants and r is the interatomic distance. C is an attractive term with the A and ρ parameters accounting for repulsive interactions, such as that between the two electron clouds of the atoms. Additional coulombic terms are

sometimes used in addition to this basic term, which takes into account electrostatics when calculating the potential.

$$\Phi(r) = Aexp\left(-\frac{r}{\rho}\right) - \frac{C}{r^6} + \frac{q_1 q_2}{4\pi\varepsilon_0 r}$$

Equation 2.3 – The Buckingham potential with additional coulombic term

In the Coulomb-Buckingham potential the additional $\frac{q_1 q_2}{4\pi\varepsilon_0 r}$ term is used to describe the electric potential energy, with q_1 and q_2 being the charges of the two ions, r is the interatomic distance and ε_0 is the permittivity of a vacuum – 8.854x10^{-12} F/m.

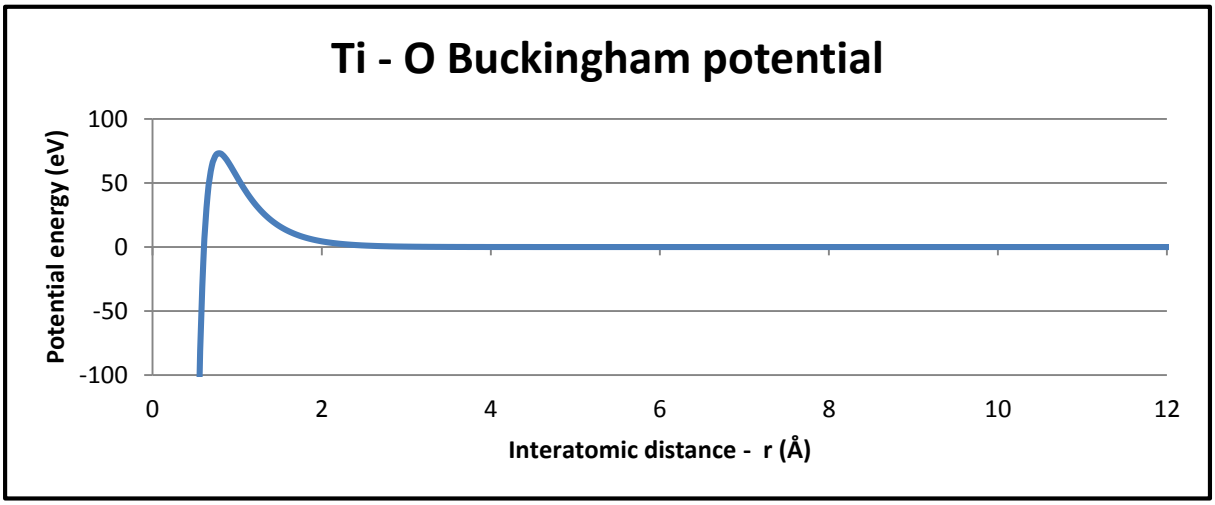

Graph 2.1 – Ti - O Buckingham potential from the Mather potential set[47]

The Buckingham potential is used extensively in this investigation due to both its suitability for the system and the wide range of potentials available for use with numerous different atoms. The potential is also easily variable with few parameters, making working with it considerably more straightforward than other potentials. Graph **2.1** shows the Ti - O Buckingham potential used in this investigation.

2.2: The Shell Model

In computational simulation both the interactions between the atoms in a structure and the interactions within the atom itself such as polarisability need to be considered. Developed by Dick and Overhauser in 1958, the 'shell model' describes the interaction between the inner and outer atom, described as a 'core' of the nucleus and inner electrons and a 'shell' of the valence electrons. This is used to describe the polarisability of an atom, with the rigid immovable core being attached by a harmonic spring of spring constant k to the shell. As 'k' increases, the rigidity of the spring increases and hence the polarisability of the ion decreases.[48] Within the Buckingham potential, the long range forces act on both the core and shell whereas the short range forces only act on the shell.

The polarisability of an ion in a vacuum is given by:

$$\alpha = \frac{q_s^2}{k_{cs}} \left(\frac{Shell\ Charge}{Force\ Constant}\right)$$

Equation 2.4 – Ionic polarisability

The force constant k is the spring constant, and sum of the shell charge q (E_{shell}) and the core charge E_{core} constitute the formal charge – oxidation state – of the ion.

The polarisability of an ion in a structure is heavily dependent on the environment surrounding said ion. The spring constant 'k' adds environment dependency to the model, dampening the polarisability along with the short range forces in the model. A non-cubic structure will always have this level of polarisation, whereas a cubic structure can be modelled without the need to incorporate this in the calculation due

to their symmetrical nature. In these cubic systems a rigid ion model is adequate for modelling of structural parameters.

A disadvantage of the shell model is that once the polarisability of the ion in a structure has been defined and the 'k' value set, any change in environment, for example a phase transition, will mean that the polarisations will now be incorrectly defined and the model will be invalid. Reactive forcefields can vary these parameters in response to environment change, but standard Buckingham potentials and the shell model cannot. $CaTiO_3$ is orthorhombic at room temperature, and can be accurately modelled with the shell model. However for cubic perovskites, where the shell model has been disregarded and rigid ions used, then changes in structure due to defect incorporation etc. will generate unphysical energy values.

2.3: Geometry Optimisation

GULP utilises numerous geometry optimisation methods when searching for minima, and has the ability to be used in conjunction with several others. When optimising the geometry of a structure, the internal energy of the given system is first defined, and then the minimum energy configuration of the structure is searched for on an energy surface. This surface can have many minima and maxima, and usually the minimum found by methods such as steepest descent are the local minima nearest the starting coordinates of the system. Finding the global minimum is considerably more difficult, so choosing a starting configuration likely to be close to the global minimum is

recommended. Experimental data such as X-ray structures is usually used as it is an ideal starting point close to the global minimum of a structure. Simulated annealing via Monte Carlo optimisation methods, genetic algorithms or MD can give a more thorough search of the potential energy surface with a greater chance of finding the global minimum from any particular starting point.

2.3.1: GULP Optimisation

GULP commonly uses conjugate gradient, steepest descent methods, and Newton-Raphson optimisation to find the minimum energy of a structure. A steepest descent method will be used to find the general location of a minimum and then Newton-Raphson can accurately find the minimum. These algorithms analyse the change in gradient of the energy surface in successive cycles as well as the change in energy and other variables between each cycle. Convergence is achieved when the changes in function, variables and gradient attain values under a 'threshold value', such as a gradient norm close to zero.

Newton-Raphson optimisation analyses the curvature of an energy surface when finding the minimum, and therefore takes a more 'direct' route and is accurate, but is slower than the gradient descent method. Another common method used by GULP is BFGS (Broyden-Fletcher-Goldfarb-Shanno) optimisation. This method calculates a 'Hessian matrix' which calculates the shape of the energy surface, and is used in

conjunction with Newton-Raphson in optimisation. The displacement vector of the current position to the minimum during the Newton-Raphson process is given by:

$$\Delta x = -H^{-1}g$$

Equation 2.5 – Displacement as a function of gradient and the Hessian matrix

Where Δx is the displacement vector, H is the Hessian and g is the gradient vector.

2.3.2: Simulated Annealing and MC

Energy minimisation using simulated annealing and Monte Carlo optimisation utilises changes in probabilities of a structure having a certain configuration. In successive cycles the free energy of atoms in a system decreases as they move from one configuration to another. The system initially has enough energy to explore the whole landscape and different minimums, before eventually sinking into a minimum as energy decreases. By giving a structure a defined 'energy' related to a temperature, and subsequently lowering the temperature, the energy and movement probability decreases and a global minimum can be found. At higher energies the structure can overcome many energy barriers, and 'jump' from one minimum to another easily in one step. As energy decreases, the distance the structure is able to 'jump' along the energy surface decreases, as well as the probability of such jumps happening. This means the structure will find a well and be unable to jump out of it, and eventually finding a minimum within the well. A search with constant energy and jump probability can then be undertaken to confirm that this minimum is global or local.

The system can be stopped from being trapped in a local minima by occasionally moving back to a more preferable state based on various restart criteria. For example there could be an inbuilt probability of a random jump to another point on the energy surface and restarting from this new position.

The probability of a move being accepted in a Monte Carlo algorithm is given by:

$$P = \exp\left(-\frac{\Delta U}{k_B T}\right)$$

Equation 2.6 – Probability of a move being accepted in a Monte Carlo algorithm

Where ΔU is the energy change of the move.

The Metropolis-Hastings criteria is also used to determine the acceptance of the next move based on the current set of values. Samples are drawn from a probability distribution P(x) and with each iteration the change in energy of current and sample values f(x) is compared with the desired probability distribution P(x). As the function f(x) increases in similarity with P(x) the probability of the candidate step being chosen in the next step increases.

2.4: Defect Simulation

Within a crystal lattice above absolute zero, the internal energy of the system is such that intrinsic stoichiometric defects are always present. These are defects which maintain the neutral charge of the crystal by movement of stoichiometric units of

atoms. An example of this in $CaTiO_3$ would be a unit of calcium oxide moving from the bulk of the lattice to the surface (to infinity) and leaving both a calcium and oxygen vacancy. This movement would maintain the neutral charge due to both a 2+ and 2- charged species being vacated. There are two main types of stoichiometric defect:

- **Schottky defect** – Where stoichiometric units of the crystal are removed from the bulk to the surface, as in the example above. This can either be a full Schottky such as removing a $CaTiO_3$ unit from $CaTiO_3$ or a smaller subset such as removal of CaO or TiO_2.
- **Frenkel defect** – Where an ion moves from its lattice point to an interstitial position elsewhere within the bulk material. This creates both a vacancy and an interstitial of the same ion, balancing charge.

Other possible defects in a crystal are non-stoichiometric and involve the incorporation of dopant impurities as interstitials or substituting onto an already occupied lattice site. All of these defects are measured by creating point defects in the crystal structure, of which there are three:

- **Vacancy** – The removal of an atom from a lattice site to infinity.
- **Interstitial** – The addition of an atom to a space between lattice sites which is normally unoccupied.
- **Substitutional defect** – The replacement of an atom on a lattice site by an impurity atom.

Additional non-stoichiometric defects exist within crystals, such as F-centres (colour centres) where an anion vacancy is filled with electrons, but will not be studied in this investigation.

2.4.1: Defect Simulation

Simulating defects in a crystal structure can be achieved via two methods, the Mott-Littleton method and the supercell method. Proposed by N. F. Mott and M. J. Littleton in 1938, the M-L method defines two spherical regions in a cluster around a point – the defect centre – in the crystal.[49] This point either lies on the initial defect site or at the central point of a cluster of defects. The inner sphere, labelled as region 1, contains the ions described as being strongly affected by the defect. These atoms are all allowed to relax around the defect and will individually move and be affected by it. Surrounding this, the ions in the outer sphere are described as being weakly affected by the defect, with their displacements and energies being approximated instead of explicitly calculated as in region 1. Though an approximation, this holds true if the perturbations in this region are relatively minor. This outer sphere is labelled as region 2a with region 2b being the remaining ions in the structure extending to infinity. Figure **2.1** describes these regions. The total defect energy of the cluster is then defined as the sum of the energies of both regions and between them. GULP uses Newton-Raphson minimisation to determine this energy.

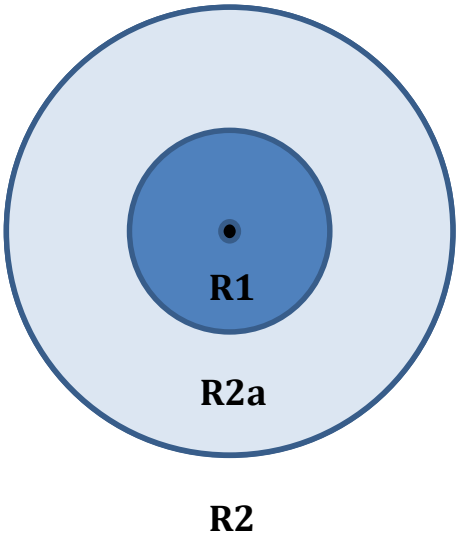

Figure 2.1: Inner sphere and outer sphere of a Mott-Littleton cluster. The Defect centre (black) is surrounded by a sphere of ions explicitly affected by the defect (dark blue), which is in turn surrounded by a sphere of ions where the effect of the defect is approximated (light blue).

The supercell method is an extension of bulk simulation methods where large concentrations of defects can be simulated within a cell and the total energy of the system then established. This is more suitable for large clusters of defects whereas the M-L method is more suitable for defects at infinite dilution.

When simulating defects in a structure using the M-L method, attention must be paid to the respective sizes of regions 1 and 2a, and how they affect the outcome of the defect calculation. A larger region radius generates a more accurate result, at the expense of increased computing time. The region 1 radius must also fully encompass the simulated defect or cluster in order to generate accurate results. Another consideration is the determination of the centre of the sphere, which if miscalculated can give erroneous results.

To test which region sizes were the most appropriate in the studied system, a size/time comparison using a Sr on Ca impurity in $CaTiO_3$ was undertaken. This defect was chosen due to it being one of the most common defects being investigated.

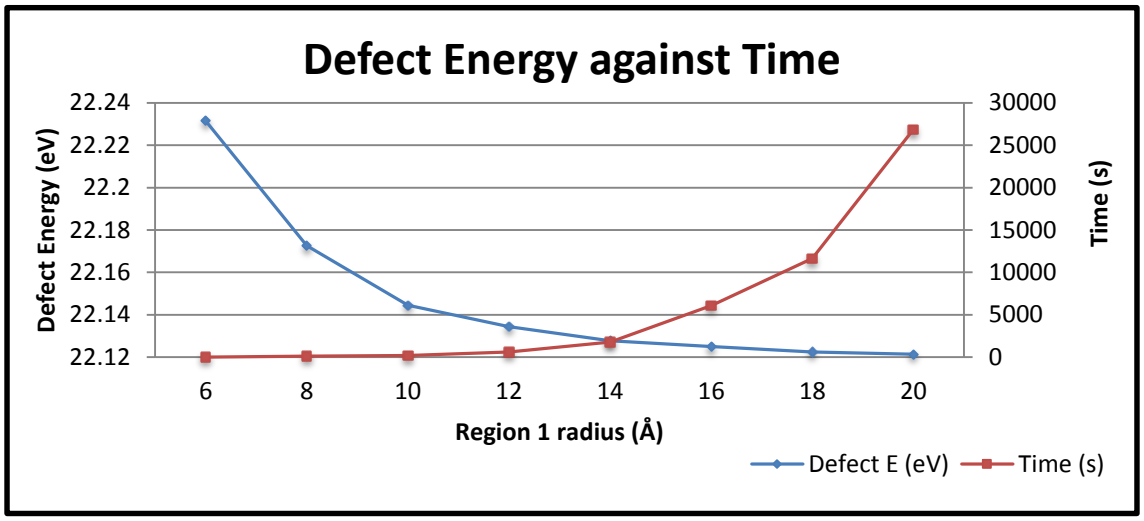

Graph 2.2 – Defect energy against time for a Sr on Ca defect in $CaTiO_3$

From the results of this, a region 1 radius of 14 Å was chosen as the ideal size – larger sphere sizes, though potentially giving more accurate results, came at the expense of considerably larger computing times. This radius both gave an accurate enough result and the calculation was completed in a time of ~1800 seconds, compared to 5000+ for larger defect radii. The 14 Å radius is large enough to encompass a sizeable defect cluster, being twice the length of the longest $CaTiO_3$ lattice parameter, which negates the possible errors from the defect not being fully encompassed.

Throughout this project, defect calculations are used to calculate solution energies and binding energies of different defect mechanisms for ions found in radioactive waste, in order to determine which is thermodynamically more favourable. The calculated favourability of certain defects can give insight into how the material is affected by these defects and subsequently how viable the target material is at radioactive waste immobilisation. With this in mind, defect incorporation studies are performed with Sr^{2+} cations due to its propensity in high level radioactive waste, then Y^{3+} and Zr^{4+} as the decay products in the ^{90}Sr decay chain. Other rare earths,

lanthanides and barium are also studied due to their chemical similarities to these elements.

Additionally, once the defect chemistry of the studied systems had been determined via the Mott-Littleton approach, simulated annealing using a Monte Carlo algorithm in a supercell was performed in a $CaTiO_3$ cell with significant concentrations of Sr defects. This gave information about the local environment of the defect on a larger scale than the Mott-Littleton 'point defect' approach.

Chapter 3: Experimental Methodology

The $Ca_{1-x}Sr_xTiO_3$ samples synthesised in this investigation were produced via two different synthetic routes, in order to determine which is more suitable for creating a pure, single phase product. Initially an aqueous route was used adapted from the method of Ball *et al.* (1998).[33] The results of this were then compared with the ceramic method. Powder XRD patterns were produced for each sample, and these were subsequently refined using Rietveld refinement.

3.1: Synthesis Methods

3.1.1: Aqueous Synthetic Route

The basis of this synthetic route is using a solution of nitrates to form the precursor. Ideally, once the precursor solution has been formed from the starting materials, a good level of homogeneity should be achieved by mixing. In the aqueous phase there would be a greater chance of achieving homogeneity than using solids, where not all of the materials are towards the surface of a grain and therefore not able to react.

Once a mixture of starting material has been achieved, the solution is then stir-dried and calcined to remove any residual organics before pelleting and high-temperature sintering. After sintering the pellet is reground, repelleted and resintered several times before a desired level of purity is achieved. This is tested by running powder XRD scans after each sintering step.

3.1.2: Solid State Synthesis

Solid state ceramic synthesis reactions are the most commonly used synthetic methods in solid state chemistry, involving a reaction between stoichiometric quantities of solid starting materials – commonly oxides as is the case here. The starting materials are ground together with a pestle and mortar or mill before pelleting and firing at high temperatures in a furnace. These temperatures can be upwards of 1000 °C. After firing, subsequent regrinding and refiring steps can be undertaken to bring more material towards grain boundaries. This encourages more material to react to achieve a higher degree of reaction.

Only material on the grain boundary or within a region where there is facile diffusion to the boundary is able to react. As such the degree of reaction of the product depends highly on the level of grinding achieved via the pestle and mortar – smaller grain sizes have a larger percentage of material near a boundary and able to react. A large grain size means a lot of material won't be able to be involved in the reaction. This is shown in figure **3.1**, showing different grain sizes in a solid state reaction, their grain boundaries, and their diffusion regions.

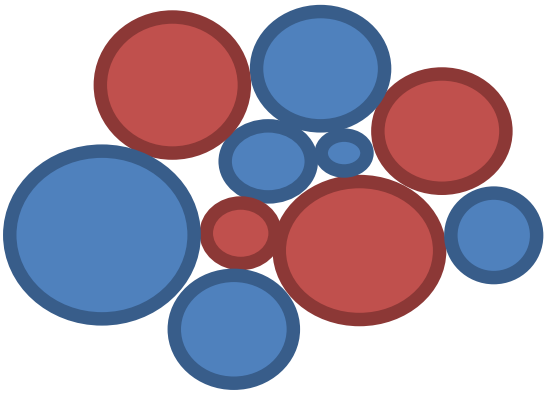

Fig. 3.1: A schematic of a variety of grains in a solid state reaction between two substances (red and blue). The dark edges are the regions where material is close enough to the boundary to diffuse and react. The larger grains contain a large amount of material which is not able to react due to being too far from the grain boundary. Hence it is preferable to undertake multiple grinding steps to achieve smaller grains and subsequently a higher degree of reaction.

3.2: Analysis: X-ray Diffraction

A powerful technique available to chemists to analyse the bulk structures of materials is X-ray diffraction. The interaction of X-rays with matter can provide insight into information such as the internal structures of crystals, how the atoms within them are arranged and whether a sample contains impurities and/or multiple phases.

3.2.1: Crystallography

Fundamentally, inorganic crystallography is focused on the analysis of repeating lattices of ions in particular orders and arrangements. Within each inorganic crystal are a series of repeating units – called unit cells – of a certain composition and symmetry which spread along the entire lattice. Unit cells are the smallest repeating

parallelogram in the structure and have defined lengths (a, b and c) and defined angles at the corners of each cell edge (α, β, and γ). These values are the 'lattice parameters' of each unit cell, and are major unique defining points of each crystal system. X-ray diffraction can be used to probe these parameters and gain insight into the bulk crystal structure of a material.

Table 3.1: The seven crystal systems and their defining length/angle relationships.

Crystal Systems		
Name	**Length relationship**	**Angle relationship**
Triclinic	$a \neq b \neq c$	$\alpha \neq \beta \neq \gamma \neq 90°$
Monoclinic	$a \neq b \neq c$	$\alpha = \gamma = 90° \neq \beta$
Orthorhombic	$a \neq b \neq c$	$\alpha = \beta = \gamma = 90°$
Tetragonal	$a = b \neq c$	$\alpha = \beta = \gamma = 90°$
Rhombohedral	$a = b = c$	$\alpha = \beta = \gamma \neq 90°$
Hexagonal	$a = b \neq c$	$\alpha = \beta = 90° \gamma = 120°$
Cubic	$a = b = c$	$\alpha = \beta = \gamma$

From: L. E. Smart and E. A. Moore, *Solid State Chemistry: An Introduction*, CRC Press, Boca Raton, Fl, USA, 4th edn., 2012

A crystal structure can be one of seven 'crystal systems' as outlined in table **3.1**, categorised by the relationship between the six lattice parameters. Crystal systems are additionally characterised by one of 14 'Bravais Lattices'. A Bravais lattice is a 3D combination of the seven crystal systems with one of seven lattice centrings, describing both the shape of the structure and the lattice points – locations of the atoms. An additional superset of this characterisation are the 230 'space groups', or possible unique crystal symmetries. The space group of a structure describes the crystal system, the centring and the symmetry operations of the structure. An example of this is the space group of $SrTiO_3$ – Pm-3m, which describes the $SrTiO_3$ structure as cubic with primitive centring, and having four mirror planes.

3.2.2: Diffraction and Bragg's Law

X-rays can interact with these crystal lattices in such a way that the different atomic arrangements can be distinguished. An X-ray beam is of a similar wavelength to the interatomic spacing within a crystal structure, of the angstrom order. As a result of this, the beam can therefore diffract due to the planes of atoms in the structure as a beam passes through the material. An X-ray beam entering a crystal at an angle θ is governed by Bragg's law (Eq. **3.1**), which equates the distance between two lattice planes with both this angle and the wavelength of the X-ray beam – λ.

$$n\lambda = 2d\sin\theta$$

Equation 3.1: Bragg's Law

When diffracted beams passing through the lattice interfere constructively, it means that the beams are in phase and Bragg's law is obeyed, meaning a distance d between the lattice planes and an integer number of planes n can be determined.

Using X-rays produced from different metal target materials in a diffractometer can be used to give a level of tunability in X-ray generation, with different targets producing X-rays of different wavelengths as a function of atomic number. Additionally, synchrotron X-ray data is considerably more tunable than lab diffractometers, and diffractometer configurations possible with synchrotrons can reach considerably better signal-to-noise ratios compared with lab-based equipment.

Diffraction of particles such as neutrons can also be used to gain information about a crystal structure. Neutrons interact with the nuclei of an atom, whereas X-rays

interact with the electron clouds surrounding them. Combined X-ray and neutron data sets can give a great amount of information on the nature of a crystal. Neutron diffraction cannot be performed in a lab and has to be undertaken in a national facility, limiting its availability, but is advantageous when determining magnetic structure and between atoms with similar electron configurations. For the purpose of this investigation, lab XRD analysis is adequate due to being considerably easier, cheaper and quicker, and the ions in the crystal are not adjacent to each other on the periodic table. This means that they have significantly different electronic configurations and can be characterised easier.

Diffraction experiments are the starting point of crystal system and space group determination, and additionally aid in the determination of the cell parameters of each unit cell in the material. They can also determine how many phases are present in a sample and give an idea of the level of crystallinity in the structure. Pattern analysis software can be used to compare a generated XRD pattern with an existing database of patterns to show similarities in peak location/width with literature examples and give an idea of the purity of a sample. Further analysis of powder XRD patterns can then be achieved via refinement methods such as Rietveld refinement, to gain a full understanding of the structure of a sample.

3.2.3: X-Ray Generation

In lab diffractometers, X-Rays are generated in 'X-ray tubes' comprised of a tungsten filament and a separate anode within a vacuum. This tube generates electrons which are then fired at a metal target – usually copper – which produces the X-rays as a product of the energisation/ionisation of electrons in the metal atoms. These X-rays are then monochromated to produce a wavelength of ~1.54Å (for copper targets). Not monochromating the X-ray beam will produce additional peaks in the PXRD pattern. This beam is then fired towards the sample mounted in the machine, where it interacts with the sample and the resultant intensities are then detected by a scintillation counter or CCD.

3.2.4: Powder X-ray Diffraction

XRD data in this investigation was collected using a Bruker D8 Advance powder X-ray diffractometer in transmission mode. The target metal was copper and the monochromator used was a germanium crystal, producing X-rays with a wavelength of 1.5406 Å. Powder samples were mounted with Scotch™ tape on low background plastic disk sample holders. The tape does not interact strongly with the X-rays making it ideally suited for the purpose. In the diffractometer, the sample was mounted on a rotating arm which enabled the sample to be angled and rotated round the instrument to scan over a range of 2θ values.

Generally, PXRD provides an average of every possible crystal orientation in a sample, and is faster than other methods such as single crystal XRD. Additionally, it does not require the growth of large crystal as in single crystal XRD and the sample can be easily prepared for analysis by making a fine powder.

3.3: Analysis: Rietveld Refinement

Rietveld refinement is a method of obtaining accurate crystal structure data from a powder diffraction pattern. In a refinement an experimental PXRD pattern is compared with and fitted to a calculated curve, the parameters of which can be adjusted in the refining process. Possible refinable parameters include:

- Background
- Zero-point
- Peak shape, intensity, position and FWHM
- Thermal parameters (U_{iso})
- Atomic positions
- Site occupancy

As the curve is fitted to a pattern, the difference between calculated and experimental data is minimised via a least-squares fit until a sensible 'χ^2' (goodness of fit) value of close to 1 is reached while still retaining physical parameters. This value is the square of the ratio of two 'R-factors' which derive from the given calculated and experimental data – R_{wp} and R_{exp}. R_{wp} is the weighted profile R-factor

and R_{exp} is the expected R-factor. The weighted profile is calculated from both observed and calculated data whereas the expected derives from observed data, the number of refined parameters and the number of observations. The outcome of this is a particularly accurate approximation of the fitted parameters if the χ^2 is low.

$$R_{wp} = \sqrt{\frac{\sum w_i(y_i - y_{ci})^2}{\sum w_i(y_i)^2}} \qquad R_{exp} = \sqrt{\frac{N-P-C}{\sum w_i(y_i)^2}}$$

Equations 3.2 and 3.3: Calculation of R_{wp} and R_{exp}

$$\chi^2 = \left(\frac{R_{wp}}{R_{exp}}\right)^2$$

Equation 3.4: Calculation of $\chi 2$

In equation **3.2**, R_{wp} is calculated from the weighting factor – w_i, and the calculated and observed intensities y_{ci} and y_i. In equation **3.3**, R_{exp} is calculated from the number of observables N, the number of refined parameters P, and the number of constraints used C, alongside the weighting factor and observed intensity. Equation **3.4** shows how these are then combined to form the χ^2 value.

The method was originally developed by H. M. Rietveld in 1969, and the General Structure Analysis System (GSAS) has been developed in order to utilise and analyse the data. In this investigation all the Rietveld refinements have been produced using EXPUI GSAS.[50, 51] The background, intensity, peak profile and thermal parameters were adjusted to get a good fit for lattice parameters and atomic positions for each structure in the $Ca_{1-x}Sr_xTiO_3$ series.

Chapter 4: Results and Analysis – Computational

"For a moment, nothing happened. Then, after a second or so, nothing continued to happen."

— Douglas Adams, The Hitchhiker's Guide to the Galaxy

4.1: Potential Set Determination

The first step in modelling the chemistry of a system is to be able to accurately produce the pure structures of the parent phases being examined. Different potential sets model systems with varying degrees of accuracy as a result of how the potentials were fit and to how many different parameters they were fit to. An ideal potential model will be able to reproduce as many physical properties of the parent phase as possible such as the lattice parameters, bulk modulus and dielectric properties.

There are several literature potential sets available for modelling calcium titanate, so in order to determine which was the most ideal for use they were each compared with experimental values for lattice parameters and bulk/shear moduli (Table **4.1**). For all of these potential sets, the crystal structure fitted to was that of S. Sasaki *et al*. (1987), gained from single crystal XRD data and subsequent refinement.[52] The bulk and shear moduli were taken from data collected by Y. D. Sinelikov *et al.* (1998)[53] and the static dielectric constant was taken from T. Fujii *et al.* (1993).[54]

Table 4.1: Comparison of $CaTiO_3$ models with experiment.

Experimental Comparisons							
	Exp	**Mather[47]**	**% Diff**	**Bush[55]**	**% Diff**	**Cherry[56]**	**% Diff**
K (GPa)	175(2)	211.39	18.83	294.43	50.88	208.36	17.40
G (GPa)	107(1)	110.26	3.00	161.11	40.36	115.91	7.99
'a' (Å)	5.4423	5.4446	0.04	5.2984	1.51	5.4940	0.95
'b' (Å)	7.6401	7.6802	0.53	7.4930	1.93	7.7468	1.40
'c' (Å)	5.3796	5.3907	0.21	5.2984	2.64	5.4259	0.86

K = Bulk Modulus, G = Shear Modulus, DEC = Static Dielectric Constant.

As a result of this comparison, the Mather potential set was determined to be the most ideal for modelling the calcium titanate system. Though the bulk modulus, shear modulus and static dielectric constant were all considerably different than the experimental values, this was the case for each of the potential sets. The calculated lattice parameters for the Mather potential set were particularly close to the experimental values, more so than the other sets. Consequently these were the most ideal for reproducing the experimental crystal structure.

It is also important to note which structures the potential sets were originally fit to, as this can also have an effect on the suitability of the potential set. If the potentials were not fit to ternary oxides, then they would not be able to be used with enough confidence that the results were accurate. The Bush potential set describes issues with its use with ternary oxides such as $CaTiO_3$, stating that they were initially derived for binary oxides then applied for ternary systems. Bush comments that though the potentials were successfully fit to ternary systems the choice of $Ti^{4+} - O^{2-}$ potential used was somewhat arbitrary and further refinement would be needed in order to have a fully rigorous potential set.[55] Conversely, the Mather system was

fitted specifically for $CaTiO_3$ and $CaTiO_3$-based systems, and therefore could be trusted more to give an accurate model of the system.

The chosen Mather potential set is as follows:

Table 4.2: Mather potential set. From G. C. Mather *et al.*, *Adv. Funct. Mater.*, 2007, **17**, 905-912.

Mather Potential Set				
Potential	**A**	**rho**	**C**	**Cutoff (Å)**
Ca^{2+} – O^{2-}	1340.18	0.3214	0.0	15.0
Ti^{4+} – O^{2-}	877.2	0.38096	9.0	15.0
O^{2-} – O^{2-}	22764.0	0.1490	43.0	15.0

Table 4.3: Core shell splits of ions. From G. C. Mather *et al.*, *Adv. Funct. Mater.*, 2007, **17**, 905-912.

Mather Core/Shell splits			
Atom	**Core**	**Shell**	**Spring**
Calcium	-1.135	3.135	110.2
Titanium	39.863	-35.863	65974.0
Oxygen	0.389	-2.389	18.41

4.2: Further Refinement

As the Mather potential set was fitted to model $CaTiO_3$ explicitly, and it has been seen that it fits the lattice parameters of the Sasaki structure particularly accurately, it can be trusted to model our studied system with similar accuracy. The remaining issue with this potential set is the lack of agreement with the mechanical properties of the material – bulk/shear moduli and the static dielectric constant. The three different potentials can each be altered individually to get a better fit, but this may cause an adverse effect on other parameters as this will change the nature of the entire potential. Consequently it would not be advised to just change other values in the potential willy-nilly to fit to another parameter.

However, variation of the spring constant and core-shell charge ratio can have an effect on the dielectrics of the material without affecting the other material properties. As such, an experiment to determine more ideal values for both the spring constant and charge ratio was devised and tested on the titanium ion values due to these seeming particularly large. By varying the different parameters over a range the static dielectric constant of the simulated material – initially 34.1559 – was brought more in line with the experimental value – 183. A piece of code was written that varies the spring constant in the GULP input file by a set value and outputs the resultant dielectric constant associated with the new spring value.

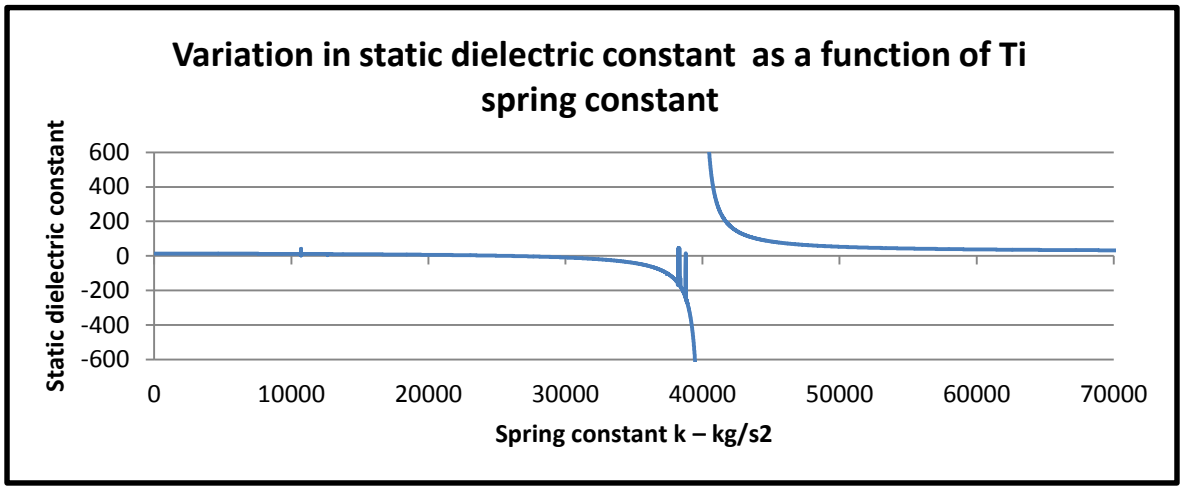

Graph 4.1: Variation in SDC as a function of spring constant

As can be seen in graph **4.1**, the static dielectric constant (DEC) can vary considerably with change in spring constant. Most notably there is a large feature at a k of ~40000 where the DEC tends to negative infinity, then returns from positive infinity to more realistic values. This is likely to not be an actual physical property of the material with this level of polarisability and therefore when finding the ideal spring constant this region would have to be avoided. Graph **4.2** shows a zoomed in version of figure **4.1** showing the ideal DEC value, from which the ideal spring constant can be determined.

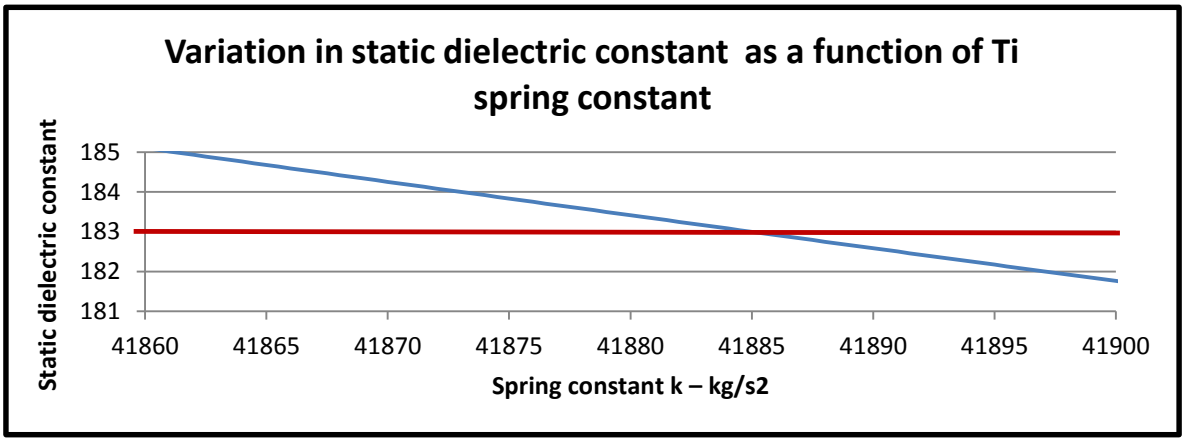

Graph 4.2: Showing zoomed in region where DEC value passes through 183 (red line) – the experimental DEC value.

This region, where the DEC is near 183, is located past the large feature, on the right hand 'tail'. It is also the only region where the DEC goes through 183, so there is no ambiguity that a Ti spring constant in this region is the most ideal for this system. Analysis of this result gives an ideal spring constant value of **41884.975** to give a DEC of 183 – when using literature core/shell values. Changing the core/shell values and charge ratio gives the effect of subsequently changing this ideal spring constant value, so this was also investigated.

To study this further, the ratio of core charge/formal charge (**R**) was varied through a range. **R** is described as:

$$R = \frac{E_{core}}{FC}$$

$$FC = E_{core} + E_{shell}$$

Equations 4.1 and 4.2: The core/shell charge ratio

Where E_{core} is the core charge, E_{shell} is the shell charge, and FC is the formal charge. The formal charge of Ti^{4+} is +4.

Table 4.4: Showing range of core/shell values and their resultant R

Core/Shell charge ratios								
E_{core}	E_{shell}	R	E_{core}	E_{shell}	R	E_{core}	E_{shell}	R
4	0	**1.0**	18	-14	**4.5**	32	-28	**8.0**
6	-2	**1.5**	20	-16	**5.0**	34	-30	**8.5**
8	-4	**2.0**	22	-18	**5.5**	36	-32	**9.0**
10	-6	**2.5**	24	-20	**6.0**	38	-34	**9.5**
12	-8	**3.0**	26	-22	**6.5**	40	-36	**10.0**
14	-10	**3.5**	28	-24	**7.0**			
16	-12	**4.0**	30	-26	**7.5**			

The literature R value used in the Mather potential set for titanium is 39.863, giving an R value of 9.966. Therefore the R values studied ranged between 1 and 10, as shown in table **4.4**.

The first effect identified by the changing of the R value was the change in both location and size of the large feature discussed previously. At low R values, the DEC goes to infinity at low k values, and the feature only affects a small number of k values. As R increases, so does the k value at which the feature occurs and the size of the feature. The outcome of this is that there seems to be a clear relationship between R and k, as shown in graph **4.4**. Graph **4.3** shows the results of the spring constant variation at different R values.

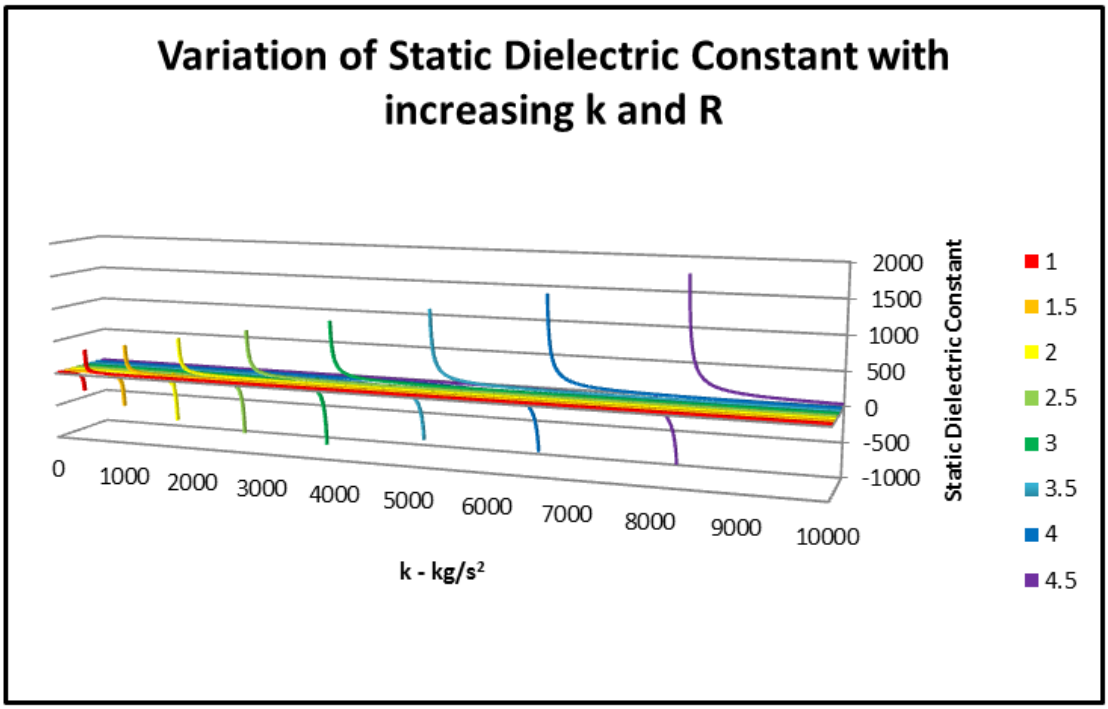

Graph 4.3: Graph of k against DEC, with varying R values from 1 to 4.5. R varies along the Z axis – Each different coloured line represents a different R. This shows that the feature both increases in size and k value with increasing R.

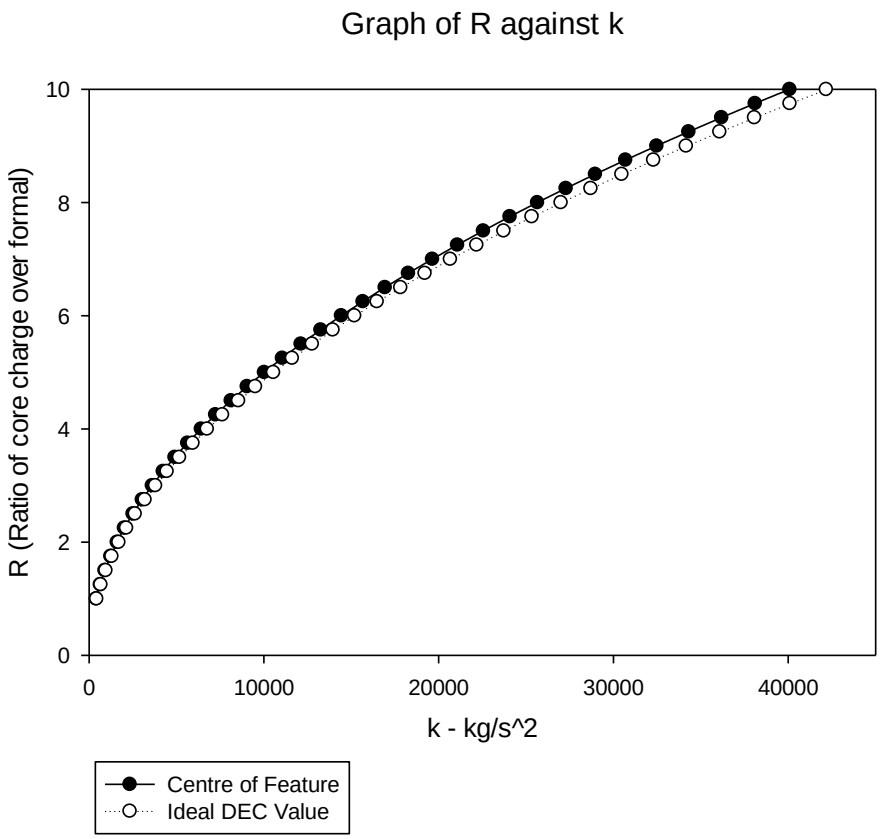

Graph 4.4: Graph of R against k, showing the relationship throughout every R value studied. Each point is the location of a feature. Also plotted is the ideal DEC value for each value of R and k.

This clear R – k relationship fits to the equation:

$$f = a * x^b$$

Where b = 0.5. Therefore:

$$f = a * \sqrt{X}$$

Where X = Spring Constant k.

Equations 4.3 and 4.4: The R – k relationship

As shown in graph **4.4**, the ideal DEC value also follows this trend.

The outcome of this is that in order to get a DEC value which is both close to the experimental value and not within the unphysical feature, both large R and k values are required. This justifies the choice of both core charge and spring constant of Ti by Mather *et al.* in their potential set, but it also shows that improvements can be made in order to get a more realistic result.

4.3: Potential Validation – Common Oxides

In order to validate the chosen literature potential sets further, the compatibility of each interatomic potential with each other must be examined. If the constituent oxides of a material cannot be produced with good accuracy in addition to the main material, then the cation potential cannot be used with certainty of producing accurate results in defect simulations.

For $CaTiO_3$, initially the potential set must also be able to produce both CaO and TiO_2. Comparison of the lattice energies of these would then determine whether formation of the titanate or the constituent oxides is more favourable. As TiO_2 can also form different polymorphs – rutile, anatase and brookite – this investigation can also conclude which of these is more favourable to form.

Summarised below (Tables **4.5-4.7**) are the calculated lattice parameters for the three TiO_2 polymorphs and their quality of fit to experimental (initial) data. For most parameters there is an accurate fit, with only the c parameters in rutile and anatase being slightly erroneous. Importantly they were all successfully modelled with the

Ti – O and O – O potentials chosen for the modelling of $CaTiO_3$, highlighting their compatibility. The bond angles (α, β, γ) all remained constant (90.0°) in each instance.

Table 4.5 – Rutile experimental data from D. M. Tobaldi *et al.* (2010)[57]

Rutile			
Parameter	**Initial**	**Calculated**	**% Difference**
a (Å)	4.59	4.53	-1.51
b (Å)	4.59	4.53	-1.51
c (Å)	2.96	3.23	9.09

Table 4.6 – Anatase experimental data taken from P. Ballirano and R. Caminiti (2001)[58]

Anatase			
Parameter	**Initial**	**Calculated**	**% Difference**
a (Å)	3.78	3.63	-4.00
b (Å)	3.78	3.63	-4.00
c (Å)	9.50	11.19	17.78

Table 4.7 – Brookite experimental data taken from I. Djerdj and A. Tonejc (2006)[59]

Brookite			
Parameter	**Initial**	**Calculated**	**% Difference**
a (Å)	5.16	5.33	3.19
b (Å)	9.18	9.54	3.86
c (Å)	5.43	5.39	-0.81

The calculated lattice energies of these polymorphs were then compared (Table **4.8**) in order to determine the lowest energy polymorph – that which would more readily be formed.

Table 4.8 – Calculated TiO_2 lattice energies

TiO_2	
Polymorph	**Lattice Energy (eV)**
Rutile	-112.35
Anatase	-112.49
Brookite	-112.26

From this study it is evident that the lowest energy TiO_2 polymorph is anatase – and therefore is the most thermodynamically stable. This anatase lattice energy value is used throughout this investigation as the TiO_2 energy.

Other oxides were also modelled both to determine potential compatibility and also so a set of lattice energies could be built up for defect calculations. The cations from these oxides were the ones used in the defect calculations in the remainder of this investigation. The quality of fit of the monovalent oxides to experimental data has been summarised in appendix 2 along with the potential set used, and the calculated lattice energies of the entire oxide set including $Ca/SrTiO_3$ are tabulated below.

Table 4.9 – Calculated oxide lattice energies

Oxide Lattice Energies	
Compound	**Lattice Energy (eV)**
CaO	-37.71
BaO	-32.58
SrO	-34.47
Ti_2O_3	-150.03
La_2O_3	-126.94
Nd_2O_3	-130.07
Gd_2O_3	-133.08
Y_2O_3	-135.71
Yb_2O_3	-137.70
ZrO_2	-111.38
$SrTiO_3$	-147.99
$CaTiO_3$	-150.88

4.4: Initial – Pure – Structure and Intrinsic Defects

Table 4.10 – Calculated $CaTiO_3$ lattice parameters with the Mather potential set

Calcium Titanate			
Parameter	**Initial**	**Calculated**	**% Difference**
a (Å)	5.44	5.45	0.04
b (Å)	7.64	7.68	0.53
c (Å)	5.38	5.39	0.21

Knowing that the literature potential set can recreate both the pure $CaTiO_3$ structure (Table **4.10**) and various relevant oxides, the results of defect calculations using this set can now be accepted with a reasonable degree of confidence. Firstly the intrinsic (Schottky and Frenkel) point defects of the material can be examined before moving on to substitutional defects. The Schottky defect occurs when charge balanced ions leaves their lattice sites creating vacancies. Both these and Frenkel defects occur naturally in stoichiometric units, preserving the charge of the crystal. The Frenkel defect creates both a vacancy and an interstitial defect as an atom moves from an original lattice position but does not remove itself to infinity – instead it moves through the lattice to a new interstitial location. The mechanisms of Schottky and Frenkel defects in $CaTiO_3$ are as shown:

$$Ca_{Ca}^{x} + Ti_{Ti}^{x} + 3O_{O}^{x} \rightleftharpoons V_{Ca}^{''} + V_{Ti}^{''''} + 3V_{O}^{\bullet\bullet} + CaTiO_3$$

$$Ca_{Ca}^{x} + O_{O}^{x} \rightleftharpoons V_{Ca}^{''} + V_{O}^{\bullet\bullet} + CaO$$

$$Ti_{Ti}^{x} + 2O_{O}^{x} \rightleftharpoons V_{Ti}^{''''} + 2V_{O}^{\bullet\bullet} + TiO_2$$

Equations 4.5 – 4.7 – A full Shottky, a calcium Schottky and a titanium Schottky defect

$$Ca_{Ca}^{x} \rightleftharpoons V_{Ca}'' + Ca_{i}^{\bullet\bullet}$$

$$Ti_{Ti}^{x} \rightleftharpoons V_{Ti}'''' + Ti_{i}^{\bullet\bullet\bullet\bullet}$$

$$O_{O}^{x} \rightleftharpoons V_{O}^{\bullet\bullet} + O_{i}''$$

Equations 4.8 – 4.10 – A calcium Frenkel defect, a titanium Frenkel defect and an oxygen Frenkel defect

Table 4.11 – Calculated intrinsic defects in $CaTiO_3$.

Intrinsic Defects			
Defect	**Lit Value (eV)[47]**	**Calculated* (eV)**	**% Difference**
Ca Schottky	2.92	2.01	0.98
Ti Schottky	3.03	2.97	1.55
Full Schottky	2.49	2.45	1.58
Ca Frenkel		4.32	
Ti Frenkel		8.45	
O Frenkel		3.17	

*Average value per defect

As summarised in Table **4.11**, in calcium titanate simulations show that the lowest energy intrinsic defect was a Ca Schottky defect, with Ca^{2+} and O^{2-} ions migrating to the surface and producing CaO. Second to this was a full $CaTiO_3$ Schottky defect, followed by a Ti Schottky. Frenkel defects were much higher energy in comparison and subsequently less likely to form. For both defect types, a movement of the titanium atom is the least favoured. Within the calcium titanate structure there is little room for interstitials between the atomic sites, which would be why this type of defect is less favourable.

4.5: Substitutional Defects

In a waste immobilisation context, the effect of substitutional defects will give a good understanding of how the lattice is affected by waste incorporation. Incorporating strontium and barium ions, due to their prevalence in HLW, are of considerable concern, and calcium titanate should readily incorporate these due to their similar chemistries. A solid solution exists between $CaTiO_3$ and $SrTiO_3$ so interchanging Sr and Ca in the system should be particularly facile.

There are numerous literature sources which examine dopant incorporation into these structures, notably Mather *et al.* (2007) which explores several dopants and is the source of the potential set for the pure $CaTiO_3$ structure.[47] Buscaglia *et al.* (2001) and Freeman *et al.* (2011) both examine dopant incorporation into $BaTiO_3$, and look at charge compensation when incorporating ions of different charges.[15, 35] $CaTiO_3$ and $SrTiO_3$ have both been examined in some detail by Dawson *et al.* (2013) who also looked at charge compensation mechanisms which may occur on doping.[36] Initially dopants with a 2+ charge were studied, followed by examining lanthanides and rare earths with a 3+ charge and finally Zr^{4+}, following the trend present in the decay chain of ^{90}Sr.

The results of the substitutional defect calculations are summarised in tables **4.12** and **4.13**, which reveal several trends based upon the variation of ionic radius in the dopant cation.

Table 4.12 – Substitutional defects on Ti and Ca sites in $CaTiO_3$ for 2+ charge impurities

Substitutional Defects	
Defect	**Calculated (eV)**
Ca on Ti	58.88
Ti on Ca	-55.00
Sr on Ca	3.45
Sr on Ti	63.24
Ba on Ca	5.97
Ba on Ti	66.29

Of particular interest is the higher defect energy when there is a difference in charge between the dopant cation and the initial cation that occupied the site. Impurities on the titanium site have considerably higher defect energies than those on the calcium site, a trend which continues with the lanthanide impurities. Additionally Ba on Ca impurities have higher defect energies than Sr on Ca, due primarily to the size difference as the Sr impurities are closer in ionic radius to the replaced Ca.

Table 4.13 – Substitutional defects on Ti and Ca sites in $CaTiO_3$ for 3+ and 4+ charge impurities.

Substituitonal Defects – Lanthanides, rare earths and zirconium			
Defect	**Calculated (eV)**	**Defect**	**Calculated (eV)**
La on Ca	-16.14	La on Ti	42.85
Nd on Ca	-17.88	Nd on Ti	40.72
Gd on Ca	-19.43	Gd on Ti	38.78
Y on Ca	-20.74	Y on Ti	37.18
Yb on Ca	-21.70	Yb on Ti	35.95
Zr on Ca	-54.13	Zr on Ti	1.90
		Ti^{3+} on Ti^{4+}	28.77

It is also noticeable from table **4.13** that the Zr on Ti impurity has a considerably smaller defect energy than that of the other Ti-site impurities. In this case the 4+ charge is retained and the ionic radius does not change as much as in the other cases, explaining the more facile substitution.

These values, taken with the formation energy of the respective oxides of the impurities, give a value for the solution energy of each impurity. This solution energy can give an idea as to which is the most favourable thermodynamically and most likely to occur. For calcium titanate several different mechanisms of dopant charge compensation exist, each with differing solution energies. Both the Ca^{2+} and Ti^{4+} sites in the crystal can be substituted, and as the Ln/REE^{3+} ions are both mid-sized and have intermediate charge this examination can uncover the ideal impurity site in addition to the most favourable impurity.

4.6: Solution Energies

4.6.1: 2+ Charged Impurities

For 2^+ cation incorporation in $CaTiO_3$ the two sites can be doped via two mechanisms – one simple substitution onto the Ca^{2+} site (equations **4.11** and **4.12**) and one onto the Ti^{4+} site, with the production of an oxygen vacancy to balance charge (equations **4.13** and **4.14**). Shown below are the two mechanisms using Sr^{2+} incorporation as an example. These mechanisms would also hold true for Ba^{2+} and other 2+ cations. The respective solution energies are summarised in table **4.14**.

- Substitution of Sr^{2+} at Ca^{2+} site:

$$SrO + Ca_{Ca} \rightarrow Sr_{Ca} + CaO$$

$$E_s = Sr_{Ca} + CaO - SrO$$

- Substitution of Sr^{2+} at Ti^{4+} site with O^{2-} vacancy compensation:

$$SrO + Ti_{Ti} + O_O \rightarrow Sr''_{Ti} + V_O^{\bullet\bullet} + TiO_2$$

$$E_s = Sr''_{Ti} + V_O^{\bullet\bullet} + TiO_2 - SrO$$

Equations 4.11 – 4.14: Sr^{2+} doping into $CaTiO_3$ at both Ca^{2+} and Ti^{4+} site.

Table 4.14: Solution energies for 2+ ion doping in $CaTiO_3$

Solution Energies	
Defect	**Solution energy (eV)**
Sr on Ca	0.21
Ba on Ca	0.85
Sr on Ti	4.81
Ba on Ti	5.98

From these results it is clear that the more favourable site for Sr^{2+} and Ba^{2+} incorporation is the Ca^{2+} site, and it is particularly unfavourable for any doping to occur on the Ti^{4+} site. Also notable is the very small energy value for Sr^{2+} incorporation, which supports why substitution is favourable and plays a major part in how the $CaTiO_3$ and $SrTiO_3$ form a solid solution.

4.6.2: 3+ Charged Impurities and Charge Compensation

For 3+ charged impurities many more charge compensation mechanisms can exist, with five being described in the literature [15, 35, 36] and several other mechanisms possible.

- **Scheme 1:** Substitution of M^{3+} at Ca^{2+} with conduction electron (titanium reduction) compensation:

$$M_2O_3 + 2Ca_{Ca} \rightarrow 2M^{\bullet}_{Ca} + \frac{1}{2}O_2 + 2e' + 2CaO$$

$$E_s = \frac{1}{2}[2M^{\bullet}_{Ca} + 2Ti^{3+}_{Ti^{4+}} + 2e' - \left(\frac{1}{2}D_{O_2} + EA_{O^{2-}}\right) + 2CaO - M_2O_3]$$

(Equations 4.15 – 4.16)

In scheme 1 the metal ion is substituted onto the Ca^{2+} site and charge compensation is achieved via reduction of a Ti^{4+} species to Ti^{3+}. The theory behind this scheme is the Ti^{4+} acting as an 'electron sink' for excess electrons in the structure. Reduction of a species in a reaction is a complex process, and therefore several additional terms are required to fully explain the mechanism. The energy required for a Ti^{4+} ion to gain an electron (e') needs to be considered, as well as the the dissociation energy of oxygen (D_{O_2}) and second electron affinity of oxygen ($EA_{O^{2-}}$) (Both in table **4.15)**. The second electron affinity of oxygen is heavily environment dependant, and therefore is different for each substituted ion. The values used for each environment are shown in table **4.16**. This electron sink behaviour is a possible explanation for how charge compensates during radioactive decay of β^- emitters such as ^{90}Sr.

Table 4.15: Dissociation energy of an O_2 molecule and the energy required for Ti^{4+} reduction to Ti^{3+} on gaining an electron. From *CRC Handbook of Chemistry and Physics*, ed. D. R. Lide, CRC Press, Boca Raton, FL, USA, 86th edn., 2005

Energy values used in Scheme 1 (eV)	
O_2 Dissc. E.	5.165
e'	-43.27

Table 4.16: 2nd electron affinities of O^{2-} ion doping in $CaTiO_3$ for different rare earth compounds.

2nd Electron Effinities (eV)	
Compound	**EA – O^{2-}**
La_2O_3	7.53
Nd_2O_3	6.76
Gd_2O_3	7.23
Y_2O_3	7.29
Yb_2O_3	6.90

From C. L. Freeman *et al., J. Mater. Chem.*, 2011, **21**, 4861-4868 (La-Gd, Yb) And calculated from cohesive energies given in *CRC Handbook of Chemistry and Physics*, ed. D. R. Lide, CRC Press, Boca Raton, FL, USA, 86th edn., 2005. (Y)

In both $SrTiO_3$ and $CaTiO_3$ the literature value of the solution energy associated with this is particularly high, for example 12.56 eV for an La^{3+} impurity.[36] This, compared to the calculated energies of Sr/Ba defects of less than 1 eV suggests that this mechanism must be very unfavourable.

Table 4.17: Solution energy results for scheme 2, both in a cluster and at infinite dilution

Solution Energies – Scheme 1 (eV)					
Element	**Inf. Dil. E.**	**Cluster. E.**	**Binding E.**	**Inf. Sol. E**	**Clus. Sol. E.**
La	66.94	67.04	0.10	10.91	10.96
Nd	63.47	63.57	0.11	11.12	11.18
Gd	60.36	60.48	0.11	10.84	10.90
Y	57.75	57.86	0.12	10.82	10.88
Yb	55.83	55.94	0.11	11.10	11.16

The calculated solution energies for this scheme (table **4.17**) show that for 3+ ion incorporation this scheme is particularly unfavourable. This is in agreement with the literature results. It is also notable that the binding energies of the defect clusters are positive, suggesting that this defect prefers to be at infinite dilution over being clustered, though the energy is very small. Notably there seems to be no trend with

ionic radius, which may be due to the environment dependant electron affinity term which also is not related to radius.

- **Scheme 2:** Substitution of M^{3+} at Ca^{2+} with Ti^{4+} vacancy compensation:

$$2M_2O_3 + 4Ca_{Ca} + Ti_{Ti} \rightarrow 4M_{Ca}^{\bullet} + V_{Ti}^{''''} + 3CaO + CaTiO_3$$

$$E_s = \frac{1}{4}[4M_{Ca}^{\bullet} + V_{Ti}^{''''} + CaTiO_3 - 3CaO - 2M_2O_3]$$

(Equations 4.17 – 4.18)

In scheme 2 (equations **4.17** and **4.18**) the metal ion is substituted onto the Ca^{2+} site and charge compensation is achieved via a titanium vacancy. The Ti^{4+} and Ca^{2+} produce CaO and $CaTiO_3$ on the surface (at infinity) upon leaving the structure. A $CaTiO_3$ molecule is produced over CaO and TiO_2 due to the slightly lower lattice energy of the ternary oxide compared to that of the two binary oxides combined meaning formation is preferable. Out of the all charge compensation mechanisms studied scheme 2 involves the most atomic positions, with five – four Ca^{2+} sites and one Ti^{4+} site – having a role in the mechanism. These sites are shown in figures **4.1** and **4.2**.

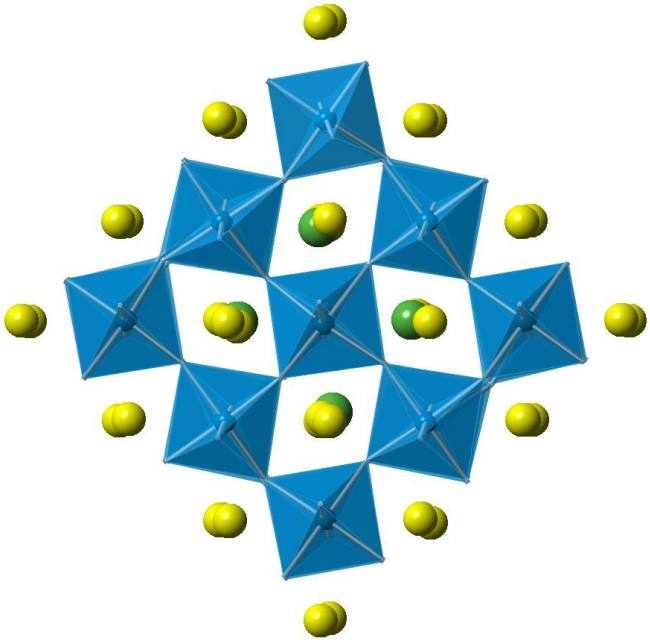

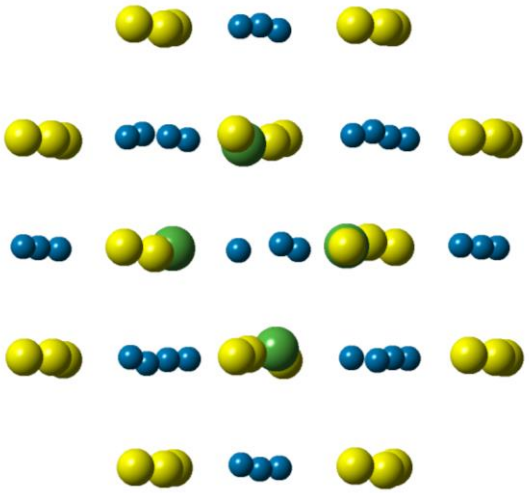

Fig. 4.1 (left) and Fig. 4.2 (below): Cross section of $CaTiO_3$ with four Lanthanum impurities and a Titanium vacancy. Note how due to the large size of the La^{3+} ions they distort the lattice, and each ion lies closer to the centre of the cluster, where the Ti^{4+} vacancy is present.

Table 4.18: Solution energy results for scheme 2, both in a cluster and at infinite dilution.

Solution Energies – Scheme 2 (eV)					
Element	**Inf. Dil. E.**	**Cluster. E.**	**Binding E.**	**Inf. Sol. E**	**Clus. Sol. E.**
La	17.62	14.93	-2.69	1.88	1.20
Nd	10.68	8.36	-2.32	1.71	1.13
Gd	4.47	2.41	-2.07	1.66	1.14
Y	-0.76	-2.65	-1.90	1.67	1.19
Yb	-4.60	-6.45	-1.86	1.75	1.29

From the results for this scheme (table **4.18**) there are two trends which are immediately apparent. Firstly, the solution energies for each impurity element where the defects are clustered together are lower than that at infinite dilution. This means that each defect prefers to cluster together in the structure. Secondly, the solution energies tend to increase as the impurity element decreases in size, with the exception of Lanthanum. This may be due to lanthanum being too large for the

structure and the ideal impurity radius being close to that of neodymium. The smaller elements may be too small to comfortably fit in the structure and hence pose the same issue as lanthanum. The impurity with the lowest solution energy was neodymium with 1.13 eV. Compared with scheme 1, the energy values for this scheme are all ~10 eV lower, which highlights the unfavourability of that mechanism.

- **Scheme 3:** Substitution of M^{3+} at Ti^{4+} with O^{2-} vacancy compensation:

$$M_2O_3 + 2Ti_{Ti} + O_O \rightarrow 2M'_{Ti} + V_O^{\bullet\bullet} + 2TiO_2$$

$$E_s = \frac{1}{2}[2M'_{Ti} + V_O^{\bullet\bullet} + 2TiO_2 - 2M_2O_3]$$

(Equations 4.19 – 4.20)

In scheme 3 (equations **4.19** and **4.20**) the metal ion is substituted onto the Ti^{4+} site (fig. **4.3**) with charge compensation being achieved via the creation of oxygen vacancies. This incorporation method differs from the previous two due to the resultant substitutional defect being negatively charged. To combat this increase in negative charge an oxygen anion is removed creating TiO_2 on the surface.

Table 4.19: Solution energy results for scheme 3, both in a cluster and at infinite dilution.

Solution Energies – Scheme 3 (eV)					
Element	**Inf. Dil. E.**	**Cluster. E.**	**Binding E.**	**Inf. Sol. E**	**Clus. Sol. E.**
La	105.31	104.14	-1.17	3.63	3.05
Nd	101.03	100.04	-0.99	3.06	2.56
Gd	97.17	96.58	-0.58	2.63	2.34
Y	93.97	93.46	-0.51	2.35	2.09
Yb	91.50	91.05	-0.45	2.16	1.93

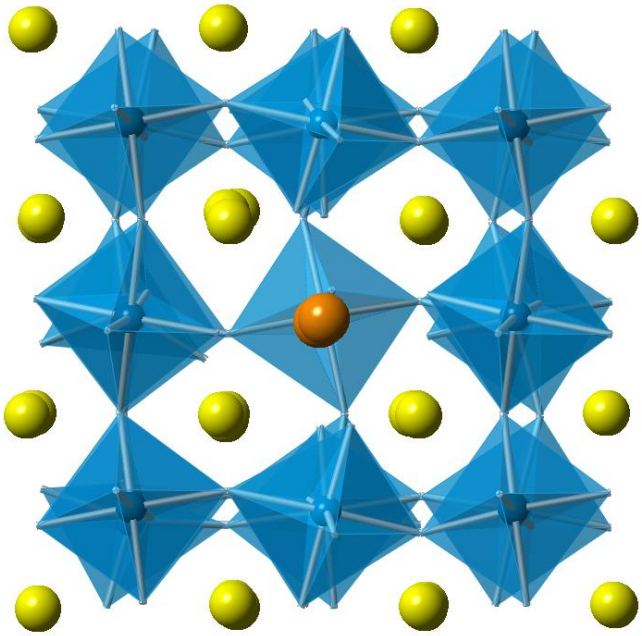

Fig. 4.3: Cross section of $CaTiO_3$ with two neodymium atoms replacing titanium as in scheme 3. There is considerable additional tilting of the TiO_6 octahedra around the defect site.

The main trends apparent with scheme 3, as shown in table **4.19**, are the much clearer relationship between size and solution energy in comparison with scheme 2. There is a substantially greater energy difference between the different elements with the Yb energy over 1 eV smaller than the La energy – 1.93 eV compared to 3.05 eV. The relationship is also more linear than with scheme 2, possibly due to all of the elements being too large for the B site. Additionally, the solution energies for this scheme are all particularly high, showing the unfavourability of dopant incorporation on the B site.

- **Scheme 4**: Substitution of M^{3+} at Ca^{2+} and at Ti^{4+} with self-compensation:

$$M_2O_3 + Ti_{Ti} + Ca_{Ca} \rightarrow M'_{Ti} + M^{\bullet}_{Ca} + CaTiO_3$$

$$E_s = \frac{1}{2}[M^{\bullet}_{Ca} + M'_{Ti} + CaTiO_3 - M_2O_3]$$

(Equations 4.21 – 4.22)

In scheme 4 (equations **4.21** and **4.21**) dopants are incorporated onto both the Ca^{2+} and Ti^{4+} sites, with the subsequent charge imbalances cancelling each other out and a $CaTiO_3$ unit being produced. The substitutional defects here are therefore overall charge neutral with no need for additional vacancies to be produced to compensate.

Table 4.20: Solution energy results for scheme 4, both in a cluster and at infinite dilution.

Solution Energies – Scheme 4 (eV)					
Element	**Inf. Dil. E.**	**Cluster. E.**	**Binding E.**	**Inf. Sol. E**	**Clus. Sol. E.**
La	26.71	26.52	-0.19	1.39	1.29
Nd	22.84	22.68	-0.16	1.02	0.94
Gd	19.35	19.21	-0.14	0.78	0.70
Y	16.45	16.31	-0.14	0.64	0.57
Yb	14.25	14.13	-0.12	0.59	0.53

Scheme 4 has some of the lowest overall solution energies shown so far for the 3+ charge compensation mechanism, as shown in table **4.20**. As evidenced in figures **4.4** and **4.5** there is not significant distortion of the lattice when the elements are incorporated. All of the cluster values apart from lanthanum are below 1 eV, with ytterbium being the lowest at 0.53 eV, and as with scheme 3 the solution energy decreases with ionic radius and the most favourable mechanism is Yb incorporation. There are very low binding energies for the various clusters, showing affinity for cluster formation over infinite dilution but not by a great margin.

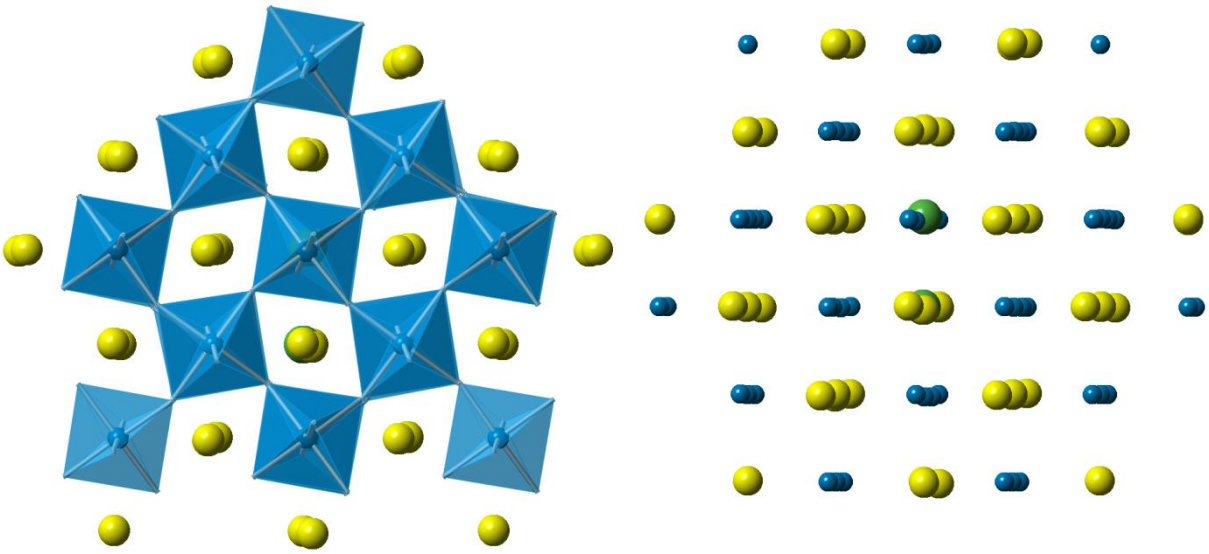

Fig. 4.4 (left) and Fig. 4.5 (right): Two lanthanum impurities self-compensating in the $CaTiO_3$ structure. There is no great noticeable distortion of the lattice or the octahedra despite the large size of the dopant cations. Some cation sites are pushed away from the defect centre.

- Scheme 5: Substitution of M^{3+} at Ca^{2+} with Ca^{2+} vacancy compensation:

$$M_2O_3 + 3Ca_{Ca} \rightarrow 2M_{Ca}^{\bullet} + V_{Ca}'' + 3CaO$$

$$E_s = \frac{1}{2}[2M_{Ca}^{\bullet} + V_{Ca}'' + 3CaO - M_2O_3]$$

(Equations 4.23 – 4.24)

In scheme 5 (equations **4.23** and **4.24**) the entire mechanism involves Ca^{2+} sites with the Ti^{4+} playing no part. Two M^{3+} cations incorporate onto Ca^{2+} site and one Ca^{2+} vacancy is produced to counter the charge imbalance.

Fig. 4.6 (left) and Fig. 4.7 (right): Three neodymium impurities incorporating onto Ca^{2+} sites in the $CaTiO_3$ structure, accompanied by a Ca^{2+} vacancy. There is some distortion in the octahedral tilts but the structure is not dramatically affected.

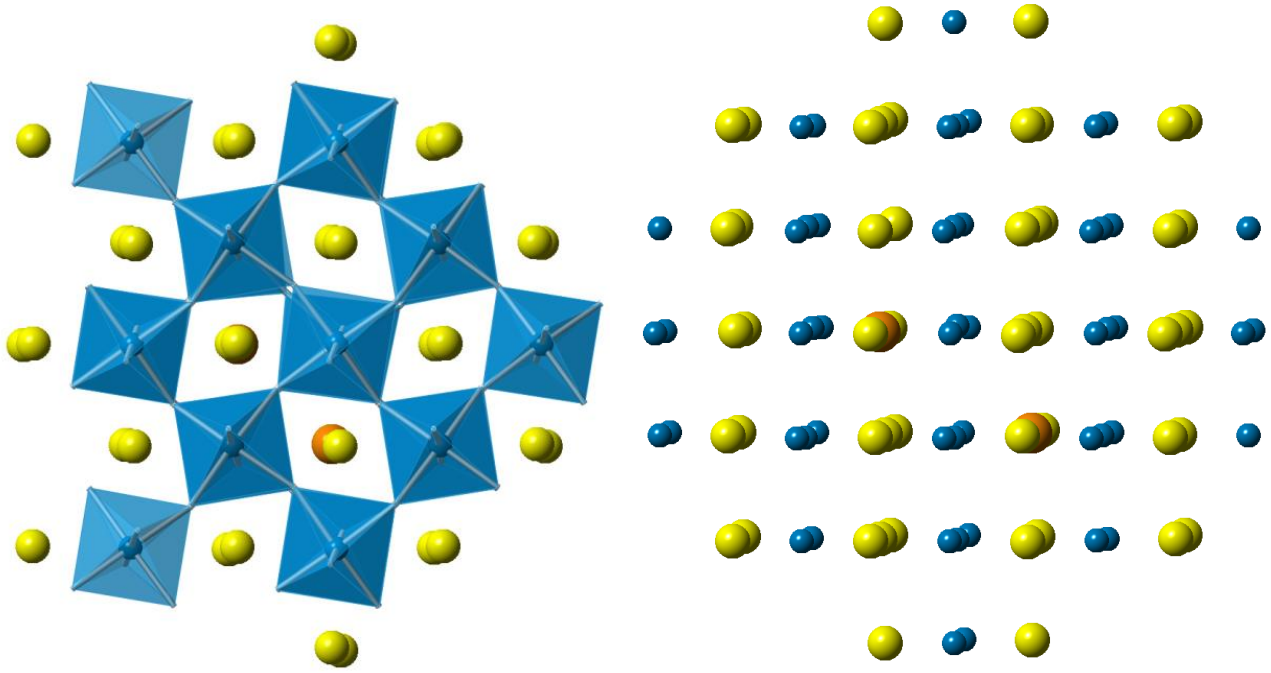

Table 4.21: Solution energy results for scheme 5, both in a cluster and at infinite dilution.

Solution Energies – Scheme 5 (eV)					
Element	**Inf. Dil. E.**	**Cluster. E.**	**Binding E.**	**Inf. Sol. E**	**Clus. Sol. E.**
La	-10.16	-10.76	-0.61	1.83	1.53
Nd	-13.63	-13.94	-0.32	1.66	1.51
Gd	-16.73	-17.25	-0.52	1.61	1.35
Y	-19.35	-19.69	-0.34	1.62	1.45
Yb	-21.27	-21.75	-0.48	1.71	1.47

For the range of elements studied, there was surprisingly little variation in solution energy – 0.18 eV – between the highest (La) and the lowest (Gd). It is also interesting to note that there is no linear correlation with ionic radius, with lanthanum and ytterbium both having similar energy values and the lowest being the mid-sized gadolinium. The trend of values is more parabolic with Gd as the minimum. The

energy values for scheme 5 are higher than for both schemes 2 and 4, despite scheme 2 having more Ca^{2+} sites being doped and vacated in the cluster.

- Scheme 6: Substitution of M^{3+} at Ca^{2+} with O^{2-} interstitial compensation:

$$M_2O_3 + 2Ca_{Ca} \rightarrow 2M_{Ca}^{\bullet} + O_i'' + 2CaO$$

$$E_s = \frac{1}{2}[2M_{Ca}^{\bullet} + O_i'' + 2\mathrm{CaO} - M_2O_3]$$

(Equations 4.25 – 4.26)

In scheme 6 (equations **4.25** and **4.26**) the charge is balanced by introduction of an interstitial oxygen into the lattice framework. It has been seen that Frenkel defects in $CaTiO_3$ are unfavourable, with the oxygen Frenkel energy being 3.17 eV, so consequently it can be theorised that this mechanism may also be unfavourable.

When simulating defect clusters for scheme 6 it was found that for gadolinium, neodymium and lanthanum there were unphysical interactions generated between the atoms in the structure as they were brought too close together. This is a consequence of both large impurities and an additional atom being located near each other in a small space, and the Buckingham potential being unphysically attractive at short distances. These were not present in yttrium and ytterbium, possibly due to their smaller ionic radii being more accommodating of the interstitial oxygen. At infinite dilution the defects were able to be accommodated but the solution energies were still particularly unfavourable.

Table 4.22: Solution energy results for scheme 6, both in a cluster and at infinite dilution.

Solution Energies – Scheme 6 (eV)					
Element	**Inf. Dil. E.**	**Cluster. E.**	**Binding E.**	**Inf. Sol. E**	**Clus. Sol. E.**
La	-45.56			2.99	
Nd	-49.03			2.82	
Gd	-52.13			2.77	
Y	-54.75	-53.98	0.77	2.78	3.16
Yb	-56.67	-55.24	1.43	2.86	3.58

Table **4.22** shows the generated energy values, and shows that the mechanisms for all the elements are more favourable at infinite dilution. Y and Yb defects have positive binding energies, and the others are unable to form clusters due to size restrictions. The solution energy trend is more curved than linear, with the lowest energy being for gadolinium (2.77 eV) as with scheme 5.

- Scheme 7: Substitution of M^{3+} at Ca^{2+} with Ca^{2+} at Ti^{4+} compensation:

$$M_2O_3 + 2Ca_{Ca} + Ti_{Ti} \rightarrow 2M_{Ca}^{\bullet} + Ca_{Ti}'' + CaTiO_3$$

$$E_s = \frac{1}{2}[2M_{Ca}^{\bullet} + Ca_{Ti}'' + CaTiO_3 - M_2O_3]$$

(Equations 4.27 – 4.28)

This scheme (equations **4.27** and **4.28**) can be best described as two Ca^{2+} ions being substituted in the system, with one moving onto a nearby Ti^{4+} site and $CaTiO_3$ being produced on the surface. The effect of the addition of the impurities is shown in figures **4.8** and **4.9**.

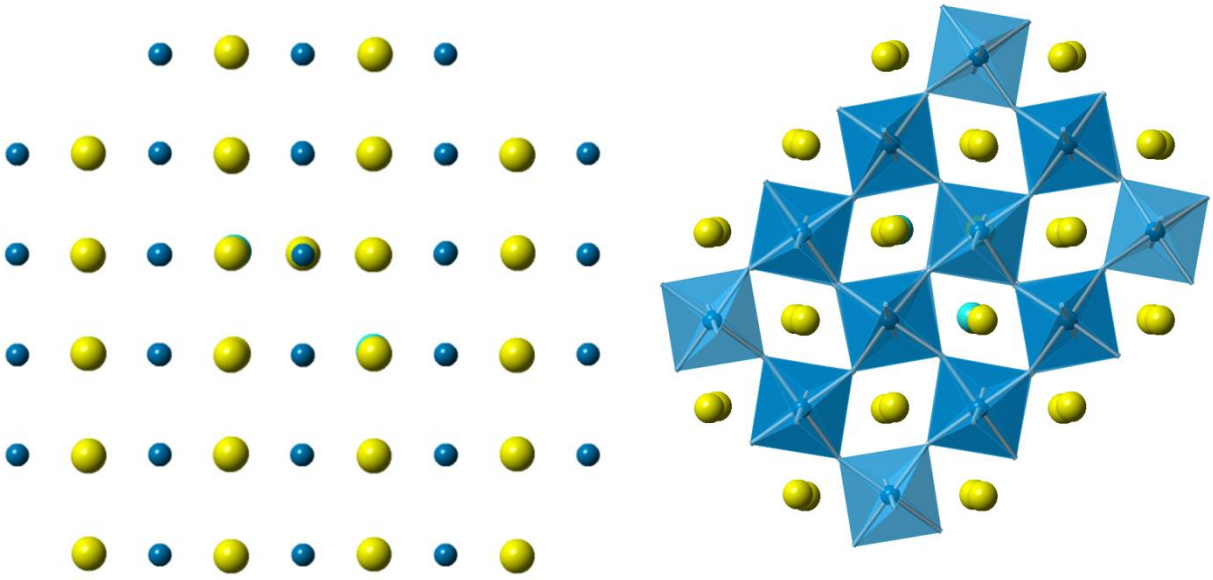

Fig. 4.8 (left) and Fig. 4.9 (right): Two ytterbium impurities on calcium sites with a calcium on titanium impurity. There is not significant distortion of the lattice in this system, with slightly exaggerated octahedral tilting around the defect centre.

Table 4.23: Solution energy results for scheme 7, both in a cluster and at infinite dilution.

Solution Energies – Scheme 7 (eV)					
Element	**Inf. Dil. E.**	**Cluster. E.**	**Binding E.**	**Inf. Sol. E**	**Clus. Sol. E.**
La	26.60	25.76	-0.84	1.33	0.91
Nd	23.12	22.37	-0.76	1.16	0.78
Gd	20.02	19.12	-0.90	1.11	0.66
Y	17.40	16.45	-0.95	1.12	0.64
Yb	15.48	14.65	-0.84	1.20	0.78

The trend in the results for this scheme (table **4.23**) follows a correlation with the ionic radius of the lanthanide, with the La-Y solution energies decreasing as the radius decreases. Surprisingly, ytterbium incorporation has a significantly higher solution energy than expected and does not follow the trend, possibly a consequence of being too small for the site. Overall the solution energies are quite low, on a par with scheme 4, and slightly lower for the larger elements. The range of energies is small with only 0.14 eV between the four lowest energies, with the lowest overall solution energy being 0.64 eV for yttrium and the highest being 0.91 eV for lanthanum.

- Scheme 8: Substitution of M^{3+} at Ti^{4+} with Ti^{4+} at Ca^{2+} compensation:

$$M_2O_3 + 2Ca_{Ca} + Ti_{Ti} \rightarrow 2M'_{Ti} + Ti^{\bullet\bullet}_{Ca} + CaTiO_3$$

$$E_s = \frac{1}{2}[2M'_{Ti} + Ti^{\bullet\bullet}_{Ca} + CaTiO_3 - M_2O_3]$$

(Equations 4.29 – 4.30)

This scheme (equations **4.29** and **4.30**) is similar to scheme 7, but the initial substitution occurs at the Ti^{4+} site and the ions are shuttled in the reverse direction – with a Ti^{4+} moving to the Ca^{2+} site. The movement of a titanium cation from the

centre of an octahedron may be unfavourable, but the replacement of the ion with a Ca^{2+} may stabilise the structure and make this interaction more favourable than a Ti^{4+} vacancy for example. Figures **4.10** and **4.11** show the locations of the impurities and their effect on the surrounding octahedra.

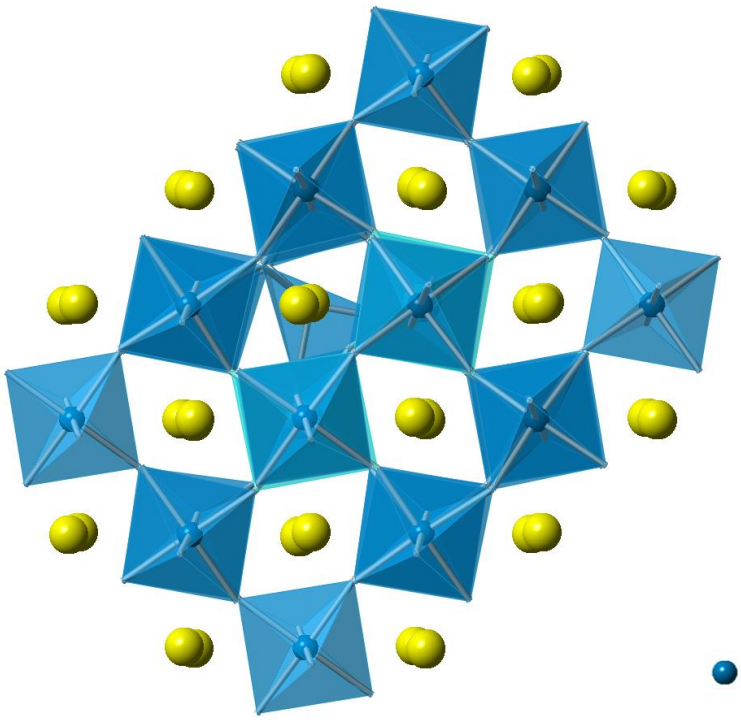

Fig. 4.10 (left): Two ytterbium impurities on titanium sites with a titanium on calcium impurity. There is some distortion of the titanium octahedra.

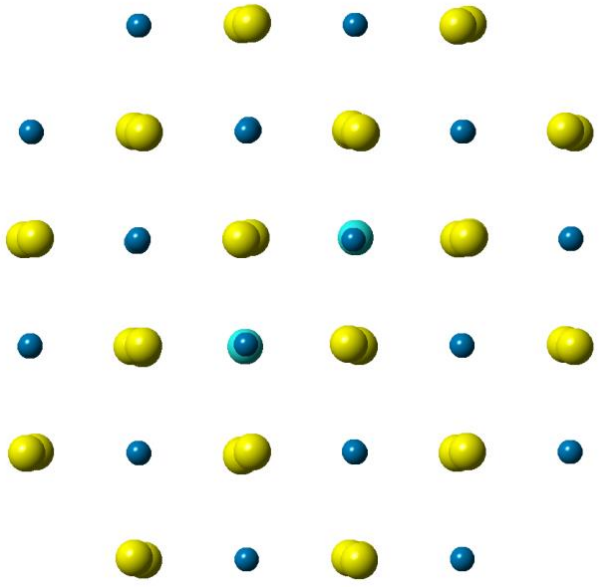

Fig. 4.11 (right): Down (010) it can be seen that the cations are not displaced majorly from their initial positions, though additional movement of the Ca^{2+} cations away from their initial positions is noticeable.

Table 4.24: Solution energy results for scheme 8, both in a cluster and at infinite dilution.

Solution Energies – Scheme 8 (eV)					
Element	**Inf. Dil. E.**	**Cluster. E.**	**Binding E.**	**Inf. Sol. E**	**Clus. Sol. E.**
La	30.70	29.98	-0.73	3.38	3.02
Nd	26.43	25.80	-0.63	2.81	2.50
Gd	22.56	22.01	-0.56	2.38	2.10
Y	19.36	18.85	-0.52	2.10	1.84
Yb	16.90	16.41	-0.49	1.91	1.67

Despite the similarities of scheme 8 to scheme 7, this scheme has considerably larger solution energy values (table **4.24**), and a much more linear correlation between ionic radius and solution energy. The lowest energy impurity is ytterbium – 1.67 eV – and the highest is lanthanum with a 3.02 eV solution energy.

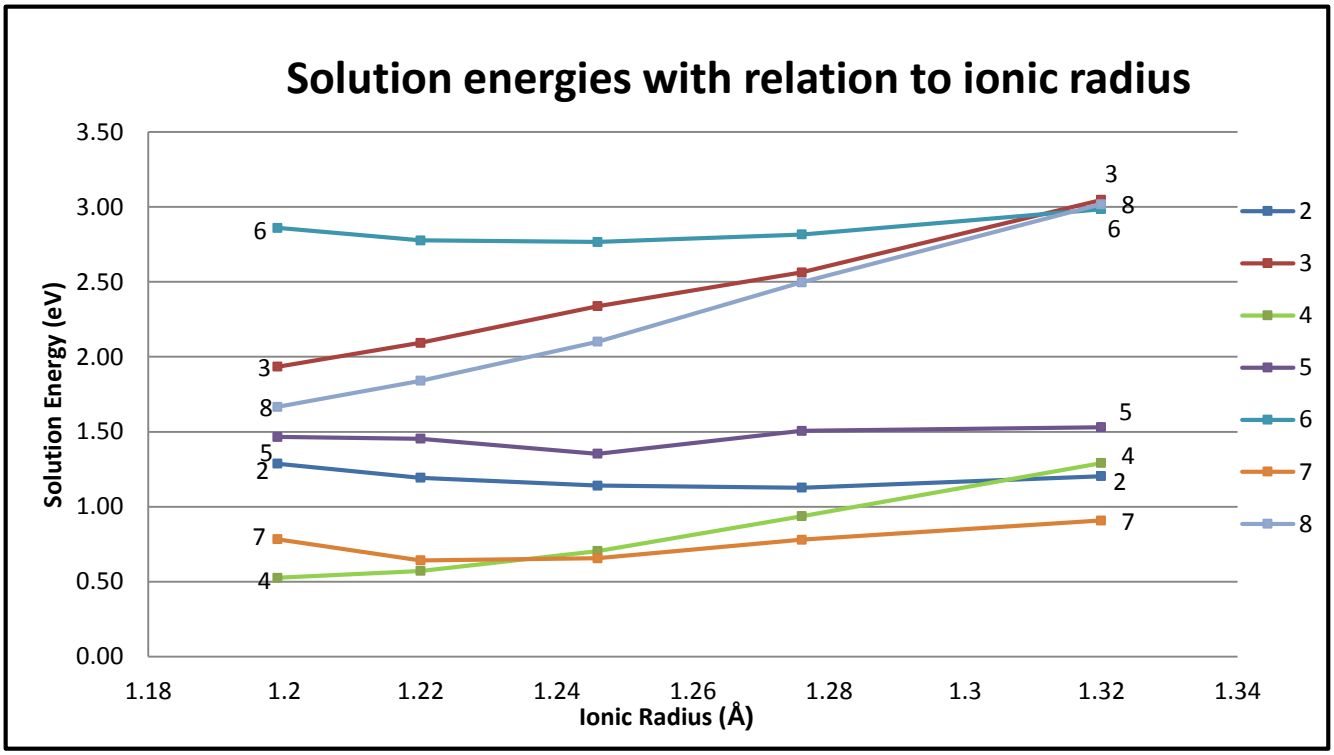

Graph 4.5: Solution energies as a function of ionic radius for schemes 2-8

Overall, when comparing schemes 2-8 as a function of dopant ionic radius, it becomes clear that scheme 4 is the most favourable charge compensation mechanism at low radius and scheme 7 is the most favourable at high radius. Scheme 6 is the highest energy across most of the range, with scheme 3 becoming the least favourable mechanism for lanthanum but only by a small margin. The overall energy range is ~2.5 eV, which is two orders of magnitude higher than K_BT at 298 K (~0.025 eV). This means that that the lowest energy schemes for each element are such considerably lower energies than the others that at room temperature that they will always be the preferential charge compensation mechanism.

The impact of these results on 90-Sr immobilisation in $CaTiO_3$ is that due to the favourability of self-compensation for yttrium incorporation, 100 % of the calcium sites can be substituted with 90-Sr due to the mechanism of charge compensation not requiring vacancies on Ca sites. If the favoured mechanism involved A site vacancies then there would be a risk of incorporated waste on the A site being removed from the bulk as the waste decayed.

Scheme 1 is considerably higher energy than the other schemes, and therefore can be completely discounted as a possibility.

Zirconium incorporation into $CaTiO_3$ brings in more challenges due to the increased positive charge and decreased ionic radius. As the end product of the 90-Sr decay chain it will eventually dominate the structure, but will initially only be present in low concentrations, with Sr and Y being the major impurities present.

4.6.3: 4+ Charged Impurities and Charge Compensation

For Zr^{4+} incorporation, six possible charge compensation mechanisms were studied. One was a straight substitution on the Ti^{4+} site and five were substitutions onto the Ca^{2+} site. It can be assumed that the Ti- Zr substitution will be the most favourable due to both size and charge similarities, but in the context of ^{90}Sr immobilisation substitution on the Ca^{2+} site also needs to be examined. ^{90}Zr is the end product of the ^{90}Sr decay chain and as a result will have a major effect on the crystal structure due to the continued increase of Zr^{4+} impurities in the material as more strontium ions decay through yttrium. Scheme 5, where the Ti^{4+} undergoes a reduction process, is similar in form to the 3+ incorporation scheme 1. As this mechanism was discounted it has not been studied further for zirconium incorporation.

- Scheme Zr-1: Substitution of Zr^{4+} at Ca^{2+} with O^{2-} interstitial compensation:

$$ZrO_2 + Ca_{Ca} \rightarrow Zr_{Ca}^{\bullet\bullet} + O_i'' + CaO$$

$$E_s = Zr_{Ca}^{\bullet\bullet} + O_i'' + CaO - ZrO_2$$

(Equations 4.31 – 4.32)

Scheme Zr-1 has the same issues as the 3+ charge scheme 6 – interstitial oxygen defects in $CaTiO_3$ are particularly unfavourable, and so it is likely that charge compensation through this route will also be energetically unfavourable.

- Scheme Zr-2: Substitution of Zr^{4+} at Ca^{2+} with Ca^{2+} vacancy compensation:

$$ZrO_2 + 2Ca_{Ca} \rightarrow Zr_{Ca}^{\bullet\bullet} + V_{Ca}'' + 2CaO$$

$$E_s = Zr_{Ca}^{\bullet\bullet} + V_{Ca}'' + 2CaO - ZrO_2$$

(Equations 4.33 – 4.34)

- Scheme Zr-3: Substitution of Zr^{4+} at Ca^{2+} with Ti^{4+} vacancy compensation:

$$2ZrO_2 + Ca_{Ca} + Ti_{Ti} \rightarrow 2Zr_{Ca}^{\bullet\bullet} + V_{Ti}'''' + CaO + CaTiO_3$$

$$E_s = \frac{1}{2}[2Zr_{Ca}^{\bullet\bullet} + V_{Ti}'''' + CaO + CaTiO_3 - 2ZrO_2]$$

(Equations 4.35 – 4.36)

- Scheme Zr-4: Substitution of Zr^{4+} at Ti^{4+}:

$$ZrO_2 + Ti_{Ti} \rightarrow Zr_{Ti} + TiO_2$$

$$E_s = Zr_{Ti} + TiO_2 - ZrO_2$$

(Equations 4.37 – 4.38)

Scheme Zr-4 is a direct Ti-Zr exchange, and due to their similar sizes and charges this should be the most favourable compared to the other mechanisms.

- Scheme Zr-5: Substitution of Zr^{4+} at Ca^{2+} with Ti^{3+} at Ti^{4+} compensation:

$$ZrO_2 + Ca_{Ca} + Ti_{Ti} \rightarrow Zr_{Ca}^{\bullet\bullet} + Ti_{Ti^{4+}}^{3+} + \frac{1}{2}O_2 + 2e' + CaO$$

$$E_s = \frac{1}{2}\left[Zr_{Ca}^{\bullet\bullet} + Ti_{Ti^{4+}}^{3+} + 2e' - \left(\frac{1}{2}D_{O_2} + EA_{O^{2-}}\right) + CaO - ZrO_2\right]$$

(Equations 4.39 – 4.40)

Scheme Zr-5, like the 3+ scheme 1, involves several additional factors due to a reduction occurring. Due to the very large values obtained for 3+ scheme 1, this mechanism was not studied for zirconium.

- Scheme Zr-6: Substitution of Zr^{4+} at Ca^{2+} with Ca^{2+} at Ti^{4+} compensation:

$$ZrO_2 + Ca_{Ca} + Ti_{Ti} \rightarrow Zr_{Ca}^{\bullet\bullet} + Ca_{Ti}'' + TiO_2$$

$$E_s = Zr_{Ca}^{\bullet\bullet} + Ca_{Ti}'' + TiO_2 - ZrO_2$$

(Equations 4.41 – 4.42)

The results of the investigation into these mechanisms has been summarised in graph **4.6** and table **4.25**, excluding scheme Zr-5. Figures **4.12** and **4.13** illustrate an example of how zirconium incorporation affects the octahedra in the lattice, showing how this happens in scheme Zr-6.

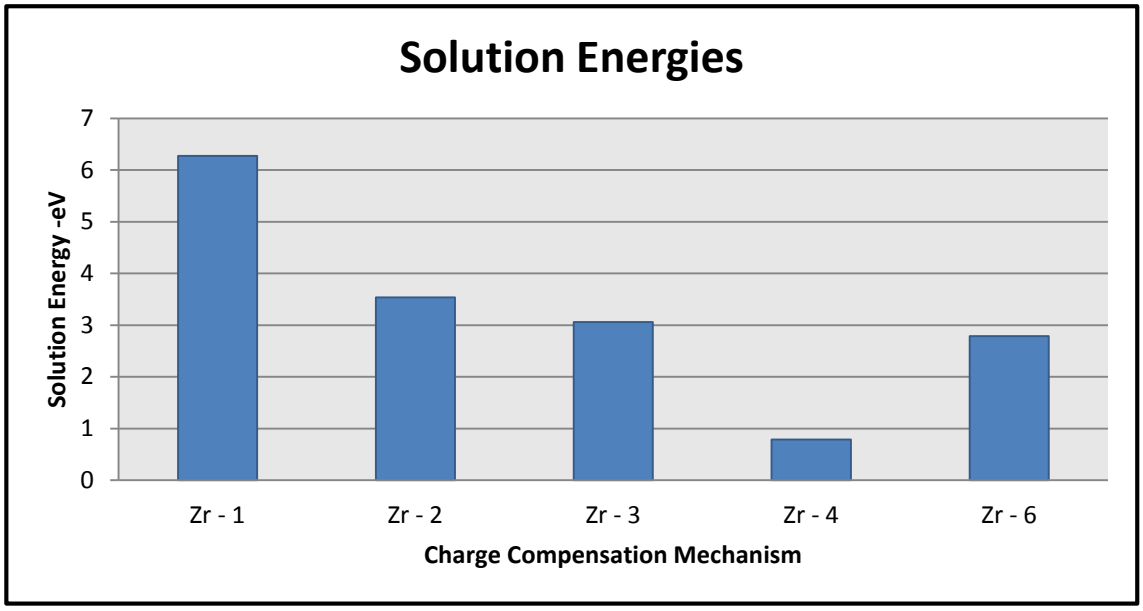

Graph 4.6: Solution energies as a function of ionic radius for schemes 1-4 and 6

Table 4.25: Solution energy results for zirconium incorporation, both in a cluster and at infinite dilution.

Solution Energies – Zirconium (eV)					
Scheme	**Inf. Dil. E.**	**Cluster. E.**	**Binding E.**	**Inf. Sol. E**	**Clus. Sol. E.**
Zr-1	-67.41			6.27	
Zr-2	-32.01	-32.43	-0.43	3.97	3.54
Zr-3	-26.08	-28.06	-1.99	4.05	3.06
Zr-4	1.90	1.90	0.0000	0.79	0.79
Zr-6	4.74	3.89	-0.85	3.63	2.79

The first noticeable conclusion for each zirconium incorporation mechanism is the unfavourability compared to the 3+ incorporation mechanisms apart from 3+ scheme 1. Scheme Zr-4 is by far the most favourable, with a solution energy of 0.79 eV, in line with the favourability of 3+ incorporation. This is due to the similar size and charge of Zr^{4+} and Ti^{4+}. On the titanium site there is no need for charge compensation and substitution here is particularly facile. For incorporation onto the calcium site, the most favourable mechanism is Zr-6 (2.79 eV) where a Ca^{2+} ion is moved onto a Ti^{4+} site to compensate, similar to 3+ charge scheme 7, which was also particularly favourable (0.64 – 0.91 eV). The least favourable mechanism is Zr-1 (6.27 eV), where

incorporation of an oxygen interstitial involves particularly high energies and a cluster was unable to form. As scheme Zr-6 is the most favourable, it means the maximum level of incorporation of dopant into the material can be 100 %. As larger concentrations of dopant are added into the structure, the A and B site cations will change position but no vacancies will be produced and there is less chance of impurity species being removed from the material unless some incorporates onto the Ti^{4+} site.

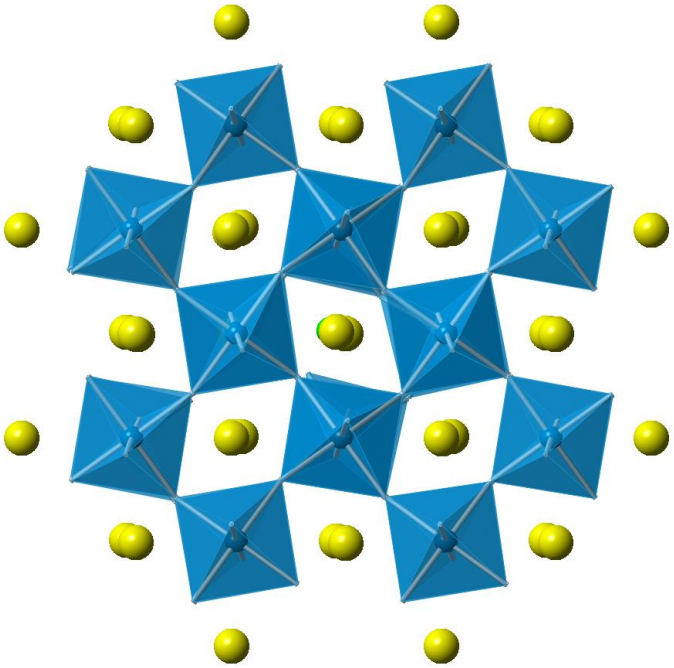

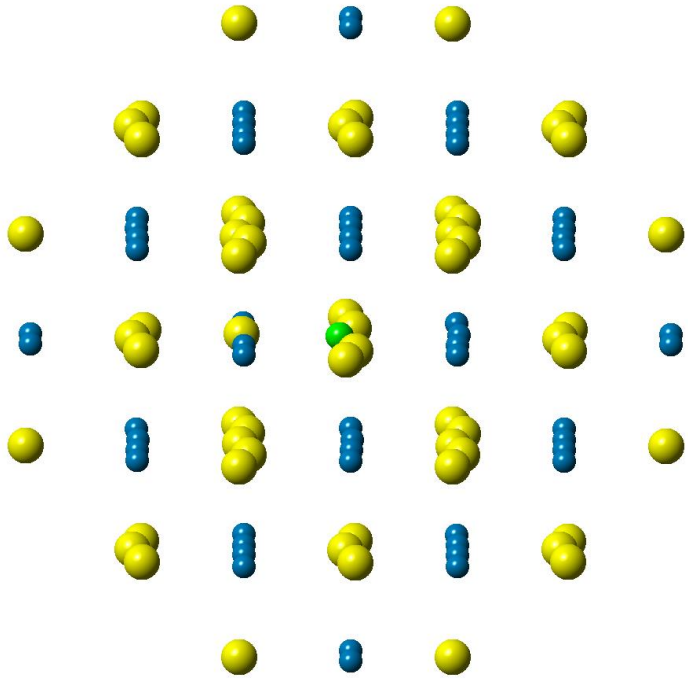

Fig. 4.12 (left) and Fig. 4.13 (right): Scheme Zr-6, showing incorporation of a Zr^{4+} ion on the Ca^{2+} site and an Ca^{2+} ion on the Ti^{4+} site as the most favourable charge compensation mechanism. If all dopant cations are incorporated onto the A site initially, then 100 % dopant incorporation can be achieved without adverse effects. This is promising for the material's intended use in radioactive waste immobilisation.

4.7: Monte Carlo Simulations of $Ca_{1-x}Sr_xTiO_3$ Supercells

For the $CaTiO_3$-$SrTiO_3$ solid solution, there is evidence of Sr ion clustering at low concentrations and less distinct clusters as strontium concentration increases, with more Ca-Sr-Ca ordering throughout the structure.[60] Using simulated annealing and a Monte Carlo algorithm to examine the lowest energy configuration of a $Ca_{1-x}Sr_xTiO_3$ supercell, this behaviour can be computationally examined and the point at which the clustering behaviour changes can be determined. Graphs **4.7** and **4.8** show this simulated annealing process in a 3x3x3 supercell of $Ca_{0.875}Sr_{0.125}TiO_3$ with 540 atoms, showing the change in supercell energy at each iteration of the annealing run. Each iteration corresponds to a change in energy of the system and a subsequent change in jump probability. A radial distribution function of the different structures can also be used to show the change in dopant-dopant distance as concentration increases.

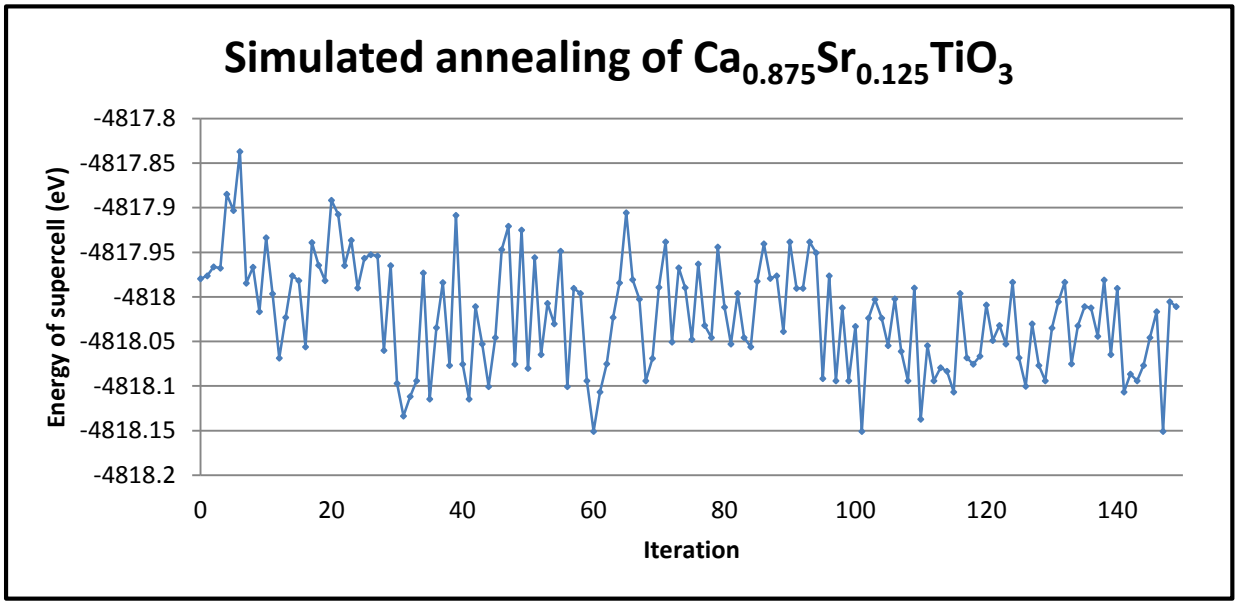

Graph 4.7: Simulated annealing run of $Ca_{0.875}Sr_{0.125}TiO_3$

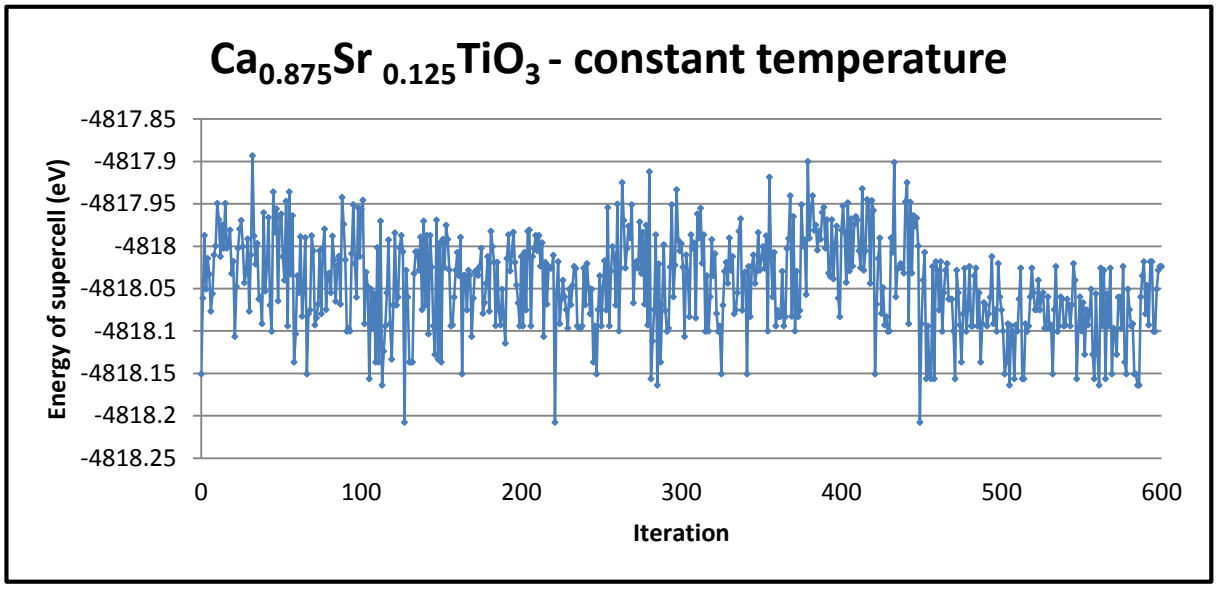

Graph 4.8: Constant temperature run of $Ca_{0.875}Sr_{0.125}TiO_3$

Initially, the MC run goes from 1000 K to 100 K and finds the lowest energy supercell (graph **4.7**), then using this supercell as a restart point a second run is done at a constant 300 K. This keeps the potential energy of the system the same and searches the potential energy well for a global minimum (graph **4.8**). iteration 147 was used as the lowest energy structure from the annealing, and point 449 was determined to be the global minimum energy. This global minimum is shown in figures **4.14** and **4.15**.

In addition to $Ca_{0.875}Sr_{0.125}TiO_3$, $Ca_{0.75}Sr_{0.25}TiO_3$ and $Ca_{0.625}Sr_{0.375}TiO_3$ were also studied, with the lowest energy configuration of the former shown in figures **4.16** and **4.17** and the latter in figures **4.18** and **4.19**.

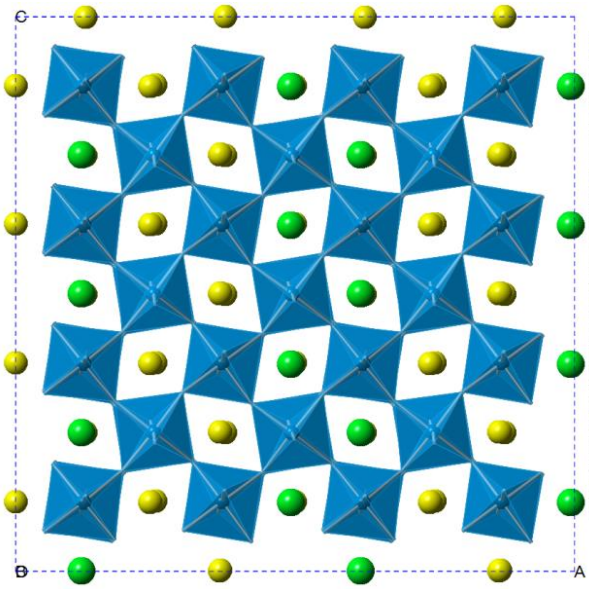

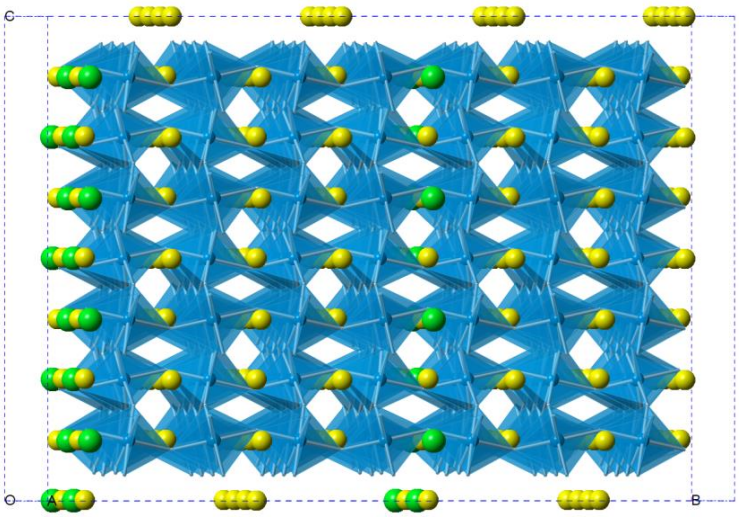

Fig. 4.14 (above left) and Fig. 4.15 (above right): Lowest energy configuration of $Ca_{0.875}Sr_{0.125}TiO_3$. Clustering of the Sr impurities (green) can be seen.

Fig. 4.16 (below left) and Fig. 4.17 (below right): Lowest energy configuration of $Ca_{0.75}Sr_{0.25}TiO_3$. Clustering of the Sr impurities (green) can be seen.

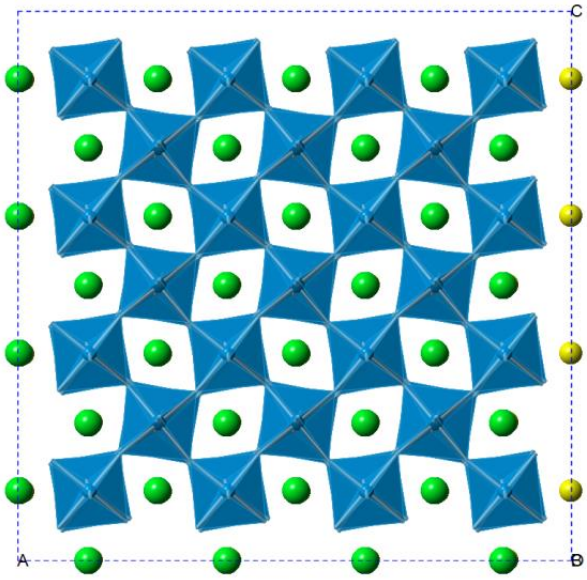

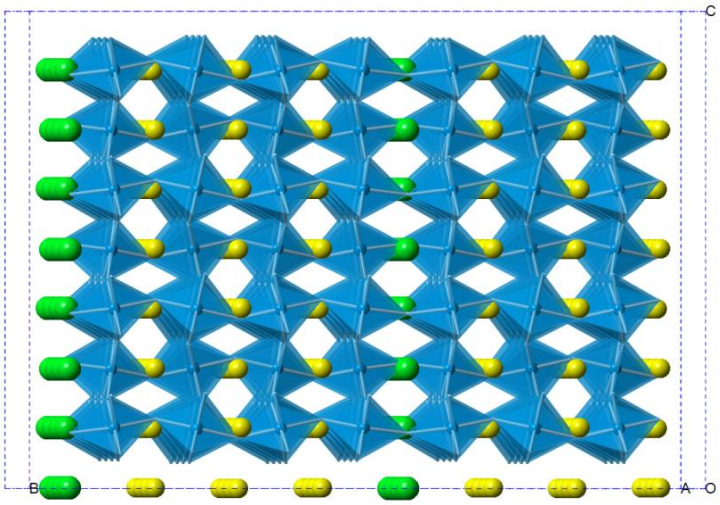

For both $Ca_{0.875}Sr_{0.125}TiO_3$ and $Ca_{0.75}Sr_{0.25}TiO_3$ clustering of the strontium impurities can be seen. The most favourable configuration of the ions is in a plane and suggests that the attractive interactions between the impurities are strong at low concentrations.

Fig. 4.18 (right): Lowest energy configuration of $Ca_{0.625}Sr_{0.375}TiO_3$. Note that Sr impurities are more spread apart and a rocksalt ordering of Ca and Sr cations is beginning to form.

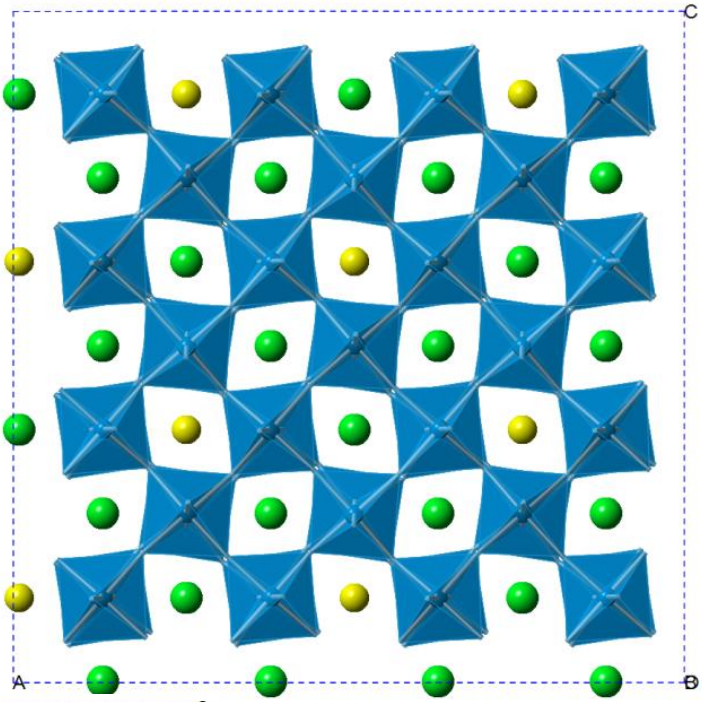

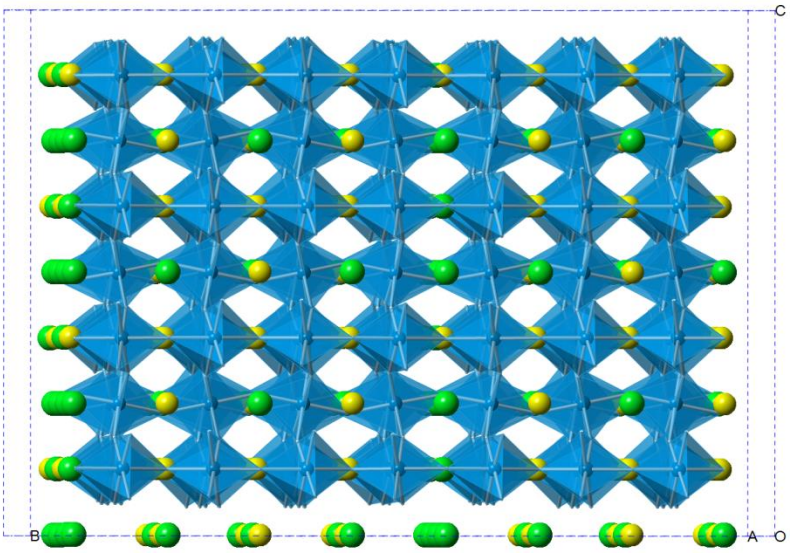

Fig. 4.19 (left): Rocksalt ordering is beginning to occur in the crystal structure of $Ca_{0.625}Sr_{0.375}TiO_3$.

In $Ca_{0.625}Sr_{0.375}TiO_3$ clustering is less apparent and the strontium and calcium cations are beginning to order in a NaCl-like rocksalt structure where the Sr ions are separated by Ca ions in particular layers, instead of coming together in a cluster. In a waste immobilisation context this is more ideal than forming clusters as the spread of impurity will spread the damaging effects of the waste material throughout the structure and not localise it in one place.

4.8: RDF of $Ca_{1-x}Sr_xTiO_3$ Supercells

To confirm the results of the MC investigation, an RDF (radial distribution function) study was undertaken on the lowest energy structures. From each strontium ion in the structure, a function determines the distance to its nearest strontium neighbours. As the function extends outwards the locations of each ion in relation to the initial strontium and the concentration of ions at that distance are calculated.

For $Ca_{0.875}Sr_{0.125}TiO_3$ (Graph **4.9**) there is a considerably larger strontium concentration close to the origin than further away, suggesting the ions are grouping together. For $Ca_{0.75}Sr_{0.25}TiO_3$ (Graph **4.10**) there is less of a concentration difference between close ion sites and further away sites, suggesting there is a lower affinity for clustering and the defects are starting to spread more.

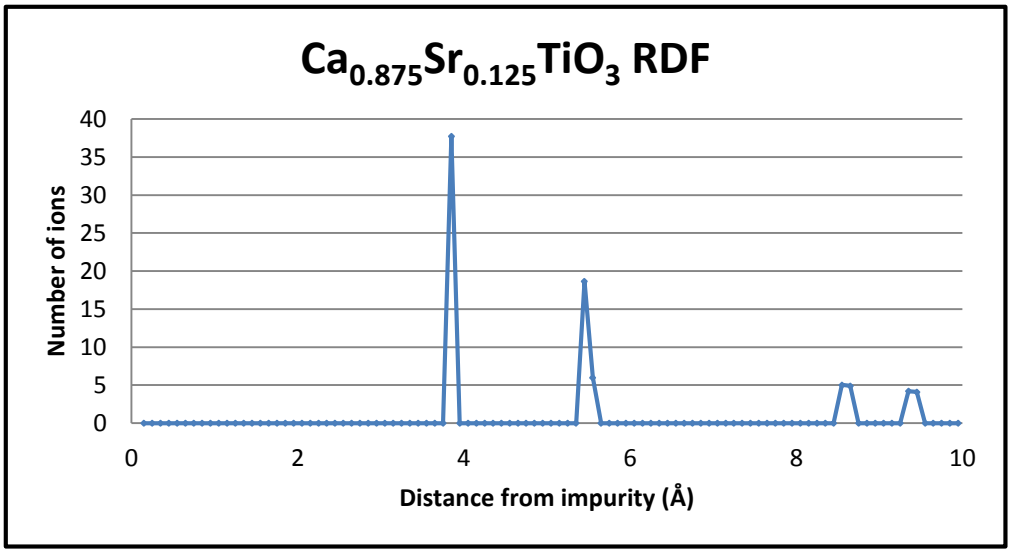

Graph 4.9: RDF plot of $Ca_{0.875}Sr_{0.125}TiO_3$

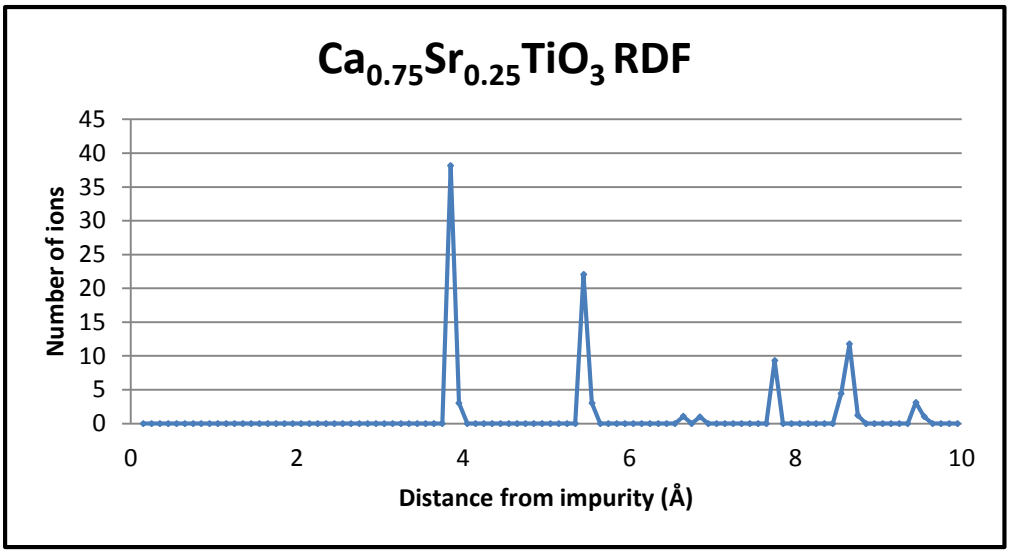

Graph 4.10: RDF plot of $Ca_{0.75}Sr_{0.25}TiO_3$

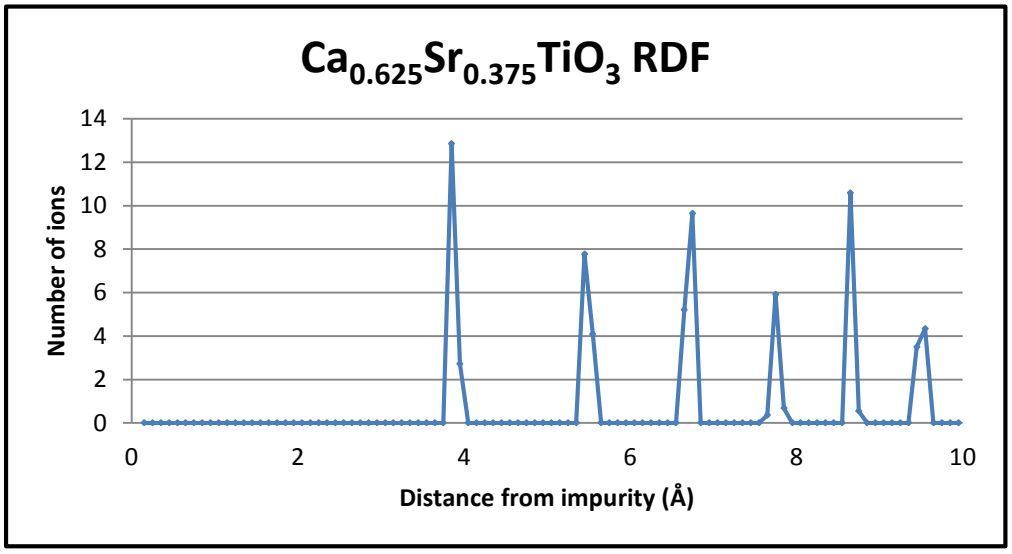

Graph 4.11: RDF plot of $Ca_{0.625}Sr_{0.375}TiO_3$

$Ca_{0.75}Sr_{0.25}TiO_3$ (graph 4.11) shows a much more even distribution of ion concentrations across each lattice site. This is indicative of a lack of clustering and the formation of a more rocksalt-like structure.

4.9: Conclusions

The overall aim of the theoretical investigation was to examine how defects in $CaTiO_3$ manifest themselves, and the implications of this for radioactive waste immobilisation. It has been shown that self-compensation and Ca^{2+} ion site relocation are the most favourable charge compensation mechanisms for 3+ charged impurities, and Ca^{2+} ion site relocation for Zr^{4+} impurities, second to straight Zr^{4+} - Ti^{4+} substitution. Strontium impurities have been seen to cluster together at low concentrations and spread apart in a rocksalt-like fashion in larger concentrations, and the implications of this for waste immobilisation have been discussed. $CaTiO_3$ can successfully incorporate large dopant concentrations of 90-Sr and the mechanism by which this can occur has been examined. Further research can be undertaken probing further into the ordering of Sr impurities and examining the ordering of Y impurities. Larger cell sizes and the influence of temperature and time also need to be investigated. Beyond this, the interaction of the $CaTiO_3$ phase with the other phases in SYNROC is still to be investigated in great detail.

“Perhaps I'm old and tired, but I think that the chances of finding out what's actually going on are so absurdly remote that the only thing to do is to say, "Hang the sense of it," and keep yourself busy”

— Slartibartfast, The Hitchhiker's Guide to the Galaxy

Chapter 5: Results and Analysis – Experimental

Both $CaTiO_3$ and $SrTiO_3$ were synthesised in addition to intermediate phases – $Ca_{1-x}Sr_xTiO_3$, where x= 0.3, 0.5 and 0.7. These compositions were chosen in order to give a broad perspective of the structures across the entire $Ca_{1-x}Sr_xTiO_3$ solid solution. Two different synthetic routes were tested in order to determine which was more ideal for creating a pure product. Table **5.1** describes the expected symmetries and space groups for the five compositions studied, with the phase diagram in fig. **5.1**.

Table 5.1 – Expected structures of the 5 investigated titanates at 298 K taken from the phase diagram (fig. **5.1**)

Structures		
Formula	**Expected symmetry**	**Expected space group**
$CaTiO_3$	Orthorhombic	Pnma
$Ca_{0.7}Sr_{0.3}TiO_3$	Orthorhombic	Pnma
$Ca_{0.5}Sr_{0.5}TiO_3$	Orthorhombic	Pnma
$Ca_{0.3}Sr_{0.7}TiO_3$	Orthorhombic / Tetragonal	Pnma / I4/mcm
$SrTiO_3$	Cubic	Pm-3m

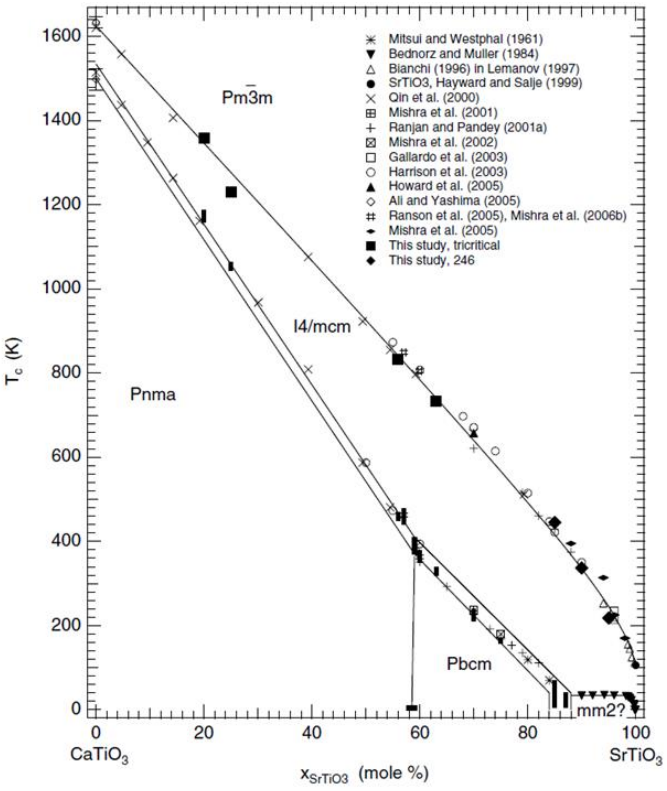

Fig. 5.1: Phase diagram of the $CaTiO_3$ – $SrTiO_3$ solid solution showing the expected structures for each composition of $Ca_{1-x}Sr_xTiO_3$ at a range of temperatures.

From: M. A. Carpenter *et al., J. Phys.: Condens. Mater.*, 2006, **18,** 10725–10749

5.1: Synthesis

5.1.1: Aqueous Route

Five samples of $Ca_{1-x}Sr_xTiO_3$ were produced via aqueous synthesis from stoichiometric solutions of aqueous $Sr(NO_3)_2$, $Ti(OCH(CH_3)_2)_4$, 70% HNO_3 and a slurry of $CaCO_3$.

Initially the aqueous $Sr(NO_3)_2$ and $Ti(OCH(CH_3)_2)_4$ were combined to form a white precipitate. The titanium isopropoxide hydrolyses in air and was added to the solution by weight rather than volume to minimise errors. Another possible synthesis method would have been using an inert atmosphere such as in a Schlenk line to create the solution in, eliminating the hydrolysis issue. Following this a $CaCO_3$ slurry was produced by adding water and this was combined with concentrated HNO_3 to form aqueous calcium nitrate. This solution was then combined with the $Sr(NO_3)_2$/ $Ti(OCH(CH_3)_2)_4$ mixture forming a white sludge. The sludge was then stir dried until completely solid.

The combined solid was then calcined in air at 600°C for one hour to remove the organics such as isopropoxide. A white powder was produced, which was then pelleted and fired in a furnace under air at 1300 °C for 12 hours. The resultant pellets were then reground with a pestle and mortar, repelleted and resintered. This process was then repeated four times until the reaction was determined to be complete via powder XRD analysis.

C. J. Ball *et al*. (1998) synthesised $Ca_{1-x}Sr_xTiO_3$ using a similar method, though their route employed higher temperatures and longer sintering times than the route

employed here.[33] The literature route was not employed due to the high temperatures and large sintering times required.

Table 5.2: Quantities of starting material for aqueous route synthesis

Starting Material Quantities				
Structure	**$Sr(NO_3)_2$ quantity / g**	**$Ti(OCH(CH_3)_2)_4$ quantity / g**	**$CaCO_3$ quantity / g**	**HNO_3 quantity / cm^3**
$CaTiO_3$	0.0000	4.0140	1.4720	1.9630
$Ca_{0.7}Sr_{0.3}TiO_3$	0.8450	3.4877	0.9330	1.2790
$Ca_{0.5}Sr_{0.5}TiO_3$	1.3250	3.2736	0.6240	0.8890
$Ca_{0.3}Sr_{0.7}TiO_3$	1.7510	3.0960	0.3550	0.4870
$SrTiO_3$	2.3070	2.8550	0.0000	0.0000

5.1.2: Solid State Route

After the initial investigation using the aqueous route, a solid state route was employed as a comparison and with a view to gaining purer samples. With fewer starting materials and variables than the aqueous route, the errors in the synthesis is less of an issue and solid powders are generally easier to work with than solutions involving concentrated acids. This route involved both less harmful reagents and fewer steps, though there was the possibility of a less than homogeneous mixture of starting materials hindering the purity of the product.

Stoichiometric ratios of $Sr(NO_3)_2$, TiO_2 and CaO powders were ground together with a mortar and pestle to create a fine powder. Any water present in the powder was removed using a drying oven, and then the powder was stored in a desiccator prior to use. The aim was for 2 g of product, which would be a significant enough quantity for analysis. This powder was then pelleted and fired in air at 1300°C for 12 hours.

Pellets were then regrinded, repelleted and refired before being analysed via powder XRD.

Table 5.3: Quantities of starting material for solid state route synthesis

Starting Material Quantities			
Structure	**$Sr(NO_3)_2$ quantity / g**	**TiO_2 quantity / g**	**CaO quantity / g**
$CaTiO_3$	0.0000	1.1750	0.8250
$Ca_{0.7}Sr_{0.3}TiO_3$	0.8454	1.0634	0.5227
$Ca_{0.5}Sr_{0.5}TiO_3$	1.3251	1.0000	0.3571
$Ca_{0.3}Sr_{0.7}TiO_3$	1.7509	0.9439	0.1988
$SrTiO_3$	2.3068	0.8705	0.0000

5.2: Analysis

5.2.1: $CaTiO_3$

The initial synthesis with the aqueous route produced poorer results, with a low signal-to-noise ratio and broad, asymmetric peaks of low relative intensity in the PXRD pattern (Fig. **5.2**). Though the peaks were roughly at the correct 2-theta for $CaTiO_3$, the peaks were broad and there was considerable overlap of peaks. This suggests the lattice was not as ordered and crystalline as expected. This could be due to inconsistent particle size where the powder was not ground thoroughly enough, or could be due to impurities such as TiO_2 or CaO where the impurity peaks could overlap with those of the product – causing an effect of broadening or splitting.

For solid state route synthesis much sharper, well-defined peaks with high relative intensities and higher signal-to-noise ratio were present in the XRD pattern (Fig. **5.3**)

showing greatly improved crystallinity. As a result it was concluded that the solid state route was more ideal for making pure $CaTiO_3$.

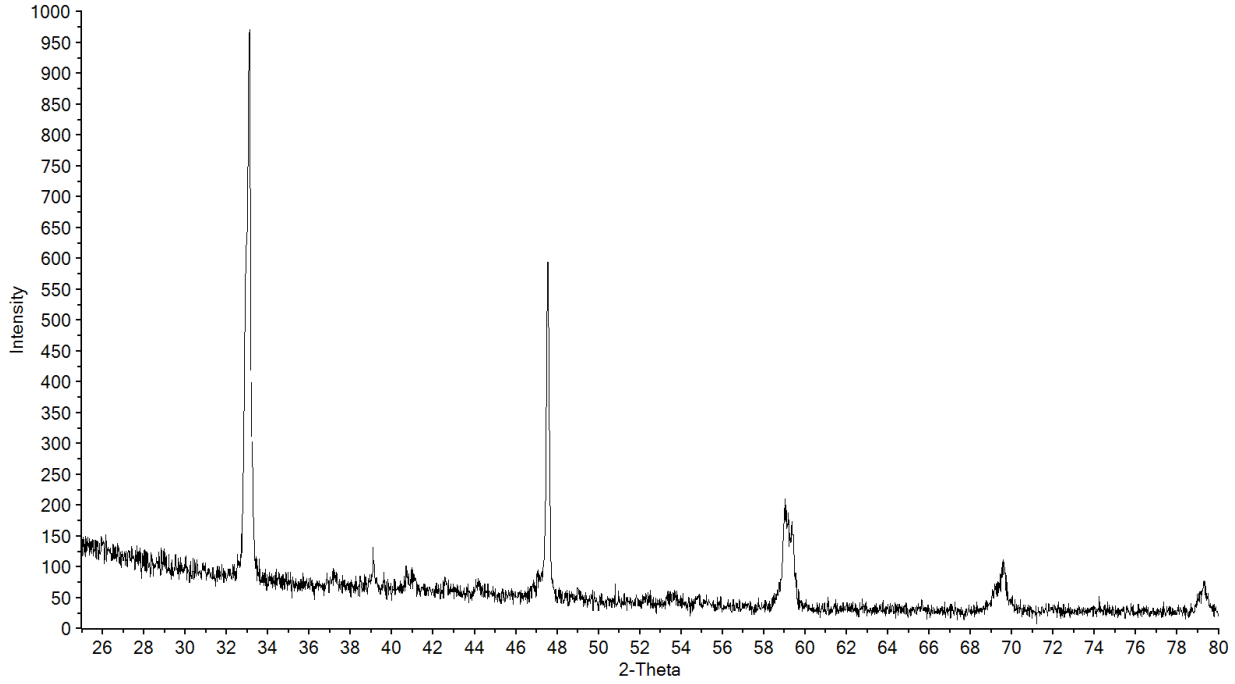

Fig. 5.2: $CaTiO_3$ powder XRD pattern from aqueous route synthesis

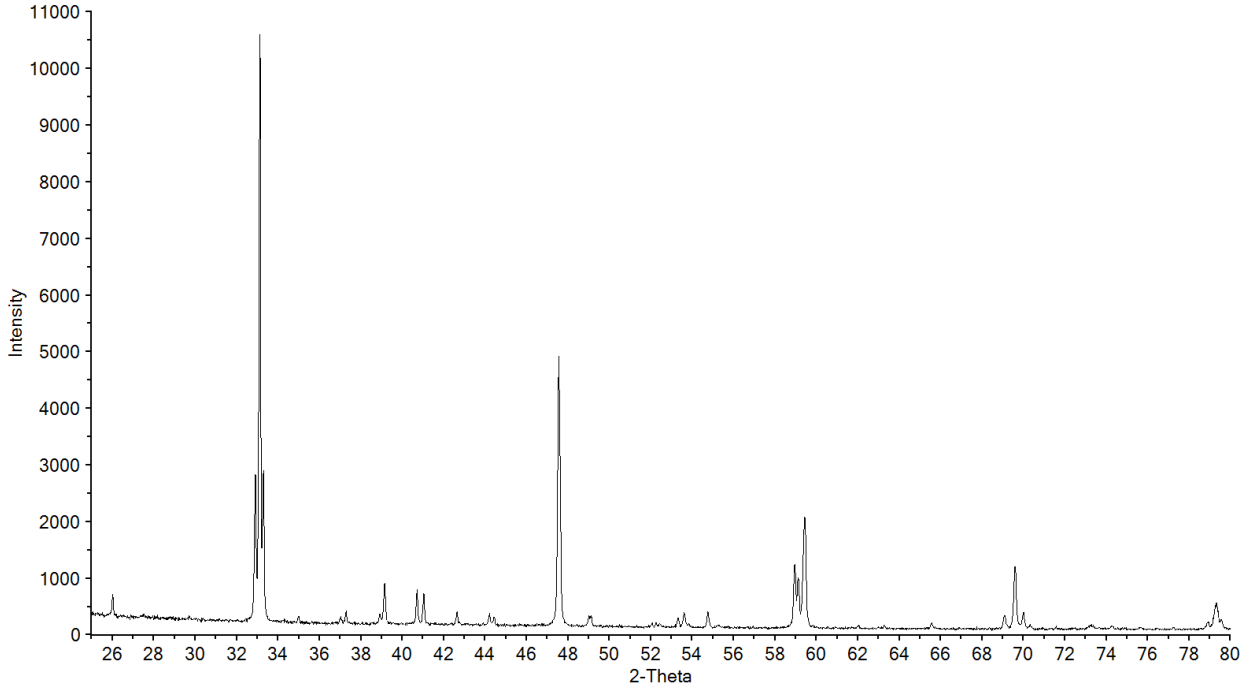

Fig. 5.3: $CaTiO_3$ powder XRD pattern from solid state route synthesis

5.2.2: $SrTiO_3$

For the aqueous route $SrTiO_3$ PXRD pattern (Fig. **5.4**) there was an improved signal to noise ratio and the pattern was not as ill-defined as $CaTiO_3$. There are some sharp symmetrical peaks present and a low background, but there were also several impurity peaks and considerable asymmetry in others. It was thought that this may have been due to partial hydration of the titanium isopropoxide, leading to a lower than calculated titanium content. To combat this, the experiment was rerun with excess Ti-isopropoxide, the results of which are shown in Fig. **5.5**.

For the Ti-excess product there were a couple of small impurity peaks at a 2-theta of ~27° but the pattern suggests a relatively successful synthesis in comparison with the previous attempt. Increased titanium in the system meant that more product could be generated with fewer impurities. For the solid state route (Fig. **5.6**) the peaks had similar peak profiles to the aqueous route patterns, but the impurity peaks at ~27° were not present and there was a better signal-to-noise ratio. Peaks also had higher relative intensities and were sharper. The highest quality data was obtained from the solid state synthetic route, which the PXRD pattern showed having higher quality powder than the aqueous route. The solid state route was also quicker and involved both less steps and reagents than the aqueous route. Five firings were needed for the aqueous route compared with two for the solid state route, and there was no preliminary synthesis needed to form the starting calcium and strontium solutions.

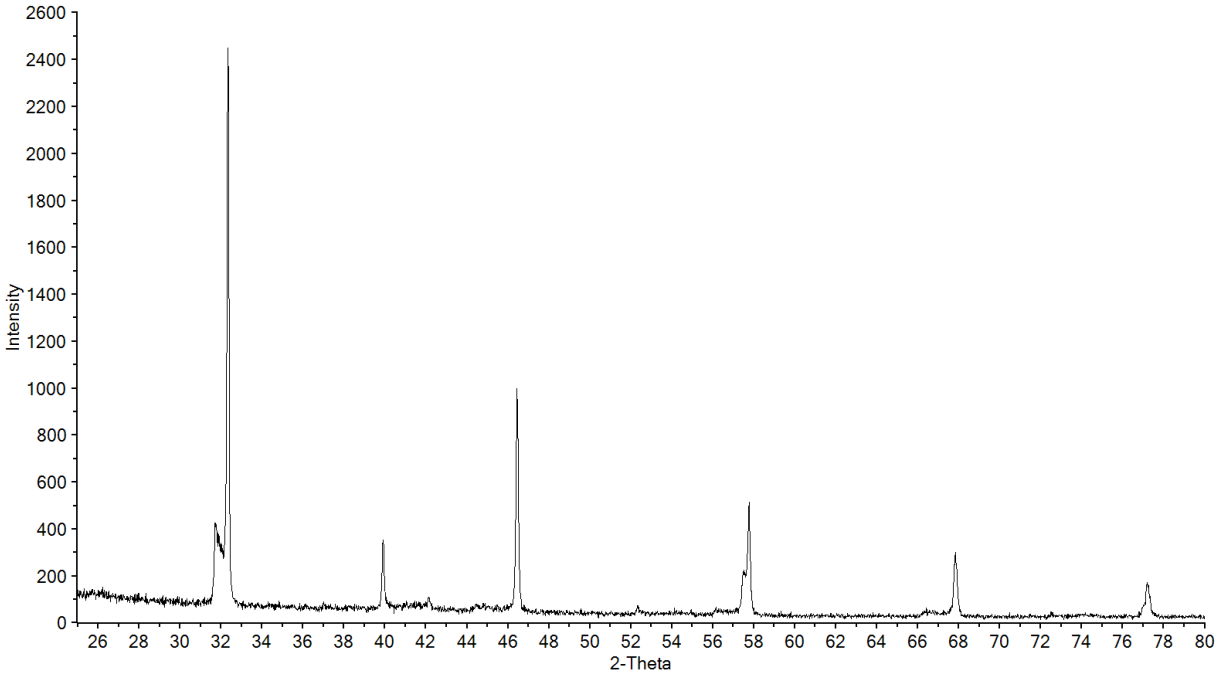

Fig. 5.4: $SrTiO_3$ powder XRD pattern from aqueous route synthesis

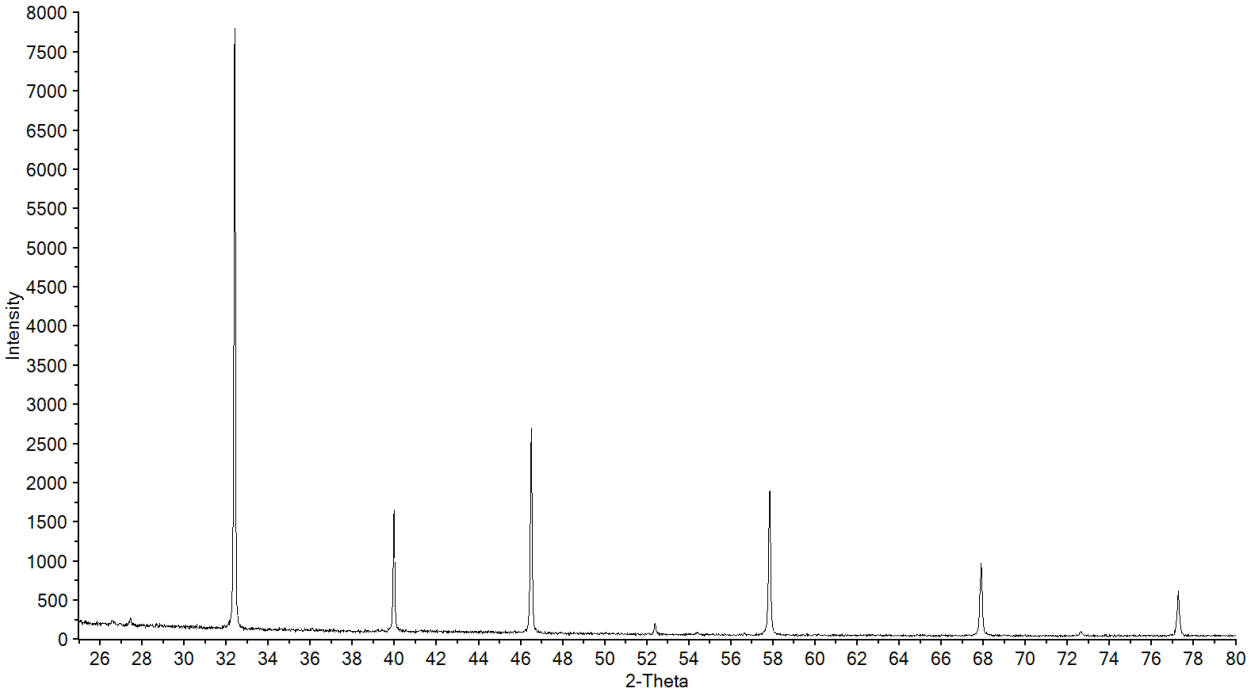

Fig. 5.5: $SrTiO_3$ powder XRD pattern from aqueous route synthesis with excess Ti-isopropoxide

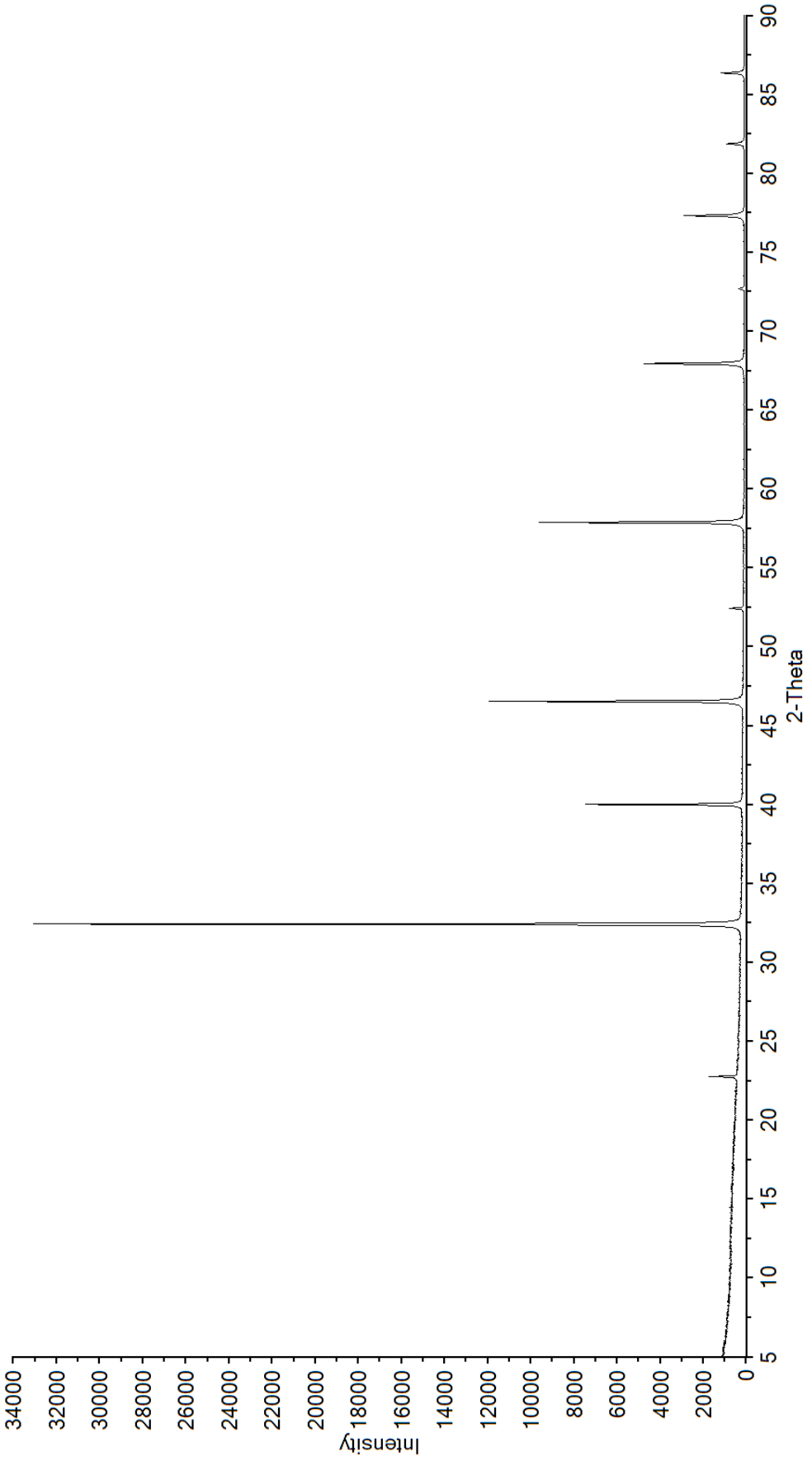

Fig. 5.6: $SrTiO_3$ powder XRD pattern from solid state route synthesis

5.2.3: Ca-$SrTiO_3$ Intermediates

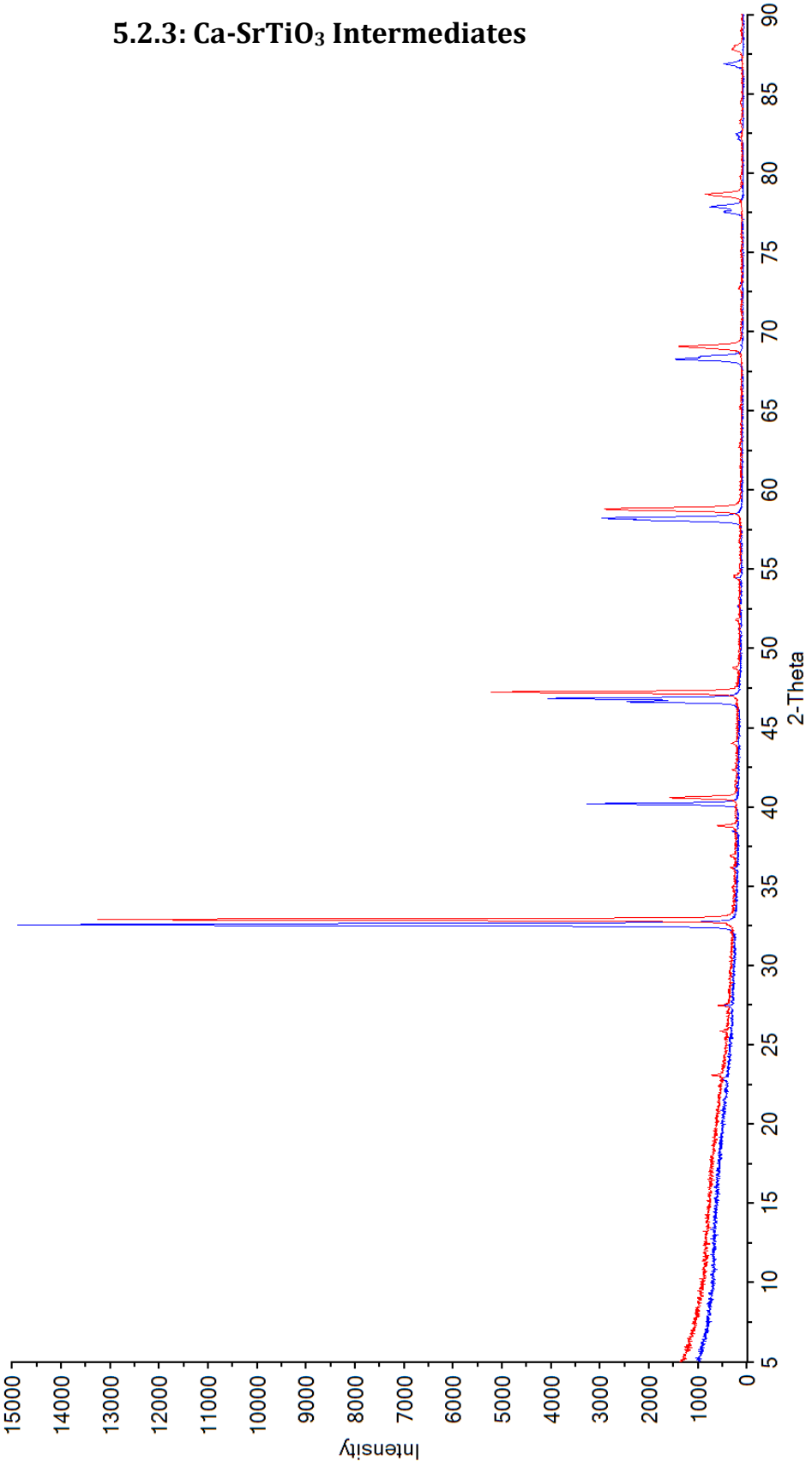

Fig. 5.7: PXRD patterns of $Ca_{0.3}Sr_{0.7}TiO_3$ (blue) and $Ca_{0.7}Sr_{0.3}TiO_3$ (red) from solid state route synthesis

The intermediary phases in the solid solution were all prepared via the solid state route, with the intention of observing the changes in lattice parameters of the unit cell with increased strontium dopant concentration. As shown in Fig. **5.7**, with increased Sr concentration the peaks are shifted towards the left, showing an expansion in the unit cell. This can be rationalised by the larger Sr^{2+} cation having greater effect as dopant levels increase. The peaks have similar intensities, though there is some peak splitting in $Ca_{0.3}Sr_{0.7}TiO_3$. This peak splitting is not present in $Ca_{0.5}Sr_{0.5}TiO_3$ (Fig. **5.8**) which is characterised by sharp, narrow peaks of high relative intensity. This splitting is indicative of a symmetry change in the system as it moves between orthorhombic and distorted orthorhombic towards tetragonal, increasing in symmetry.

Once the five studied phases of $Ca_{1-x}Sr_xTiO_3$ were synthesised with good purity and crystallinity, the resultant PXRD patterns were refined via the Rietveld method in order to determine lattice parameters and atomic positions. The intention of this was to generate the data needed to create a computational model of the system, which requires these and the symmetry.

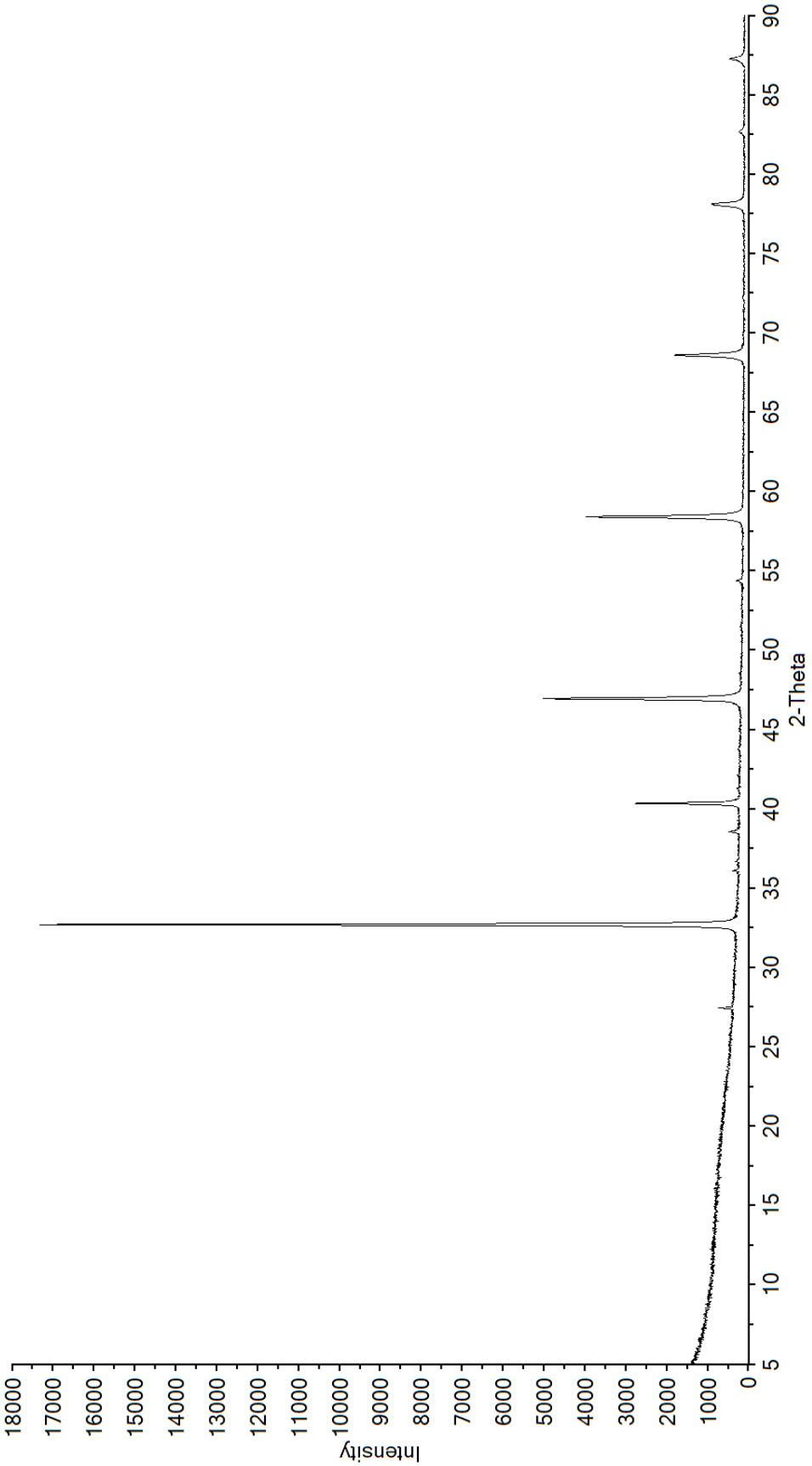

Fig. 5.8: PXRD pattern of $Ca_{0.5}Sr_{0.5}TiO_3$ from solid state route synthesis

5.3: Refinement

Rietveld refinement was utilised to analyse the recorded PXRD patterns and gain very accurate information about the systems studied. The five phases in the solid solution were matched against experimental XRD data and refined using the GSAS EXPGUI program.[51] The refined parameters were the background, zero-point, peak shapes, site occupancies and atomic positions. Within GSAS these can be individually refined to reach a sensible χ^2 value and fit to the experimental data. From this, refined lattice parameters were obtained, as well as refined atomic positions. These refined lattice parameters are detailed below, along with the χ^2 value of each fit. The patterns gained from the fit are shown in the appendix and in fig. **5.9** – $CaTiO_3$.

Table 5.4: Refined lattice parameters, site occupancyes and final χ^2 values for the 5 studied compositions.

Structures						
Formula	**a (Å)**	**b (Å)**	**c (Å)**	**Volume* (Å³)**	**A site**	**χ^2 Value**
$CaTiO_3$	5.368(1)	5.429(1)	7.624(1)	55.547	Ca_1	1.464
$Ca_{0.7}Sr_{0.3}TiO_3$	5.428(2)	5.444(2)	7.682(2)	56.753	$Ca_{0.7}Sr_{0.3}$	1.706
$Ca_{0.5}Sr_{0.5}TiO_3$	5.470(4)	7.724(4)	5.466(4)	57.740	$Ca_{0.5}Sr_{0.5}$	2.421
$Ca_{0.3}Sr_{0.7}TiO_3$	5.476(1)	5.480(1)	7.780(1)	58.360	$Ca_{0.3}Sr_{0.7}$	1.758
$SrTiO_3$	3.898(1)	3.898(1)	3.898(1)	59.228	Sr_1	2.864

*Normalised per formula unit

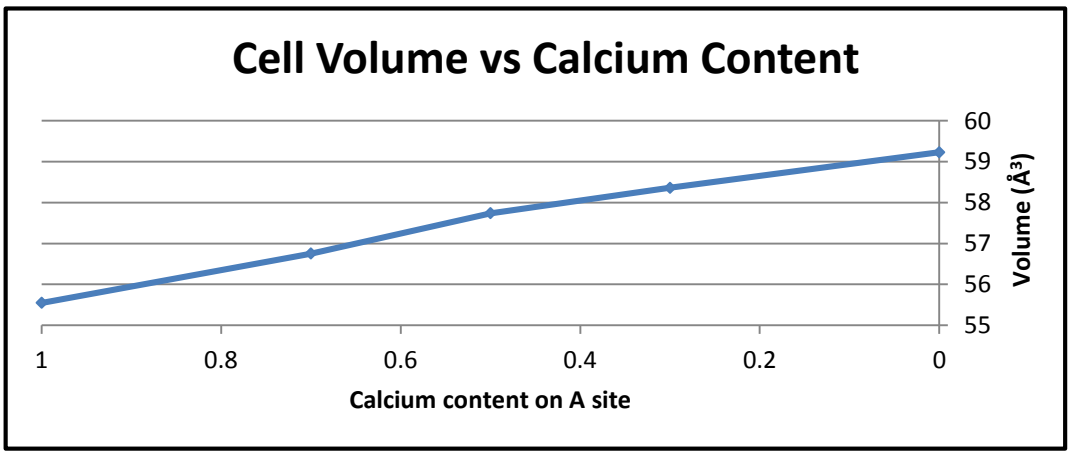

Graph 5.1: Volume of each composition against calcium content

During the Rietveld refinement, low χ^2 values were achieved for each of the structures, showing good agreement between the observed pattern and the calculated parameters. From this set of results, it is clear that as the Sr dopant level increases (down table **5.4**) the lattice parameters also increase in length. The volume per formula unit also increases as calcium content decreases, as shown in graph **5.1**. This can be rationalised as due to the presence of the larger Sr^{2+} cation in place of Ca^{2+}. This observation agrees with the trend of shifting peak position to a lower 2-theta as the Sr^{2+} dopant level increases. Also noticeable is the shift from clear orthorhombicity in $CaTiO_3$ to an almost tetragonal structure in $Ca_{0.3}Sr_{0.7}TiO_3$, which agrees with the expected symmetry from table **5.1**. In conclusion, both the synthesis of the solid solutions and the refinements were successful as they replicated experimental data and expected trends.

One of the main aims of the synthesis of these materials and subsequent refinement was to gain new accurate atomic positions for the atoms in the $CaTiO_3$ structure.

Table 5.5: Refined atomic positions for $CaTiO_3$.

Fractional Coordinates of Atoms in $CaTiO_3$			
Atom	**X coord**	**Y coord**	**Z coord**
Ca	-0.0068(10)	0.0362(10)	0.2500
Ti	0.0000(10)	0.0000(10)	0.0000
O1	0.0810(20)	0.4834(10)	0.2500
O2	0.7097(20)	0.2883(10)	0.0340

The atomic positions detailed in table **5.5**, along with the lattice parameters from table **5.4**, can now be used to create an input file for atomistic calculations without the need to rely on published experimental data or calculated DFT structures.

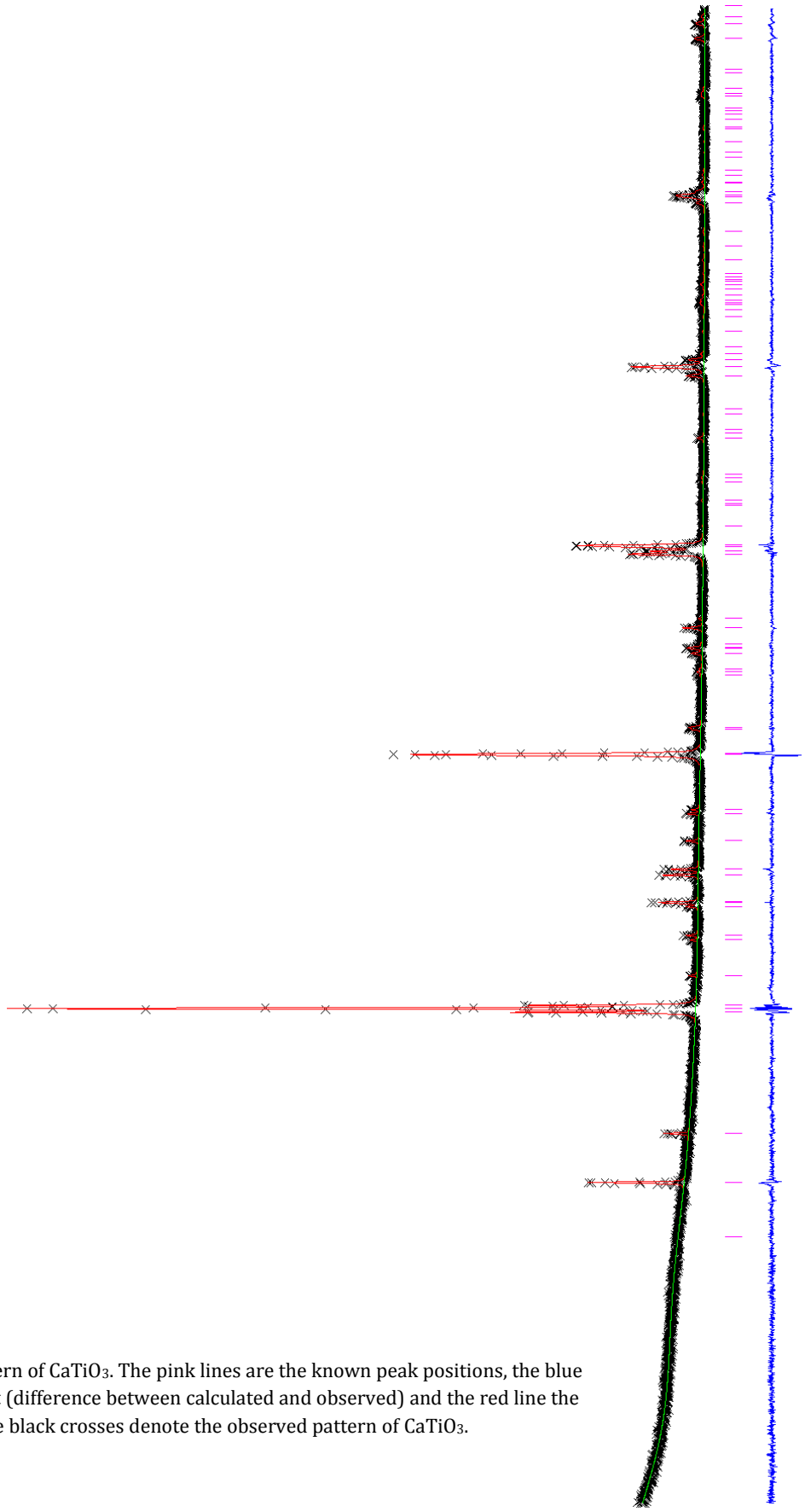

Fig. 5.9: Rietveld pattern of $CaTiO_3$. The pink lines are the known peak positions, the blue line the goodness of fit (difference between calculated and observed) and the red line the calculated pattern. The black crosses denote the observed pattern of $CaTiO_3$.

5.4: Conclusions

The overall result of the experimental section of this investigation is that the solid state synthesis method is the preferred method for producing pure products for different structures in the $Ca_{1-x}Sr_xTiO_3$ solid solution. Five compositions were synthesised and good quality PXRD patterns were taken of the range of structures, which showed the high levels of ordering and crystallinity expected. The structure of these were then refined to good levels of agreement and the atomic positions of the different sites in the space group were elucidated. The aqueous synthetic route did not achieve such high quality products as the solid state route, with more impurities present – most likely a result of partial hydration of the Ti-isopropoxide. The route also took longer and required more starting reagents.

The expansion of the lattice on increased strontium content was shown, and the change in symmetry of the structure from orthorhombic to tetragonal and then cubic was seen as the lattice parameters became closer in length and then equal. This phase change also did not occur until there were significant levels of Sr^{2+} doping. This result is promising in the context of waste incorporation – large amounts of waste 90-Sr could be introduced into the lattice before possibly detrimental phase changes could occur. This underlines the usability of $CaTiO_3$ in this context, and is evidence of the ability of the material to store waste within SYNROC.

Chapter 6: Conclusions and Further Research

The main aim of this project was to investigate, both experientially and theoretically, calcium titanate ($CaTiO_3$) in order to gain insight into the defect and doping properties of the material. This was a constituent of an overarching aim to determine the favourability of the mineral for radioactive waste incorporation. Approaching the problem from both an experimental and a theoretical perspective had a secondary aim of studying how different techniques could be used to investigate both calcium titanate and other perovskite compounds.

Initially, a Buckingham potential set for calcium titanate was tested to determine the usability of the model, followed by a short discussion of how to improve the fit of the model to the static dielectric constant of $CaTiO_3$. It was found that the potential model was adequate for modelling $CaTiO_3$, CaO and three TiO_2 polymorphs. Of the TiO_2 polymorphs anatase was determined to have the lowest lattice energy. The potential set was then expanded for several alkaline earth elements and rare earth elements.

Intrinsic Schottky and Frenkel defects were studied in $CaTiO_3$, and a CaO Schottky defect was determined to be the lowest in energy. Frenkel defects were seen to be particularly unfavourable, in line with other perovskite oxides. Substitutional defects were then studied in greater detail, with 2+, 3+ and 4+ charged defects being incorporated into the $CaTiO_3$ structure and the solution energies of different charge compensation mechanisms measured. For the 3+ charged defects, where yttrium and a range of lanthanides were studied, the most favourable charge compensation mechanism for larger ions was found to be scheme 7 – Substitution of M^{3+} at Ca^{2+} with Ca^{2+} at Ti^{4+} compensation. For smaller ions scheme 4 – Substitution of M^{3+} at Ca^{2+} and at Ti^{4+} with self-compensation

– was found to be the most favourable. It was found that 4+ charged impurities preferred substitution onto the Ti^{4+} site due to charge compensation not being needed, with the most favourable Ca^{2+} site compensation mechanism was scheme Zr-6, where the charge is balanced by a Ca^{2+} ion moving to a Ti^{4+} site.

To study defect incorporation at greater concentrations, a series of simulated annealing calculations using a Monte Carlo algorithm were performed on a $CaTiO_3$ supercell with a percentage of strontium impurities. It was seen that at low (<37.5 %) concentrations a clustering of strontium defects was the most favourable defect site configuration, whereas at larger concentrations it was more favourable for the impurities to be spread out. This conclusion was backed up with RDF analyses of the crystals showing spreading of the strontium sites with increasing concentration.

In the context of waste immobilisation, these results are beneficial as they indicate the material is able to support waste strontium throughout the lattice, and the radioactive decay products of ^{90}Sr – ^{90}Y and ^{90}Zr - can also be accommodated within the structure at high levels of substitution.

Experimentally, it was shown after testing two different synthetic routes that the solid state synthetic route was the most ideal route for the synthesis of the end products and intermediates of the $Ca_{1-x}Sr_xTiO_3$ series. It was seen that the different structures in the solid solution could be synthesised in significant quantities and in few steps. In both sections of the investigation the issue of phase change was not seen to be a significant factor in the ability of the structure to incorporate waste, with the tilting of octahedra around defect sites not completely disrupting the lattice.

Overall, calcium titanate is an ideal material for waste strontium immobilisation, with numerous advantages over borosilicate glass. Within SYNROC, alongside hollandite and zirconolite, it is a viable alternative to borosilicate glass as the next generation of waste immobilisation material, though there is still scope for further research in the area. The other SYNROC phases have not been extensively studied computationally, and neither have their interactions with each other and their surface chemistry. Additionally, the effect of radiation damage on these materials needs to be studied. This study looked at the end products of ^{90}Sr decay, and more insight is needed on the effect of the beta decay mechanism on the local environment, which could have significant detrimental effects on the viability of the material. Furthermore, this defect incorporation study focused for the main part on pure calcium titanate, and more work needs to be done on how the relative favourability of the different charge compensation mechanisms alters with increased dopant concentration.

"A learning experience is one of those things that says, "You know that thing you just did? Don't do that.""

– *Douglas Adams, The Salmon of Doubt*

References

1. W. E. Lee, M. Gilbert, S. T. Murphy and R. W. Grimes, *J. Am. Ceram. Soc.*, 2013, **96**, 2005-2030.

2. A. Connelly, R. Hand, P. Bingham and N. Hyatt, *J. Nucl. Mater.,* 2011, **408**, 188-193.

3. R. C. Ewing and W. Lutze, *Ceram. Inter.*, 1991, **17**, 287-293.

4. R. Ewing, W. Lutze and W. J. Weber, *J. Mater. Res.*, 1995, **10**, 243-246.

5. Y. Ni, J. M. Hughes and A. N. Mariano, *Am. Mineral.*, 1995, **80**, 21-26.

6. G. R. Lumpkin, *J. Nucl. Mater.*, 2001, **289**, 136-166.

7. K. Smith, G. Lumpkin, M. Blackford, R. Day and K. Hart, *J. Nucl. Mater.*, 1992, **190**, 287-294.

8. A. Ringwood, S. Kesson, N. Ware, W. Hibberson and A. Major, *Nature.*, 1979, **278**, 219-223.

9. A. Ringwood, *Mineral. Mag.*, 1985, **49**, 159-176.

10. E. Vance, C. Ball, R. Day, K. Smith, M. Blackford, B. Begg and P. Angel, . *Alloy. Compd.*, 1994, **213**, 406-409.

11. B. Begg, E. Vance, B. Hunter and J. Hanna, *J. Materi. Res.*, 1998, **13**, 3181-3190.

12. M. Carter, *Mater. Res. Bull.*, 2004, **39**, 1075-1081.

13. V. Aubin-Chevaldonneta, D. Cauranta, A. Dannouxa, D. Gouriera, T. Charpentier, L. Mazerolles and T. Advocat, *J. Nucl. Mater.*, 2007, **366**, 137-160.

14. J. Amoroso, J. Marra, S. D. Conradson, M. Tang and K. Brinkman, *J. Alloy. Compd.*, 2014, **584**, 590-599.

15. M. T. Buscaglia, V. Buscaglia, M. Viviani and P. Nanni, *J. Am. Ceram. Soc.*, 2001, **84**, 376-384

16. R. T. Shannon, *Acta. Cryst. A.*, 1976, **32**, 751-767.

17. N. U. Navi, G. Kimmel, G. Yardeni, J. Zabicky, R. Z. Shneck, M. H. Mintz and A. Navrotsky, *J. Am. Ceram. Soc.*, 2013, **96**, 2644-2650.

18. M. Carpenter, C. Howard, K. Knight and Z. Zhang, *J. Phys.: Condens. Matter.*, 2006, **18**, 10725.

19. H. Miura, *Mineral. J.*, 1986, **13**, 119-129.

20. K. R. Whittle, N. C. Hyatt, K. L. Smith, I. Margiolaki, F. J. Berry, K. S. Knight and G. R. Lumpkin, *Am. Mineral.*, 2012, **97**, 291-298.

21. E. Kuo, M. Qin, G. Thorogood, K. Whittle, G. Lumpkin and S. Middleburgh, *J. Nucl. Mater.*, 2013, **441**, 380-389.

22. J. Cooper, D. R. Cousens, R. Lewis, S. Myhra, R. L. Segall, R. Smart, P. S. Turner and T. J. White, *J. Am. Ceram. Soc.*, 1985, **68**, 64-70.

23. N. U. Navi, G. Kimmel, J. Zabicky, S. V. Ushakov, R. Z. Shneck, M. H. Mintz and A. Navrotsky, *J. Am. Ceram. Soc.*, 2011, **94**, 3112-3116.

24. E. Browne and J. Tuli, *Nuclear Data Sheets.*, 2007, **108**, 2173-2318.

25. V. S. Puli, D. K. Pradhan, B. C. Riggs, D. B. Chrisey and R. S. Katiyar, *J. Alloy. Compd.*, 2014, **584**, 369-373.

26. J.-S. Park, Y.-H. Lee, K.-B. Kim and Y.-I. Kim, *Nucl. Instrum. Meth. B.,* 2012, **284**, 44-48.

27. C. Kuper, R. Pankrath and H. Hesse, *Applied Physics A*, 1997, **65**, 301-305.

28. O. Shrivastava, N. Kumar and I. Sharma, *Mater. Res. Bull.*, 2005, **40**, 731-741.

29. V. Marques, L. Cavalcante, J. Sczancoski, E. Paris, J. Teixeira, J. Varela, F. De Vicente, M. Joya, P. Pizani and M. Siu Li, *Spectrochim. Acta. A.*, 2009, **74**, 1050-1059.

30. K. Lemański, A. Gągor, M. Kurnatowska, R. Pązik and P. Dereń, *J. Solid. State. Chem.*, 2011, **184**, 2713-2718.

31. E. Browne, *Nuclear Data Sheets.*, 1997, **82**, 379-546.

32. A. Bohre and O. Shrivastava, *J. Nucl. Mater.*, 2013, **433**, 486-493.

33. C. Ball, B. Begg, D. Cookson, G. Thorogood and E. Vance, *J. Solid. State. Chem.*, 1998, **139**, 238-247.

34. O. Shrivastava and R. Srivastava, *Prog. Cryst. Growth. Ch.*, 2002, **45**, 103-106.

35. C. L. Freeman, J. A. Dawson, H.-R. Chen, J. H. Harding, L.-B. Ben and D. C. Sinclair, *J. Mater. Chem.*, 2011, **21**, 4861-4868.

36. J. Dawson, X. Li, C. Freeman, J. Harding and D. Sinclair, *J. Mater. Chem. C.*, 2013, **1**, 1574-1582.

37. M. J. Akhtar, Z.-U.-N. Akhtar, R. A. Jackson and C. R. A. Catlow, *J. Am. Ceram. Soc*, 1995, **78**, 421-428.

38. J. Szajman, R. S. C. Smart and S. Myhra, *Surf. Coat. Tech.,* 1987, **30**, 333-342.

39. R. Chourasia and O. Shrivastava, *Bull. Mater. Sci.*, 2011, **34**, 89-95.

40. M. Bassoli, M. Buscaglia, C. Bottino, V. Buscaglia, M. Molinari, F. Maglia, G. Parravicini and M. Dapiaggi, *J. Appl. Phys.*, 2008, **103**, 014104-014104-014110.

41. W. M. Haynes, *CRC Handbook of Chemistry and Physics*, CRC press, 2014.

42. X. Yang, Q. Li, R. Liu, B. Liu, S. Jiang, K. Yang, J. Liu, Z. Chen, B. Zou and T. Cui, *CrystEngComm.*, 2014, **16**, 4441-4446.

43. J. D. Gale, *Journal of the Chemical Society, Faraday Trans.*, 1997, **93**, 629-637.

44. J. D. Gale and A. L. Rohl, *Mol. Simulat.*, 2003, **29**, 291-341.

45. J. D. Gale, P. Raiteri and A. C. T. van Duin, *Phys. Chem. Chem. Phys.*, 2011, **13**, 16666-16679.

46. J. E. Jones, *Proc. Roy. Soc. Lond. A: Mat.*, 1924, 463-477.

47. G. C. Mather, M. S. Islam and F. M. Figueiredo, *Adv. Funct. Mater.*, 2007, **17**, 905-912.

48. B. Dick Jr and A. Overhauser, *Phys. Rev.*, 1958, **112**, 90.

49. N. Mott and M. Littleton, *Trans. Faraday. Soc.,* 1938, 34, 485-499.

50. H. Rietveld, *J. Appl. Crystallogr.*, 1969, **2**, 65-71.

51. B. H. Toby, *J. Appl. Crystallogr.*, 2001, **34**, 210-213.

52. S. Sasaki, C. T. Prewitt, J. D. Bass and W. Schulze, *Acta. Cryst. C.*, 1987, **43**, 1668-1674.

53. Y. D. Sinelnikov, G. Chen and R. C. Liebermann, *Phys. Chem. Miner.*, 1998, **25**, 515-521.

54. T. Fujii, A. Fujishima, T. Hirano and T. Kobayashi, *Appl. Phys. Lett.*, 1993, **62**, 3204-3206.

55. T. S. Bush, J. D. Gale, C. R. A. Catlow and P. D. Battle, *J. Mater. Chem.*, 1994, **4**, 831-837.

56. M. Cherry, M. S. Islam and C. R. A. Catlow, *J. Solid. State. Chem.*, 1995, **118**, 125-132.

57. D. M. Tobaldi, A. Tucci, A. S. Škapin and L. Esposito, *J. Eur. Ceram. Soc.*, 2010, **30**, 2481-2490.

58. P. Ballirano and R. Caminiti, *J. Appl. Crystallogr.*, 2001, **34**, 757-762.

59. I. Djerdj and A. Tonejc, *J. of Alloy. Compd.*, 2006, **413**, 159-174.

60. Q. Hui, M. T. Dove, M. G. Tucker, S. A. Redfern and D. A. Keen, *J. Phys.: Condens. Matter.*, 2007, **19**, 335214.

Bibliography

B.E. Burakov, M.I. Ojovan and W.E. Lee, *Crystalline Materials for Actinide Immobilisation*, Imperial College Press, London, 2011

M.I. Ojovan and W.E. Lee, *An Introduction to Nuclear Waste Immobilisation*, Elsevier, United Kingdom, 2005

C.R. Bayliss and K. F. Langley, *Nuclear Decommissioning, Waste Management and Environmental Site Remediation, Butterworth-Heinemann, 2003*

A. E. Ringwood, *Safe Disposal of High Level Nuclear Reactor Wastes: A New Strategy*, Australian National University Press, Canberra, 1978

Nuclear Decommissioning Authority, *The 2010 UK Radiactive Waste Inventory: Main Report*, NDA, 2011

D. J. Green, *An Introduction to the Mechanical Properties of Ceramics*, Cambridge University Press, Cambridge, 1998

L. E. Smart and E. A. Moore, *Solid State Chemistry: An Introduction,* CRC Press, Boca Raton, Fl, USA, 4th edn., 2012

A. R. West, *Solid State Chemistry and its Applications,* Wiley, 2nd edn., Stutent edn., 2014

D. R. Lide, *CRC Handbook of Chemistry and Physics*, CRC Press, Boca Raton, FL, USA, 86th edn., 2005.

W. M. Haynes, *CRC Handbook of Chemistry and Physics*, CRC Press, Boca Raton, FL, USA, 95th edn., 2014.

C. R. A. Catlow, *Computer Modelling in Inorganic Crystallography,* Academic Press, 1997

Appendix 1: Radioactive decay

Common fission products of U-235

Element	Mass Number	Fission Yield	Half Life (approx.)
Caesium	138	4.660e-03	33.4 minutes
Caesium	137	5.992e-04	30.2 years
Caesium	136	5.530e-05	13.16 days
Caesium	135	4.903e-06	2,300,000 years
Caesium	134	7.699e-08	2.065 years
Caesium	133	7.909e-09	Stable
Barium	144	3.970e-02	11.5 seconds
Barium	141	1.657e-02	12.75 days
Barium	138	4.110e-05	Stable
Barium	137	1.870e-06	Stable
Barium	136	4.723e-08	Stable
Barium	135	7.629e-10	Stable
Strontium	94	4.507e-02	75.3 seconds
Strontium	90	7.362e-04	28.9 years
Strontium	89	1.750e-04	50.57 days
Strontium	88	7.669e-07	Stable
Strontium	87	1.319e-08	Stable
Strontium	86	1.188e-10	Stable
Iodine	131	3.911e-05	8.02 days
Yttrium	90	8.958e-08	64.05 hours
Zirconium	94	1.947e-04	Observationally Stable
Zirconium	90	4.184e-12	Stable

Table of neutron-induced fission yields of common and relevant isotopes from the decay of U-235. Of particular interest are Cs-137 and Sr-90, both of which have intermediate half-lives and are therefore of great concern from an immobilisation perspective. They also both have relatively large fission yields compared to other common isotopes of Cs and Sr, and the more abundant isotopes tabulated have considerably shorter half-lives.

Sr-90 decays into Y-90, then subsequently to stable Zr-90, with the longest lived radionuclide in the decay chain being Sr-90. Sr also has the largest fission yield of these three nuclides, so immobilisation is a much more apparent issue.

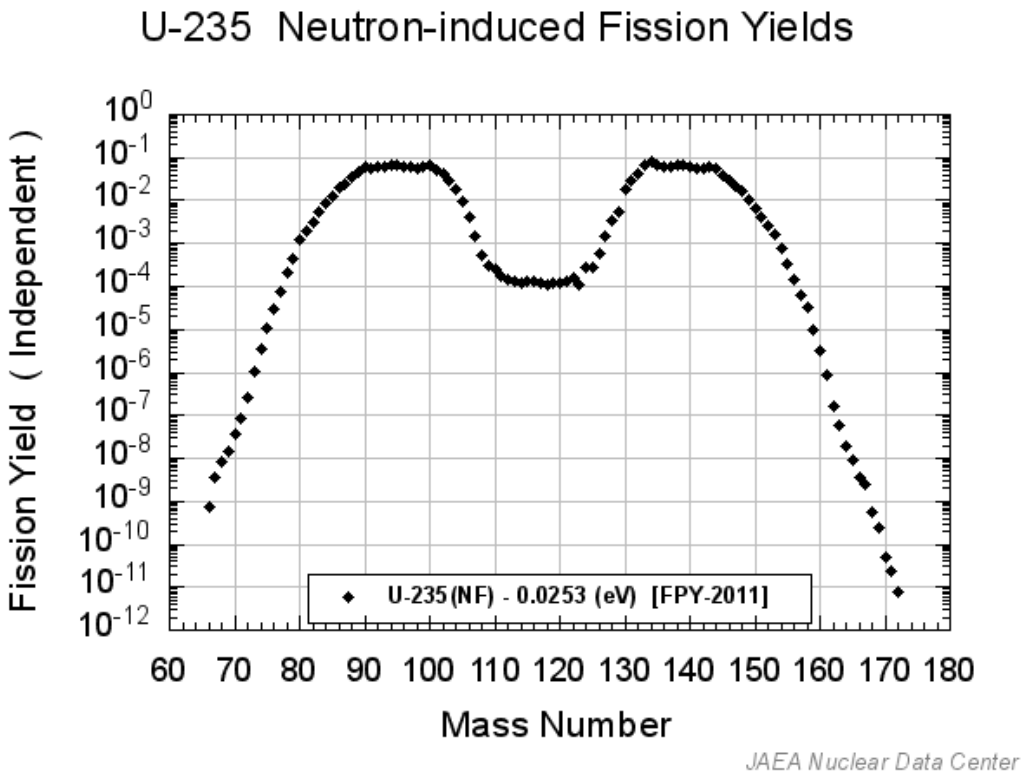

Graph of U-235 fission yields by mass number. Large observed peaks at approx. 90-100 and 130-145, showing the most abundant fission products are in this region.

Species of interest in the Sr-90 decay chain are within this area, as well as numerous Cs and Ba isotopes.

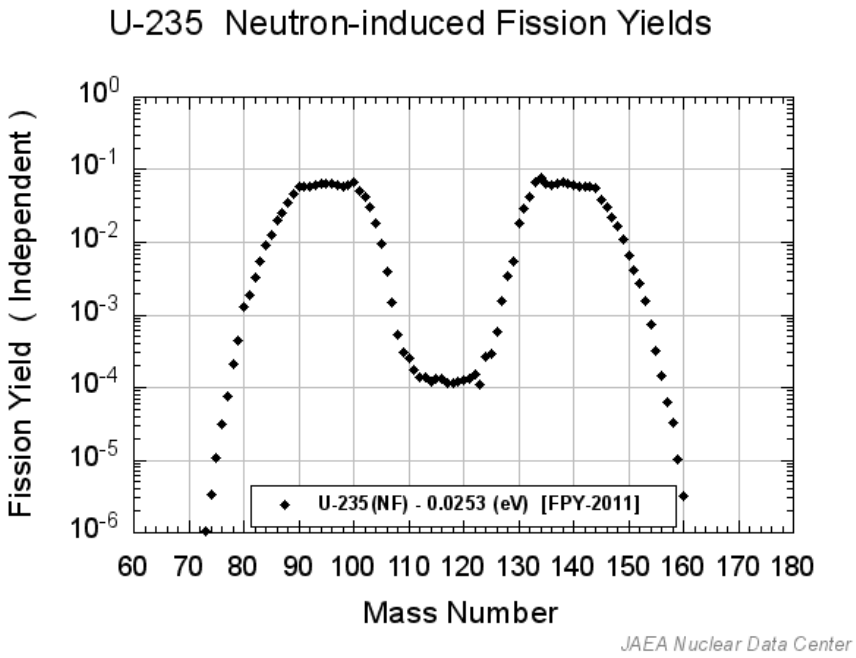

'Zoomed in' version of fission yield graph showing two distinct peaks of large fission yield.

Data from: JAEA Nuclear Data Centre, http://wwwndc.jaea.go.jp/cgi-bin/FPYfig (Accessed May 2015)

Radiation and Radioactive Decay Modes

Decay Mode	Particle Description	Effect on Nucleus
Alpha (α)	Helium Nucleus – two protons + two neutrons	Loss of two protons and two neutrons
Beta Negative (β^-)	High energy electron emission	Converts a neutron to a proton, emits an electron antineutrino
Beta Positive (β^+)	High energy positron emission	Converts a proton to a neutron, emits an electron neutrino
Gamma (γ)	High frequency photons	No change in proton/neutron numbers
Electron Capture	Proton rich nucleus absorbs an inner electron	Converts a proton to a neutron, emits an electron neutrino
Spontaneous Fission	Large unstable nucleus breaks down into two smaller nuclei	Splits nucleus into smaller, more stable nuclei
Neutron Emission	Neutron ejected from nucleus of neutron rich element	Element remains the same but becomes a different isotope

Appendix 2: Potentials and Structure Fitness

Mather Potential Set[1]				
Potential	**A**	**rho**	**C**	**Cutoff (Å)**
$Ca^{2+} – O^{2-}$	1340.18	0.3214	0.0	15.0
$Ti^{4+} – O^{2-}$	877.2	0.38096	9.0	15.0
$O^{2-} – O^{2-}$	22764.0	0.1490	43.0	15.0

Mather Core/Shell splits[1]			
Atom	**Core**	**Shell**	**Spring**
Calcium	-1.135	3.135	110.2
Titanium	39.863	-35.863	65974.0
Oxygen	0.389	-2.389	18.41

Strontium/Barium Potential Set[2, 3]				
Potential	**A**	**rho**	**C**	**Cutoff (Å)**
$Sr^{2+} – O^{2-}$	1250.00	0.3540	19.22	12.00
$Ba^{2+} – O^{2-}$	1150.00	0.38037	55.0	12.0

Sr/Ba Core/Shell splits[2, 3]			
Atom	**Core**	**Shell**	**Spring**
Strontium	3.45	-1.45	112.46
Barium	3.45	-1.45	56.23

1. G. C. Mather, M. S. Islam and F. M. Figueiredo, *Adv. Funct. Mater.*, 2007, **17**, 905-912.
2. C. L. Freeman, J. A. Dawson, H.-R. Chen, J. H. Harding, L.-B. Ben and D. C. Sinclair, *J. Mater. Chem.*, 2011, **21**, 4861-4868.
3. J. Dawson, X. Li, C. Freeman, J. Harding and D. Sinclair, *J. Mater. Chem. C.*, 2013, **1**, 1574-1582.

REE Potential Set				
Potential	**A**	**rho**	**C**	**Cutoff (Å)**
$La^{3+} – O^{2-}$	1439.7	0.3651	0.0	6.0
$Nd^{3+} – O^{2-}$	1379.9	0.3601	0.0	6.0
$Gd^{3+} – O^{2-}$	1336.8	0.3551	0.0	6.0
$Y^{3+} – O^{2-}$	1345.1	0.3491	0.0	6.0
$Yb^{3+} – O^{2-}$	1309.6	0.3462	0.0	6.0

For the rare earth elements, each potential was for a rigid ion with a 3+ (formal) charge, therefore there are no core/shell splits.

Calculated Structure Fitness to Oxides

CaO		
Parameter	**Initial**	**Calculated**
a (Å)	4.8152	4.6032
b (Å)	4.8152	4.6032
c (Å)	4.8152	4.6032

BaO		
Parameter	**Initial**	**Calculated**
a (Å)	5.6970	5.3301
b (Å)	5.6970	5.3301
c (Å)	5.6970	5.3301

SrO		
Parameter	**Initial**	**Calculated**
a (Å)	5.1613	5.0407
b (Å)	5.1613	5.0407
c (Å)	5.1613	5.0407

Appendix 3: Phase diagram and XRD patterns

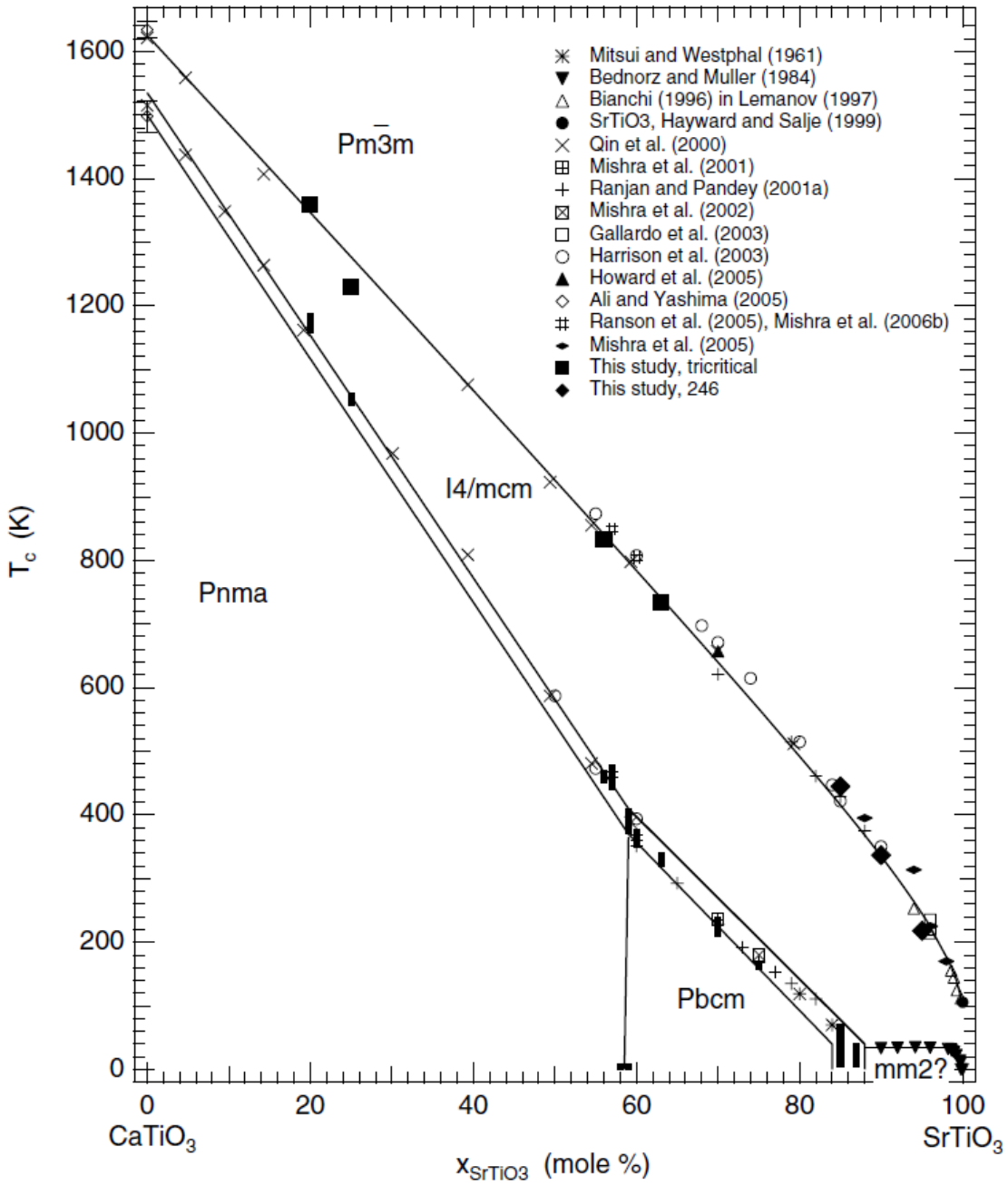

From: M. Carpenter, C. Howard, K. Knight and Z. Zhang, *J. Phys.: Condens. Matter*, 2006, 18, 10725.

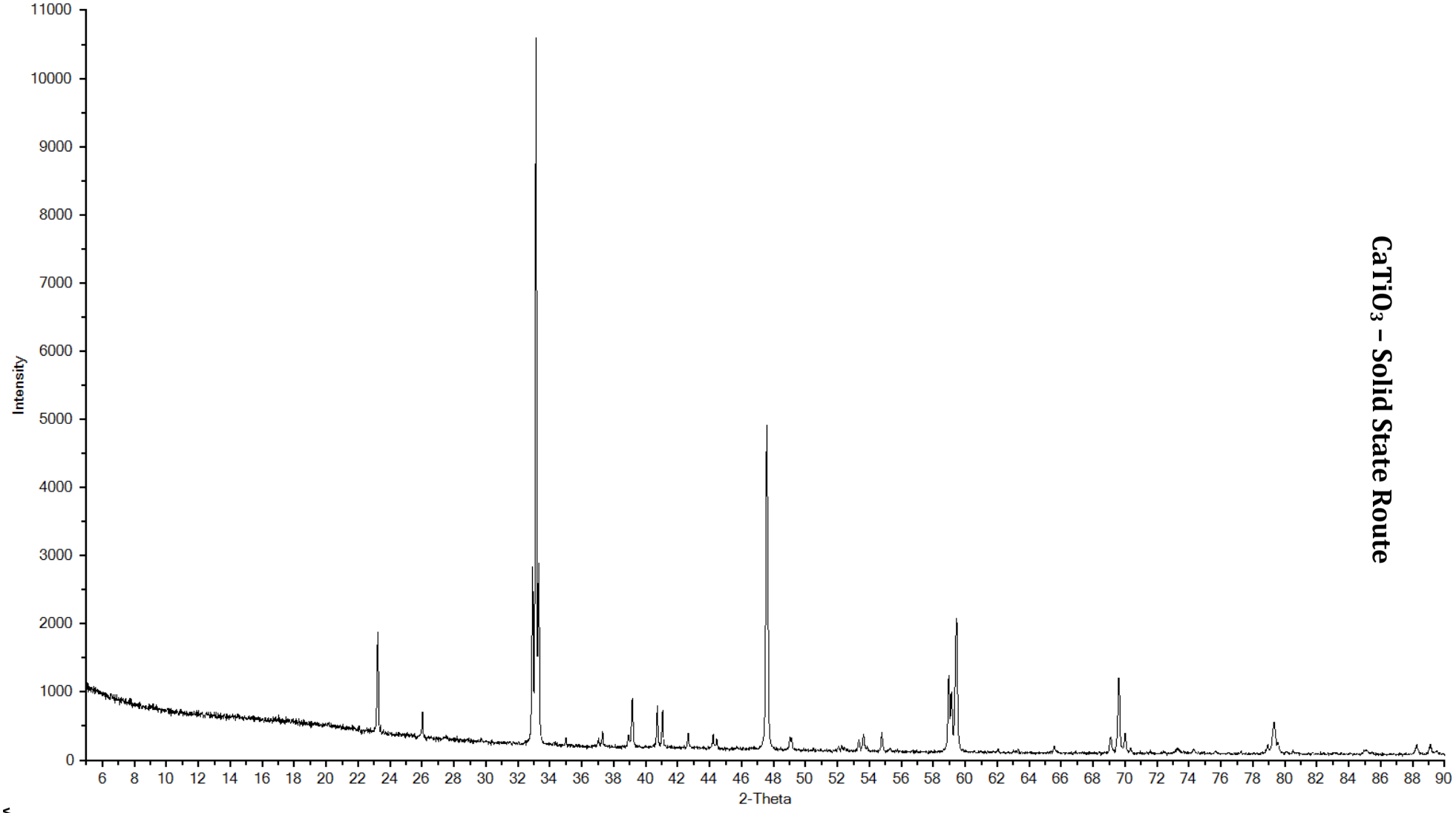
CaTiO3 – Solid State Route
Intensity
2-Theta
0
1000
2000
3000
4000
5000
6000
7000
8000
9000
10000
11000
6 8 10 12 14 16 18 20 22 24 26 28 30 32 34 36 38 40 42 44 46 48 50 52 54 56 58 60 62 64 66 68 70 72 74 76 78 80 82 84 86 88 90

$Ca_{0.7}Sr_{0.3}TiO_3$ – Solid State Route

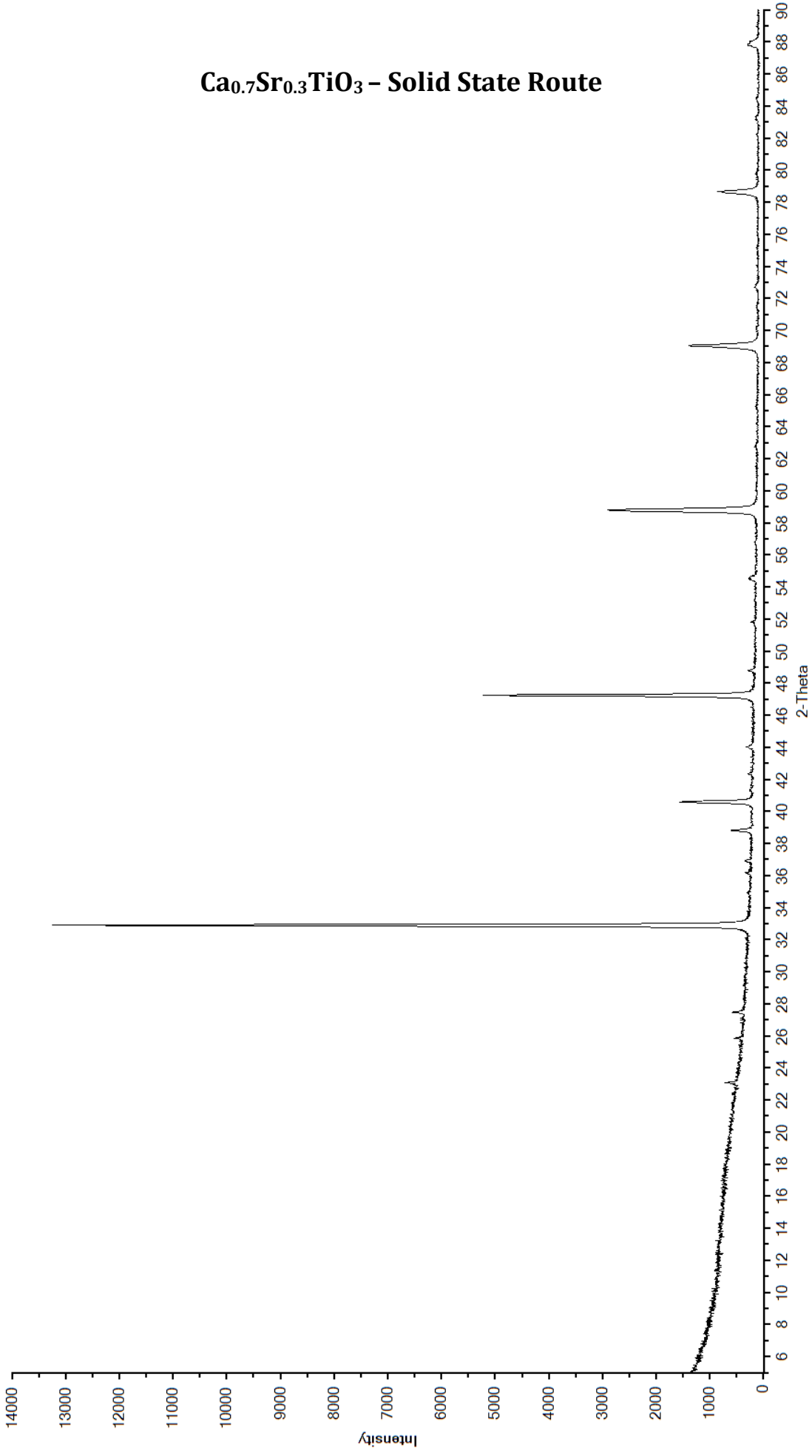

$Ca_{0.5}Sr_{0.5}TiO_3$ – Solid State Route

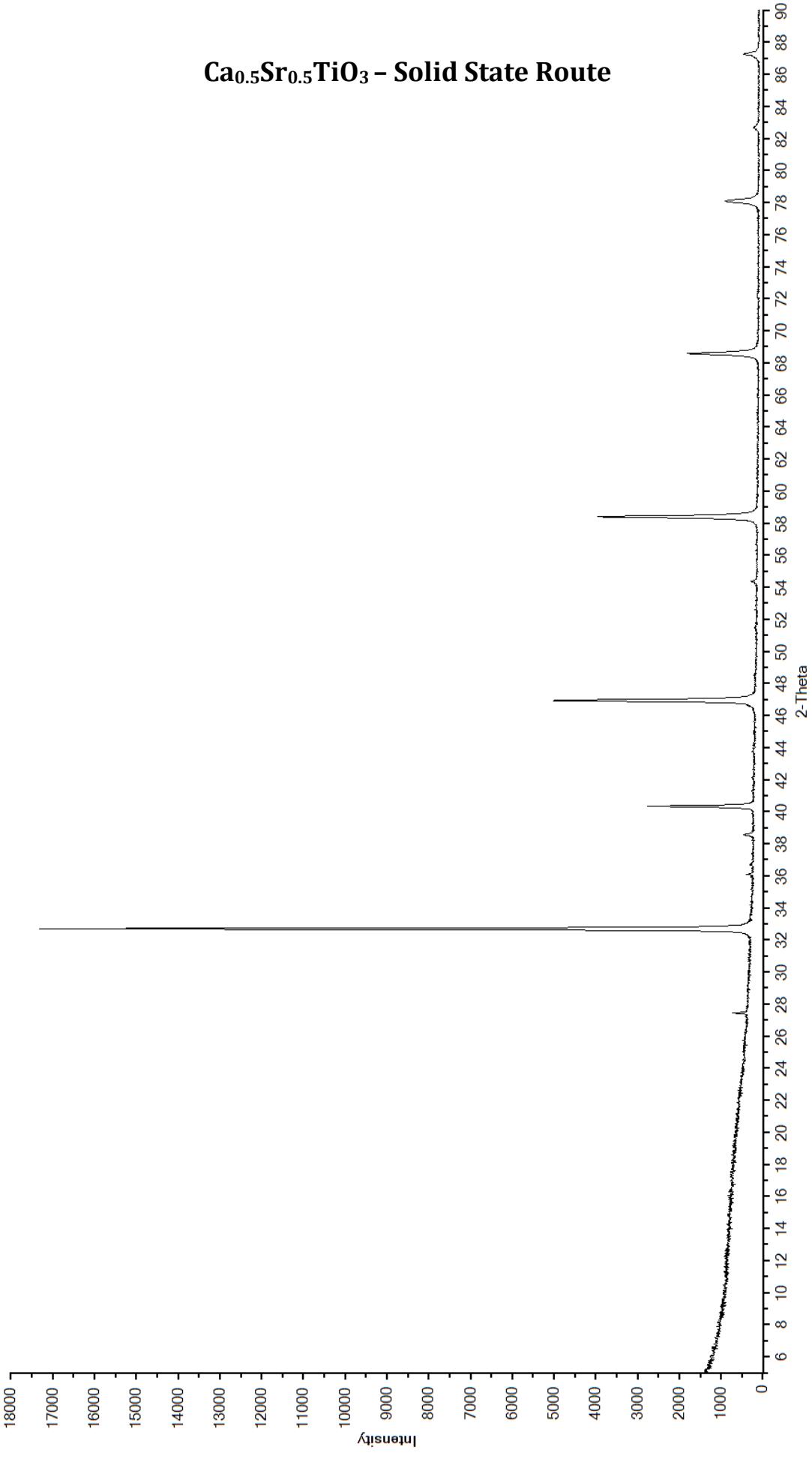

X

$Ca_{0.3}Sr_{0.7}TiO_3$ – Solid State Route

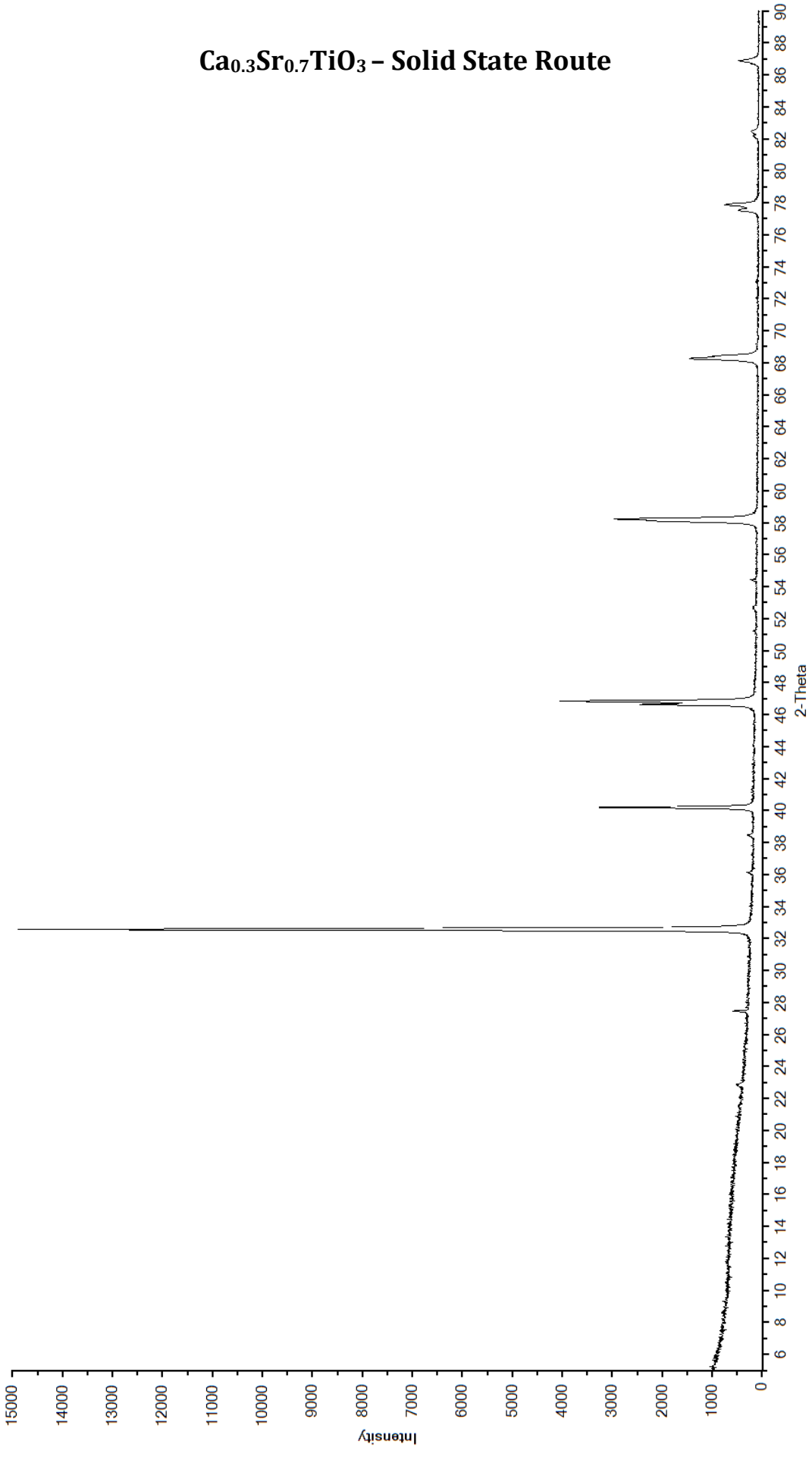

$SrTiO_3$ – Solid State Route

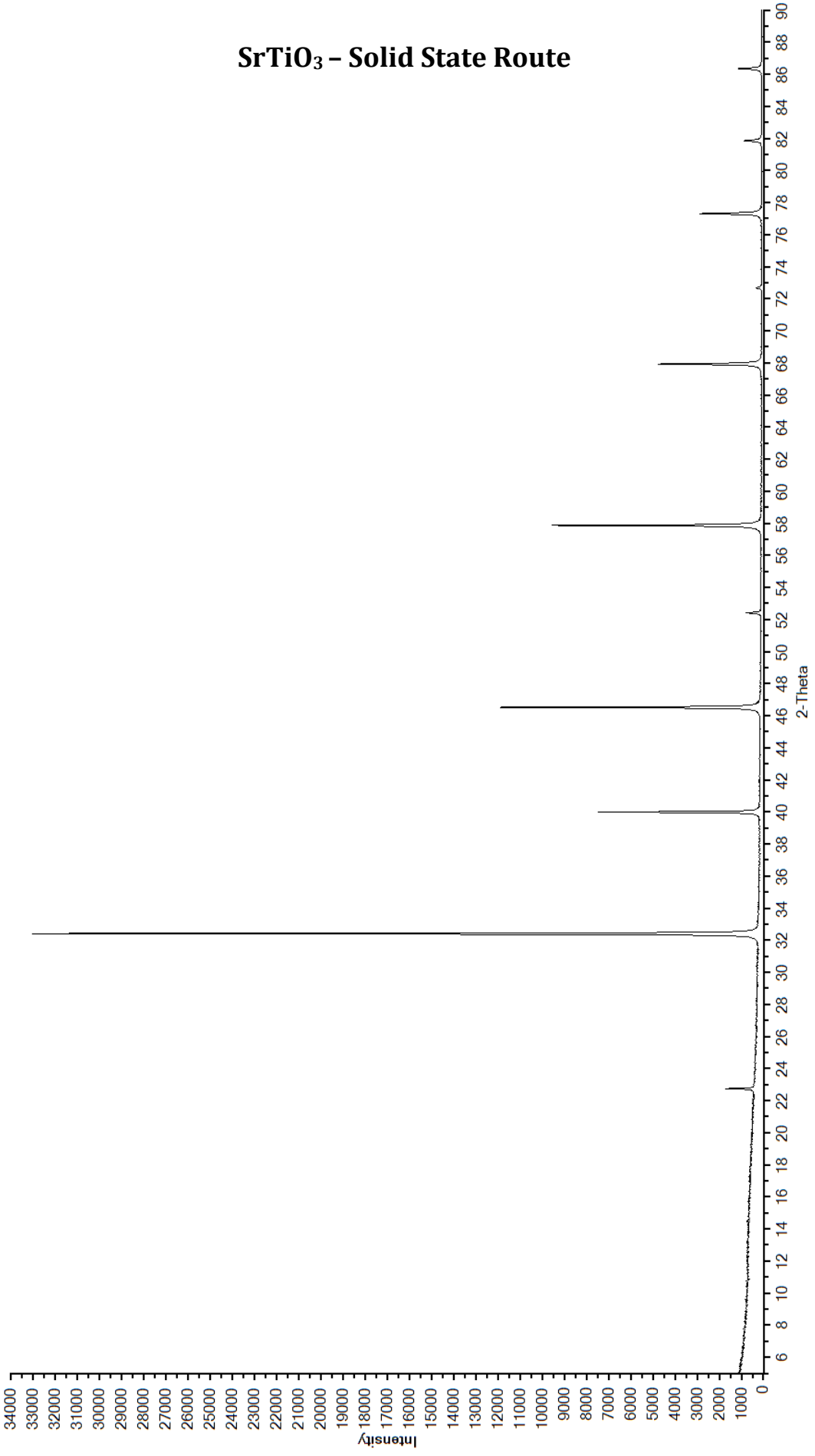

CaTiO3 – Rietveld

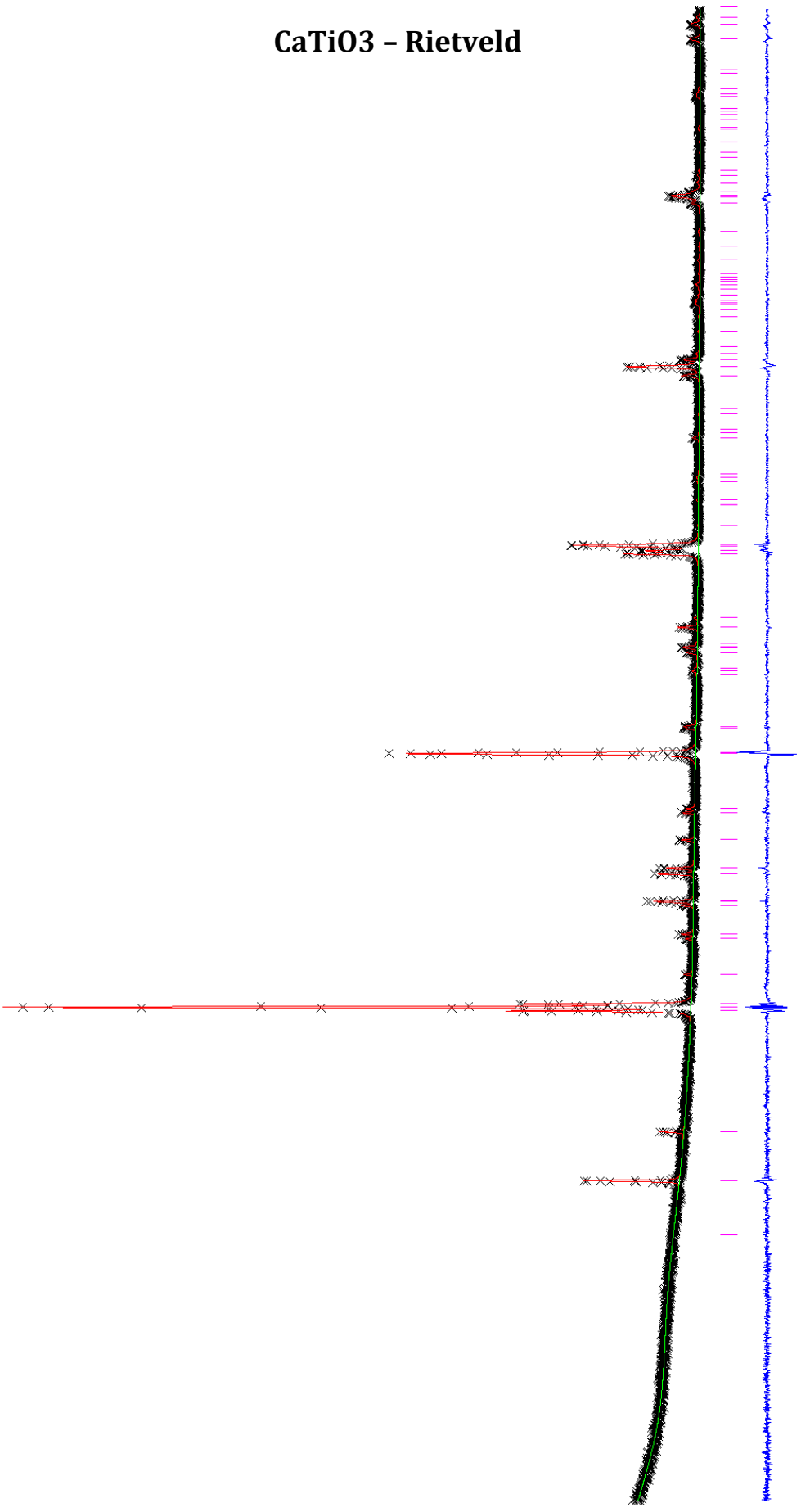

$Ca_{0.7}Sr_{0.3}TiO3$ – Rietveld

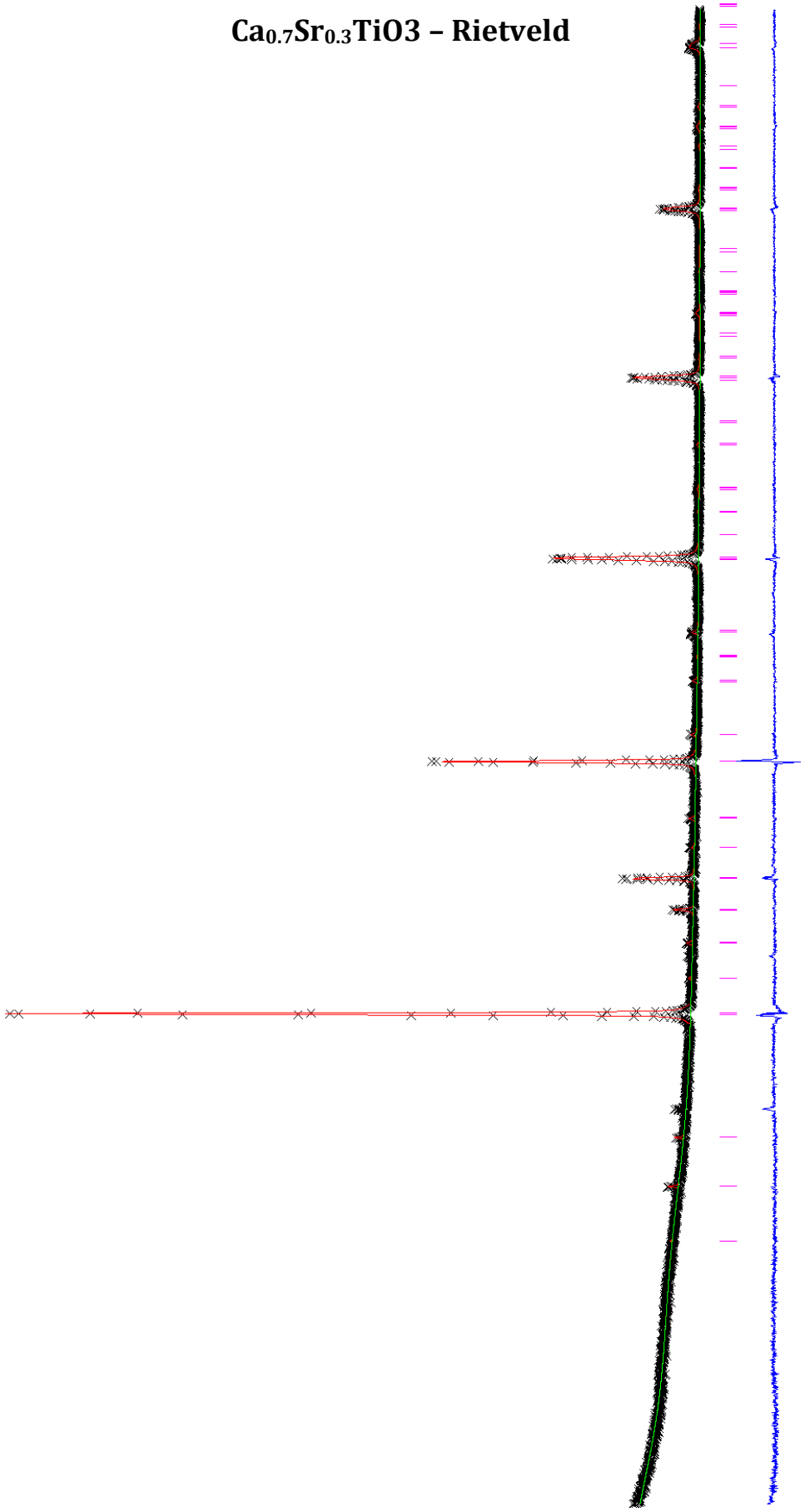

$Ca_{0.5}Sr_{0.5}TiO3$ – Rietveld

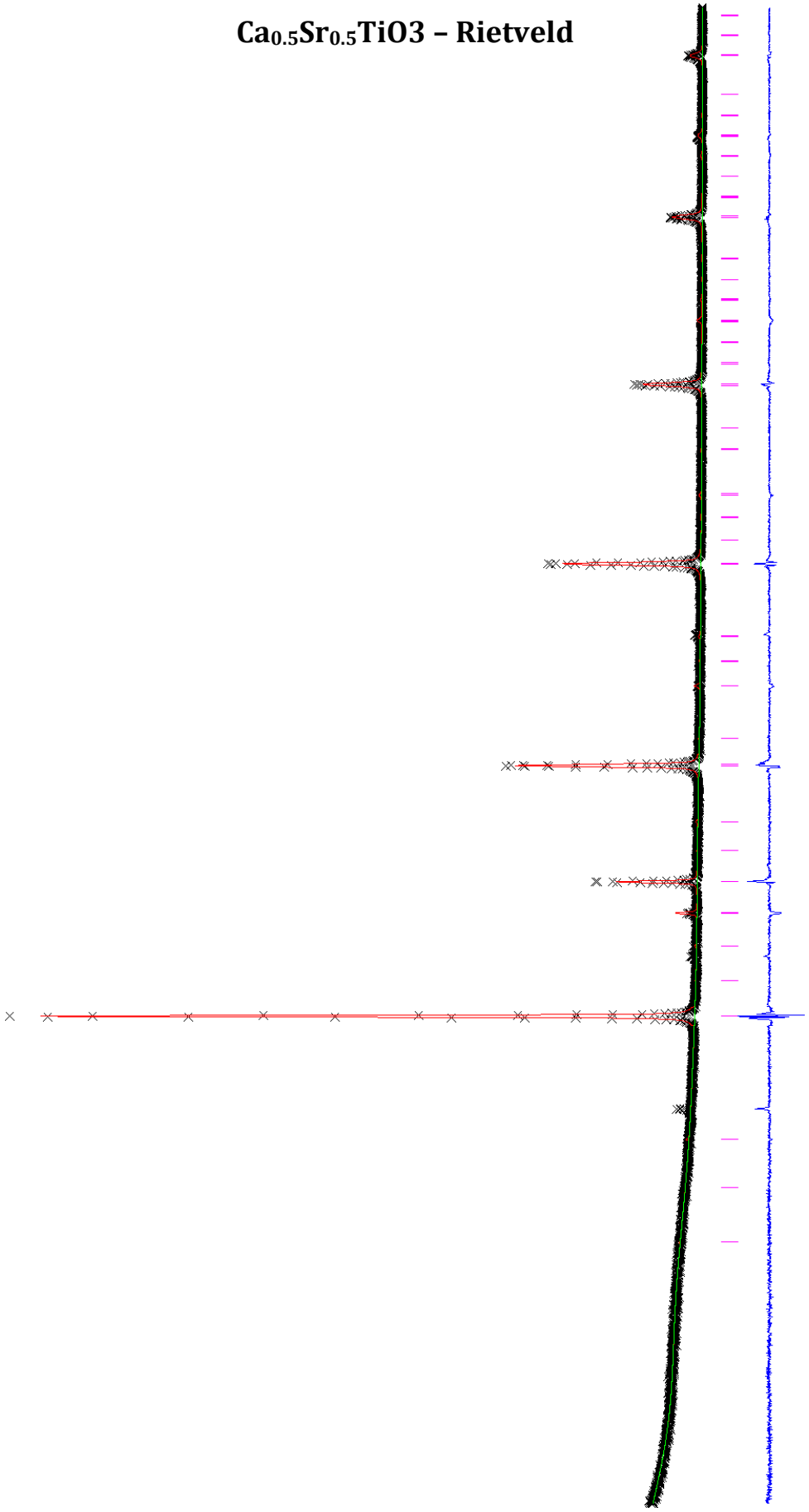

$Ca_{0.3}Sr_{0.7}TiO3$ – Rietveld

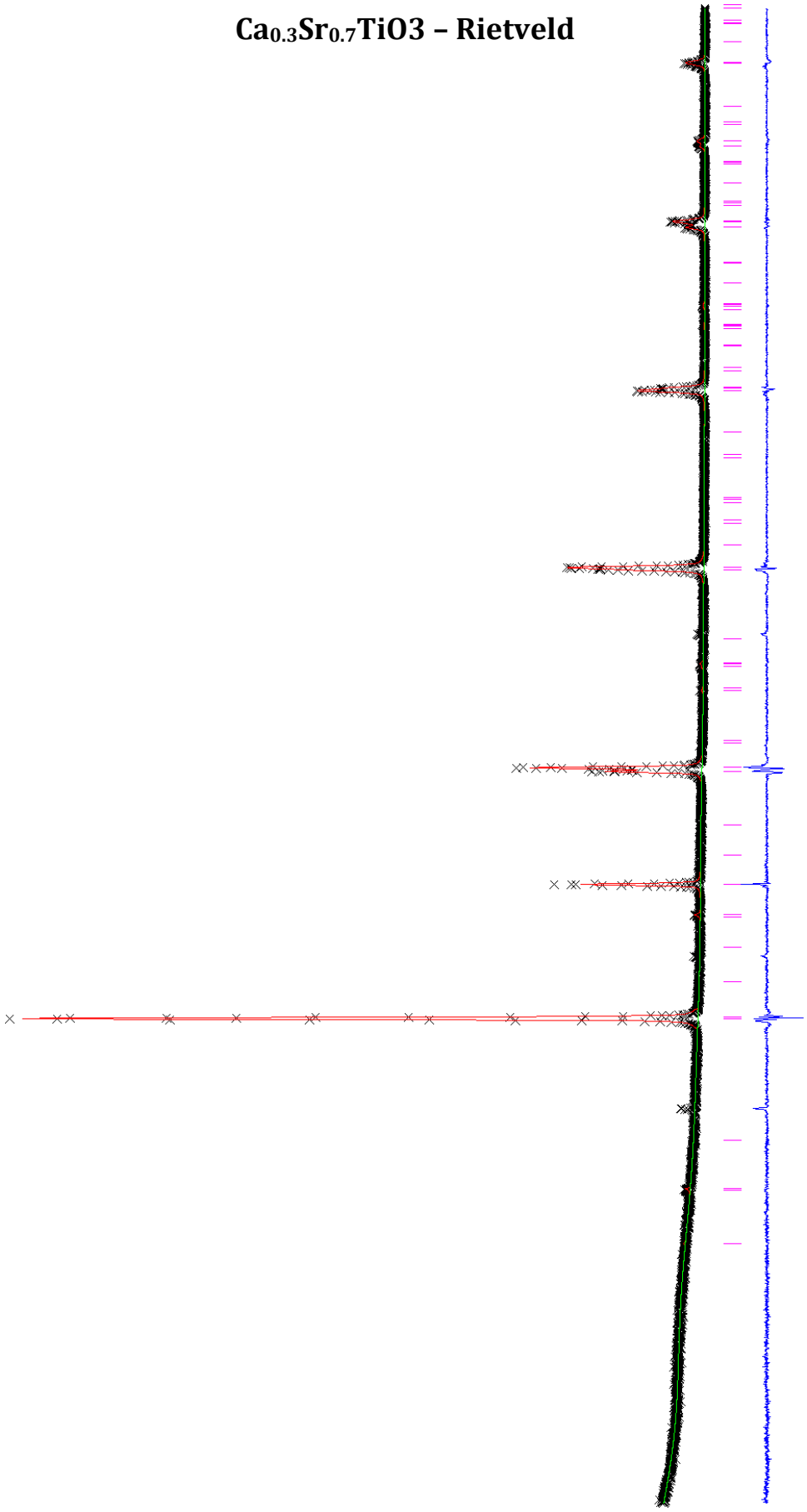

SrTiO3 – Rietveld

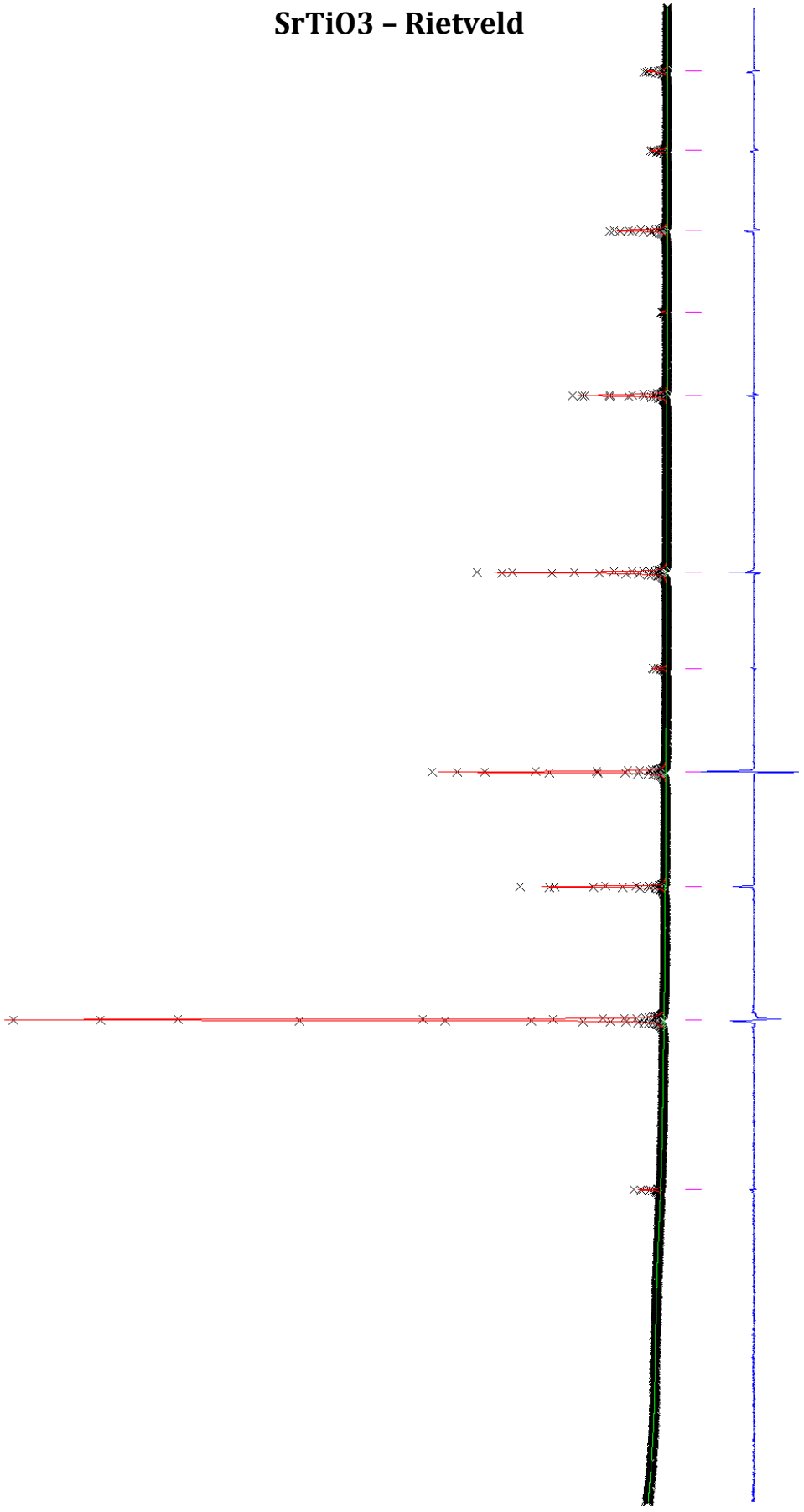

Appendix4: Example input files

```
regi prop dist opti comp conp nosymmetry full
title
Calcium Titanate Simulations - Mather - 15/10/14
end
# CaTiO3 Structure parameters and potentials obtained from:
# G. C. Mather, M. S. Islam and F. M. Figueiredo,
# Adv. Funct. Mater., 2007, 17, 905-912
# S. Sasaki et el,
# Acta. Crystallogr. C., 1987, 43, 1668
cell
5.4423 7.6401 5.3796 90.0 90.0 90.0
fractional 4
Ca core 0.4640 0.2500 0.0068 -1.135
Ca shel 0.4640 0.2500 0.0068 3.135
Ti core 0.0000 0.0000 0.0000 39.863
Ti shel 0.0000 0.0000 0.0000 -35.863
O core 0.5162 0.2500 0.5714 0.389
O shel 0.5162 0.2500 0.5714 -2.389
O core 0.2112 0.0371 0.2892 0.389
O shel 0.2112 0.0371 0.2892 -2.389
space
62
buck
Ti shel  O shel  877.2  0.38096  9.0  0.0  15.0
Ca shel  O shel  1340.18  0.3214  0.0  0.0  15.0
O  shel  O shel  22764.0  0.1490  43.0  0.0  15.0
spring
Ti 65974.0
Ca 110.2
O 18.41
dump 1 CaTiO3_Mather.dat
output xyz CaTiO3_Mather.xyz
output cif CaTiO3_Mather.cif
```

Fig. A1: An example input file for simulating pure bulk $CaTiO_3$ in GULP

The GULP input file contains a number of important keywords and sections as detailed below:

- The first line dictates the main commands the programme is going to follow, such as whether to keep the system at constant temperature (conp) or whether to optimise the structure (opti). Other possible commands are constant volume (conv) and (phonon) which measures the internal vibrations in the crystal.
- The second section is the title of the simulation, useful for keeping accurate records of the calculations being done.

- Third are the key structural parameters of the studied crystal system. The lattice constants are listed under the “cell” command, while the atomic positions and the space group are listed below the “fractional” command.
    - “Fractional” informs GULP that the inputted atomic positions are in fractional coordinates and not Cartesian. “Cartesian” would command GULP to read the coordinates in Cartesian.
    - Also listed are the charges on the core and shell of each species, which is the final column after the x y z atomic coordinates.
- The “buck” command tells the program to treat the next set of lines as Buckingham potential parameters.
    - Each line is read as: ‘atom A’ ‘atom B’ ‘A’ ‘rho’ ‘C’ ‘rmin’ ‘rmax’, where ‘rmin’ and ‘rmax’ are the cutoffs (in angstroms) of the potential.
- The “spring” command tells the programme the value of the spring constant between the cores and shells of each atom in the shell model.
- The output and dump files each produce an additional file in the output, giving more information than just the .out file.
    - The .dat file lists the final atomic positions and cell parameters of the simulated crystal
    - The .xyz file holds the cartesian coordinates of the atoms in the final structure and can be used in visualisations.
    - The .cif file contains all the information needed to recreate the crystal structure, can be used as a visualisation and also to create new inputs.

Additionally, defect simulations can be created by using the 'defect' command on the top line and adding a series of parameters to the input to define the defect.

```
vacancy 0.5 0.5 0.5
centre 0.5 0.5 0.5
size 14 28
```

Fig. A2: The lines required in the input to specify a vacancy on atomic position 0.5 0.5 0.5

- The first line in this section indicates the type of defect – either "vacancy", "interstitial", or "impurity" and the fractional coordinates of the defect
- The second line indicates the centre of the Mott-Littleton cluster in fractional coordinates, which is usually located on the defect site or centrally between multiple defects.
- The third line indicates the size of the region 1 and 2a radii of the cluster.

Within GULP potentials parameters can also be fitted using a series of observables and variables, and can also be fit to multiple phases of a material – such as cubic and orthorhombic variants of a perovskite. The parameters "fit" "relax" and "simul" are used to specify that a fitting run should take place and how the fitting algorithm should behave.

Additionally optimisers can be specified, such as "rfo" for more flexibility in how the algorithm can behave. An example of a fitting run, for the perovskite material caesium lead iodide $CsPbI_3$ is shown below.

```
fit relax opti conp comp prop phonon dist

maxcyc fit 50
switch rfo cycle 10
default_weight cell_length 10000
default_weight frac 100000
default_weight grad 100

#CsPbI3_cub

cell
6.275711 6.275711 6.275711 90.0 90.0 90.0

fractional
Cs core 3.137856 3.137856 3.137856
Pb core 0.000000 0.000000 0.000000
I core 0.000000 0.000000 3.137856
I core 0.000000 3.137856 0.00000
I core 3.137856 0.000000 0.00000
space
1
observables
bulk_modulus 19.8
end

species 3
Cs core 1.0
Pb core 0.5
I core -0.5

buck
Cs core I core 86581.8054101 0.288366216551 367.567225466 0.0 15.0 1 1 1
Pb core I core 33454.9759463 0.276808282411 459.567260058 0.0 15.0 1 1 1
I core I core 858790.467424 0.267255440475 1106.11361596 0.0 15.0 1 1 1
```

Fig. A3: A cubic $CsPbI_3$ fitting run

- In the first line the “fit” and “relax” commands are stated, telling GULP that a fitting run should be undertaken with the structure being relaxed in each step.
- The next line states that the maximum length of the fitting run should be 50 cycles. On cycle 10 the optimiser should switch to an rfo optimiser.
- The default_weight command specifies how much of an impact each particular observable should have on the final sum of squares of the fitting run. Here the cell lengths and coordinates have the highest weighting and therefore the greatest effect.
- In addition to defining the atomic positions and the space group, observables such as the bulk modulus (as shown here) can be fit to.
- The final lines show the Buckingham parameters which can be adjusted in the fit. The last 3 numbers tell GULP which parameter can be varied in the fitting process, with 1 as variable and 0 as fixed. Here all of the parameters can be varied in the fitting run.